THESIS FOR THE DEGREE OF DOCTORATE OF PHILOSOPHY

Unveiling massive galaxy evolution in the high-redshift universe

KIANA KADE

Department of Space, Earth and Environment
Division of Astronomy and Plasma Physics
CHALMERS UNIVERSITY OF TECHNOLOGY
Gothenburg, Sweden 2025

Unveiling massive galaxy evolution in the high-redshift universe

Kiana Kade
ISBN 978-91-8103-245-1
Acknowledgements, dedications, and similar personal statements in this thesis, reflect the author's own views.

Doktorsavhandlingar vid Chalmers tekniska högskola
Ny serie nr 5703
ISSN 0346-718X

Division of Astronomy and Plasma Physics
Department of Space, Earth and Environment
Chalmers University of Technology
SE-412 96 Gothenburg
Sweden
Telephone + 46 (0)31-772 1000
Email: kiana.kade@chalmers.se

Cover image: *James Webb Space Telescope image of the galaxy cluster SDSS J1226+2152*
Credit: ESA/Webb, NASA & CSA, J. Rigby and the JWST TEMPLATES team

Printed by Chalmers Reproservice
Gothenburg, Sweden 2025

Unveiling massive galaxy evolution in the high-redshift universe

Kiana Kade
Department of Space, Earth and Environment
Chalmers University of Technology

Abstract

The processes governing the rapid formation and evolution of massive galaxies in the early universe is one of the most profound and unresolved questions in modern extragalactic astronomy. Observations show that the cosmic star formation rate peaked at $z \sim 2-3$, demonstrating the distinct need to understand how galaxies acquired fuel for such vigorous star formation. Simulations point to galaxy mergers and active galactic nuclei (AGN) as the primary drivers of this buildup, but direct observational evidence for this at high redshift is limited and often ambiguous.

This thesis summarizes our current understanding of the growth of massive high-redshift galaxies, focusing on how the interplay between their environments, gas content, feedback, and star formation influences their evolution. Deep, high angular resolution observations of far-infrared and submillimeter gas tracers, primarily [C II] and CO emission, were used to study a sample of five galaxies: the quasar BRI 0952−0115 ($z = 4.432$), and the submillimeter galaxies SPT 0125−47 ($z = 2.51$), SPT 2134−50 ($z = 2.77$), G09v1.97 ($z = 3.63$), and AzTEC-3 ($z = 5.3$). Four of these galaxies are strongly gravitationally lensed, allowing for detailed studies of their interstellar medium and environments.

Small companion galaxies were identified nearby both BRI 0952−0115 and AzTEC-3, supporting the hypothesis that massive galaxies evolve in over-dense environments. Direct observational evidence of a gas exchange between a small companion and AzTEC-3 suggested that interactions with smaller galaxies can trigger and fuel intense star formation. Both systems exhibited gas outflows, though the driving mechanism behind them is uncertain. High-resolution imaging of G09v1.97 revealed a massive, rotating disk, challenging the conclusions of previous studies claiming the source was a merger. Observations of SPT 0125−47 and SPT 2134−50 showed tentative velocity gradients, suggesting that recent interactions and/or mergers may have triggered their high star-formation rates.

Overall, the results of this thesis underscore the importance of feedback, the environment, and support the hypothesis that massive high-redshift galaxies evolve in over-dense regions. This work highlights the role of gravitational lensing in uncovering faint structures and dynamical features that would otherwise be unobservable. Together, these findings provide new insight into massive galaxy evolution in the early universe.

Keywords: Galaxies: evolution – Galaxies: high-redshift – Galaxies: AGN – Galaxies: starbursts – techniques: interferometric – techniques: gravitational lensing

Research Contributions

This thesis is based on the work contained in the following papers:

I **Kade K.**, Knudsen K. K., Vlemmings W., Stanley F., Gullberg B., König S.:
Exploring the environment, magnetic fields, and feedback effects of massive high-redshift galaxies with [C II]
Astronomy & Astrophysics, Volume 673, A116 (2023)

II **Kade K.**, Knudsen K. K., Bewketu Belete A., Yang C., König S., Stanley F., Scholtz J.:
Probing the interstellar medium of the quasar BRI 0952−0115: An analysis of [C II], [C I], CO, OH, and H_2O
Astronomy & Astrophysics, Volume 684, A56 (2024)

III **Kade K.**, Yang C., Yttergren M., Knudsen K. K., König S., Amvrosiadis A., Dye S., Nightingale J., Zhang L., Zhang Z., Cooray A., Cox P., Gavazzi R., Ibar E., Michałowski M. J., van der Werf P. P., Xue R.:
Detailed lens modeling and kinematics of the dusty star forming galaxy G09v1.97: An analysis of CO(6–5), H_2O, H_2O^+, *and dust continuum emission*
Submitted to Astronomy & Astrophysics

IV **Kade K.**, Bredberg M., Knudsen K.K., König S., Drouart G., Romeo A., Bakx T.J.L.C.:
Resolving the molecular gas emission of the $z \sim 2.5 - 2.8$ *starburst galaxies SPT 0125−47 and SPT 2134−50*
Submitted to Astronomy & Astrophysics

Acknowledgements

Now at the end of the PhD it feels more difficult to write this acknowledgments section than I anticipated. This PhD has filled my life for almost six years and I have met some truly amazing people along the way, more than I could possibly name here.

I do not think I can write something here that properly acknowledges my supervisor Kirsten. She has been the best PhD supervisor I could have asked for. Kirsten has been constantly available to help, answers my stupid questions without making me feel stupid in the slightest, has been supportive of my choices, let me learn to make my own scientific decisions, and is one of the most compassionate people I have ever worked with. I have learned so much in these years working with her and I look forward to the next few years of getting to continue working in her group. I have told many people to choose their PhD supervisor, not their PhD topic, and if I had to choose again, I would choose Kirsten without any hesitation.

I have also met a number of my dear friends through my research group here at Chalmers (thanks to Kirsten for hiring these lovely people!). Flora took me under her wing when I first moved to Gothenburg, both at work and as a friend. Jan, who was hired at the same time as me but as a postdoc, was a great help to me in my first few years at Chalmers and has remained a close friend. Possibly the most impactful hire that Kirsten made during my time here was Madeleine. Madeleine and I were office-mates at Chalmers for almost four years, and I truly cannot image a better friend. Madeleine and I traveled around Europe and to Chile together for conferences and, like she said at my wedding, we never got sick of each other.

There are a number of other people from Chalmers that I am very grateful to have in my life. Theo, Chiara, and Thiebaut (The Running Cult) and all the crazy running and food shenanigans we have gotten up to. Holly (honorary Joules mention) and all the cosmere and boardgame nerdiness. I owe Matthias a huge thank you for being the best line manager ever. Finally a non-exhaustive list of people who I am so glad I have met and gotten to know during my time here at Chalmers: Andri, Bitten, Clare, Elvire, Gustav, Hannah, JB, Mark & Amy, and Tom.

Finally, thank you to my parents Kaya, Ward, and Janice for supporting my love of science and my desire to study galaxies, even when it took me to the other side of the planet. My sister, Alyx, has constantly thought that this whole PhD thing was pretty cool, which has been a continuous inspiration. Without this PhD, I would never have met my husband, Ariel. I am eternally grateful for the love and support he offers me on a daily basis. Our daughter, Iris, is the most amazing little human that I have ever met, and she makes me happy every single day.

As the Earth shrinks, the universe stretches forth its beckoning hand in a gesture to all mankind
- Public Service Broadcasting

CONTENTS

CHAPTER 1

INTRODUCTION

Approximately one hundred years ago, the Great Debate was held in Washington D.C. between two scientists arguing for and against the possibility of other galaxies apart from the Milky Way, our home. This debate sparked further research and led to the conclusive result that the Andromeda Nebula was, in fact, another galaxy (the Andromeda Galaxy). Today, it is estimated that there are $\sim 10^{11-12}$ galaxies in the observable universe. One fundamental topic in modern astronomy is galaxy formation and evolution, which addresses how galaxies grow, interact, and develop the structures observed in the local universe today. This thesis focuses on the early stages of cosmic history to investigate how galaxies developed during that epoch. A brief overview of the history of the universe is provided below to place this work in context before shifting to focus on galaxy evolution.

1.1 A brief history of the universe

The origin of the universe can be described as a 'Big Bang' followed by a period of intense inflation during which the universe expanded rapidly. The driving mechanisms of this rapid expansion are currently an open question in cosmology. The high temperatures and densities following the Big Bang resulted in the constitute matter of the universe being merely a sea of plasma: that is, a sea of protons and electrons swarming across the universe. As the universe continued to expand, temperatures and densities decreased sufficiently for the recombination of this plasma into neutral atoms. The radiation released by the process of recombination has been termed the 'Cosmic Microwave Background' (CMB) and is the most distant radiation observed in the universe.

Following the conclusion of recombination there was no significant source of radiation in the universe. Thus, the universe entered the 'cosmic dark ages'. During this time the universe was composed entirely of neutral hydrogen and helium. Inhomogeneities in dark matter distribution grew, and baryonic matter in the most massive of these eventually coalesced through gravitational collapse. This led to the formation of more familiar structures such as stars, and eventually galaxies.

The appearance of the first stars and galaxies marks the beginning of the period commonly referred to as ‘reionization’. Prior to the formation of the first stars (termed Pop. III stars), the hydrogen and helium in the universe was in its neutral state. These early stars, and subsequent galaxies, began re-ionizing the hydrogen in the universe with ultraviolet (UV) photons. Stars effectively created ‘bubbles’ of re-ionized hydrogen around them. These bubbles expanded around their stars until an entire galaxy was functionally an ionizing bubble. This process began at $z \sim 20$ (Planck Collaboration et al. 2016) and continued until a redshift [1](z) of $z \sim 6$ corresponding to about one billion years after the Big Bang, as indicated by a number of probes thought to trace ionization levels, such as Lyman-α emission and Gamma-ray bursts (e.g., Stark 2016).

The completion of the process of reionization marks the last large-scale property change of baryonic matter in the universe. How massive galaxy evolution proceeded from this period is an open question and the main topic of the this thesis.

1.2 Galaxies across cosmic time

An imperative aspect of understanding how galaxies look in the local universe (i.e., those located relatively ‘nearby’ the Milky Way) is to determine the evolutionary processes that led to their morphology and characteristics. Naturally, this requires the study of the predecessors of the Milky Way, and thus the study of the high-redshift universe. Observations of distances very far from Earth effectively look backwards in time, allowing for the characterization of the properties observed with increasing redshift, and the study of different galaxies grew and transformed.

Galaxies look different with increasing redshift suggesting that the evolutionary processes governing high-redshift galaxies were very different than those affecting the local universe and the Milky Way (e.g., Papovich et al. 2005). Increasing redshift leads to, among other things, an increase in the star-formation rate density, and a decrease in galaxy mass for massive galaxies (e.g., Conselice 2014; Madau & Dickinson 2014).

Galaxies are known to grow in conjunction with their dark matter halos (e.g., Kormendy & Ho 2013), primarily through accretion and mergers. The environment in which a galaxy evolves has a measurable impact on its development and growth. The most massive galaxies tend to form in more crowded environments (e.g., Springel et al. 2005; Vogelsberger et al. 2014), which in turn form along filamentary structures of dark matter distribution. Alternatively, some galaxies may develop in ‘voids’ or the less-dense spaces between dark matter filaments (Kreckel et al. 2011), but these galaxies appear to be relatively rare.

The general understanding of galaxy evolution is a constantly evolving landscape. The breadth of galaxy characteristics, such as mass, dust content, star-formation rate, and environment lead to a wide range of possibilities when attempting to derive a common evolutionary path through the extensive variety of observed

---

[1] Redshift is an astronomical term relating to the phenomenon of light from distant objects shifting to redder wavelengths due to the expansion of the universe. It is a ratio that can be calculated according to $z = \frac{\lambda_{\rm obs} - \lambda_{\rm emit}}{\lambda_{\rm emit}}$, where $\lambda_{\rm emit}$ is the rest-frame wavelength of the light and $\lambda_{\rm obs}$ is the observed wavelength.

galaxies. The puzzle of galaxy evolution is, as of yet, unsolved.

1.3 This thesis

This thesis aims to discuss the ways in which massive galaxies, specifically between $3 < z < 6$, evolve and the different factors that affect this evolution. The work presented focuses on the role of the environment, the effect of the central supermassive black hole (SMBH) on its host galaxy, and the gas kinematics of high-redshift galaxies. The incredible increase in technological capacity afforded in recent years has led to a dramatic escalation in direct observations of the environment of high-redshift galaxies. However, the frequency of interactions and/or mergers and the overall effect of the environment on these massive galaxies remains unclear. Additionally, probes of the effect of active galactic nuclei (AGN) in the high-redshift universe have expanded ten-fold in recent years, although there still remains a gap between theoretical models and the results of observational studies.

The work presented in this thesis provides the background for, and the results of, a number of case studies of massive galaxies during this epoch. By conducting a comparative analysis of these galaxies, both among themselves and in relation to other observational studies, it is possible to contrast empirical findings thus far with currently accepted scenarios for massive galaxy evolution. Observations probing the environments and internal processes of these systems have revealed that they exhibit the key characteristics relevant for understanding the mechanisms that drive galaxy evolution in the high-redshift universe.

CHAPTER 2

GALAXY FORMATION & EVOLUTION

In the nearby universe galaxies are often classified into two distinct categories: early and late types. Early-type galaxies, such as elliptical galaxies, are typically more massive with very low rates of star formation and older stellar populations (e.g., Hubble 1926; Schawinski et al. 2014). Late-type galaxies, such as spiral galaxies, are typically less massive, more gas rich, and have higher rates of star formation (e.g., Schawinski et al. 2014). This is shown in Figure 2.1. A first step to determining the evolution of these populations is by investigating different mechanisms of galaxy growth.

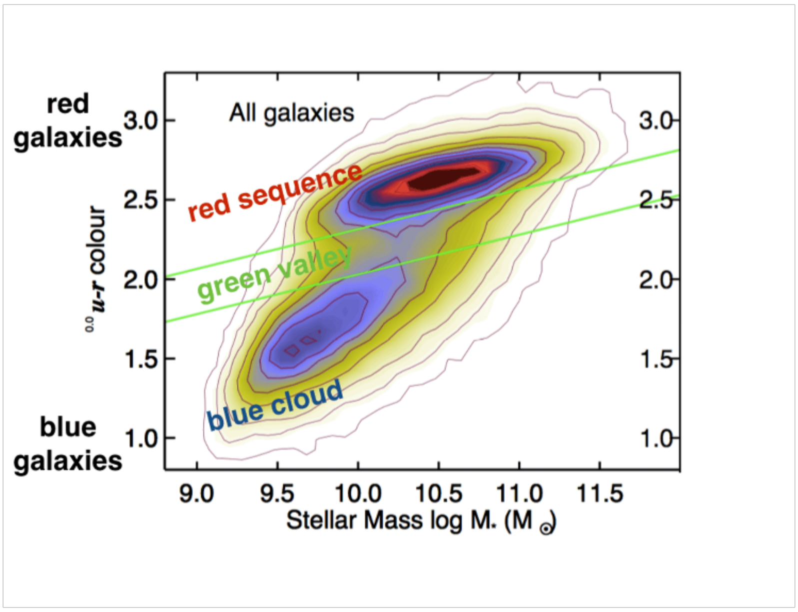

Figure 2.1: The galaxy color diagram showing the color of a galaxy (u-r filter flux) as a function of the stellar mass of a given galaxy. It is clear that the red sequence (elliptical/early-type galaxies) are, on average, significantly more massive than the blue cloud (spiral/late-type galaxies). Figure from Schawinski et al. (2014).

One method of tracing stellar mass in galaxies is through measuring star

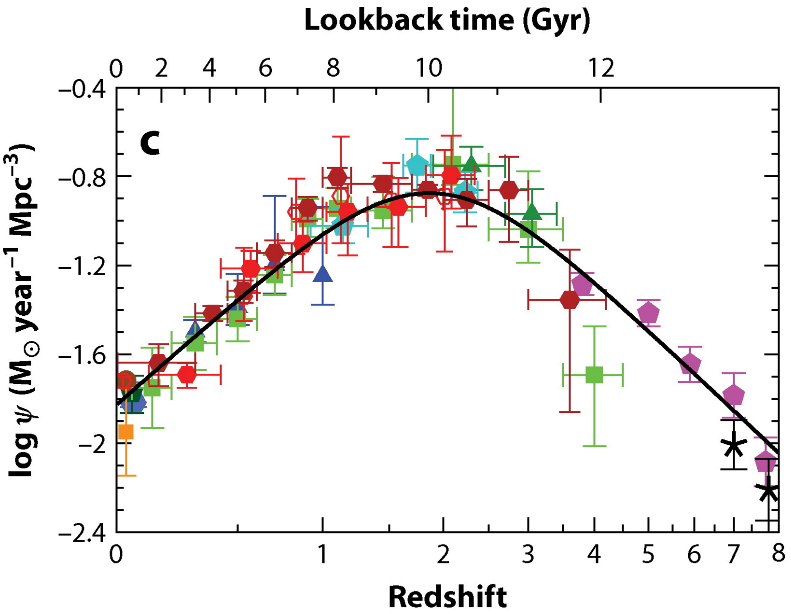

Figure 2.2: The star-formation rate density as a function of redshift (bottom) or cosmic time (top). This clearly demonstrates the peak in cosmic-star formation at $z \sim 2-3$. Figure from Madau & Dickinson (2014).

formation rates (SFRs). Examining how these rates evolve as a function of cosmic time provides key insights in the physical processes that drive galaxy growth. A variety of star-formation probes are available across a wide range of frequencies; this allows for a more global determination of SFR spanning a wide redshift range (e.g., review by Madau & Dickinson 2014). The SFR as a function of redshift has been found to peak at a redshift of $z \sim 2-3$ (approximately 2-3 billion years after the Big Bang), a period which has come to be termed ‘cosmic noon’. The rate of star formation rose preceding this redshift (i.e., $z > 2-3$) and fell proceeding (i.e., $z < 2-3$), shown in Figure 2.2. This peak leads to one fundamental question regarding the origin of cosmic noon: What physical processes enabled galaxies in the early universe to produce the extreme SFRs observed at cosmic noon? To answer this question it is necessary to understand how galaxies (both during this epoch and throughout cosmic time) grow and acquire gas and dust.

2.1 Main modes of galaxy growth

2.1.1 Gas accretion

One mechanism of galaxy growth is gas accretion. Through this process a galaxy accretes matter from the intergalactic medium (IGM) along dark matter filaments. As matter congeals along dark matter filaments, gravity becomes an ever-increasingly dominant mechanism, and the largest structures clump together. Galaxies themselves also typically form along these filaments with the most massive occurring at the intersections of different filamentary structures (e.g., Springel et al. 2005; Vogelsberger et al. 2014).

There exist two main modes of gas accretion: hot and cold mode accretion (e.g., Katz et al. 2003; Kereš et al. 2005; Dekel et al. 2009; Di Matteo et al. 2012). Cold mode accretion funnels cold, $T_{\text{gas}} \leq 10^5\,\text{K}$, gas (i.e., gas with $T_{\text{gas}} < T_{\text{virial}}$, where T_{gas} is the temperature of the gas and T_{virial} is the virial temperature of the galaxy halo) along the dark matter filaments into a galaxy from a wide range of distances and is dominant both in high-redshift environments and low-density environments at $z \sim 0$ (e.g., Kereš et al. 2005; Dekel et al. 2009). In contrast, hot mode accretion (i.e., gas with $T_{\text{gas}} > T_{\text{virial}}$) dominates in dense environments at low-redshift. A complication with this mode of accretion is that the hot gas must cool sufficiently through, for example, radiative means down to $T_{\text{gas}} < T_{\text{virial}}$ prior to becoming integrated into the galaxy. Additionally, these two modes of gas accretion can coincide in a given galaxy.

2.1.2 Mergers

Another mechanism of galaxy growth is mergers. Galaxy mergers can be broadly categorized into two main groups: minor mergers with mass ratios of $\lessapprox 4:1$ and major mergers with mass ratios of $1:1$. The contents of the merging galaxies play a large role in the outcome of the merger. A merger where both galaxies are gas-rich is often called a wet merger and can trigger star formation during and after the merger. An intuitive inference is that gas-rich mergers occur preferentially at higher redshifts when galaxies were, on average, more gas-rich and the universe was smaller (Lin et al. 2008). Conversely, a merger where both galaxies are gas-poor is called a dry merger and, following the above, these dominate in the local universe where galaxies are, on average, more gas poor than their high-redshift counterparts (e.g., Lin et al. 2008). There is the additional category of mixed mergers in which one galaxy is gas-poor and one gas-rich.

In the occurrence of a major merger, the end result is a galaxy lacking the pre-merger structure of its counterparts such as a disk (e.g., Barnes & Hernquist 1998). In this scenario, the result is a massive elliptical galaxy. Minor mergers do not destroy the structure of the more massive galaxy in the merger, rather they are thought to be one of the major growth pathways for massive spiral galaxies (e.g., Naab et al. 2009).

Theoretical and numerical modeling is important for understanding the role of mergers in massive galaxy growth. Evidence from cosmological hydrodynamical simulations, such as Illustris (Sijacki et al. 2015), showcase the importance of filamentary structures corresponding to both cold-mode accretion and galaxy mergers. Figure 2.3 shows the redshift evolution of a slice of the Illustris simulation and demonstrates the importance of filamentary structures and the increasing gas density at the intersections of these filaments with decreasing redshift.

2.2 Galaxy evolutionary sequence

There are many proposed scenarios to explain the process of galaxy evolution; focusing on massive galaxies, here follows the description of one of the most popular, though relatively simple scenarios for the development of such galaxies. A massive

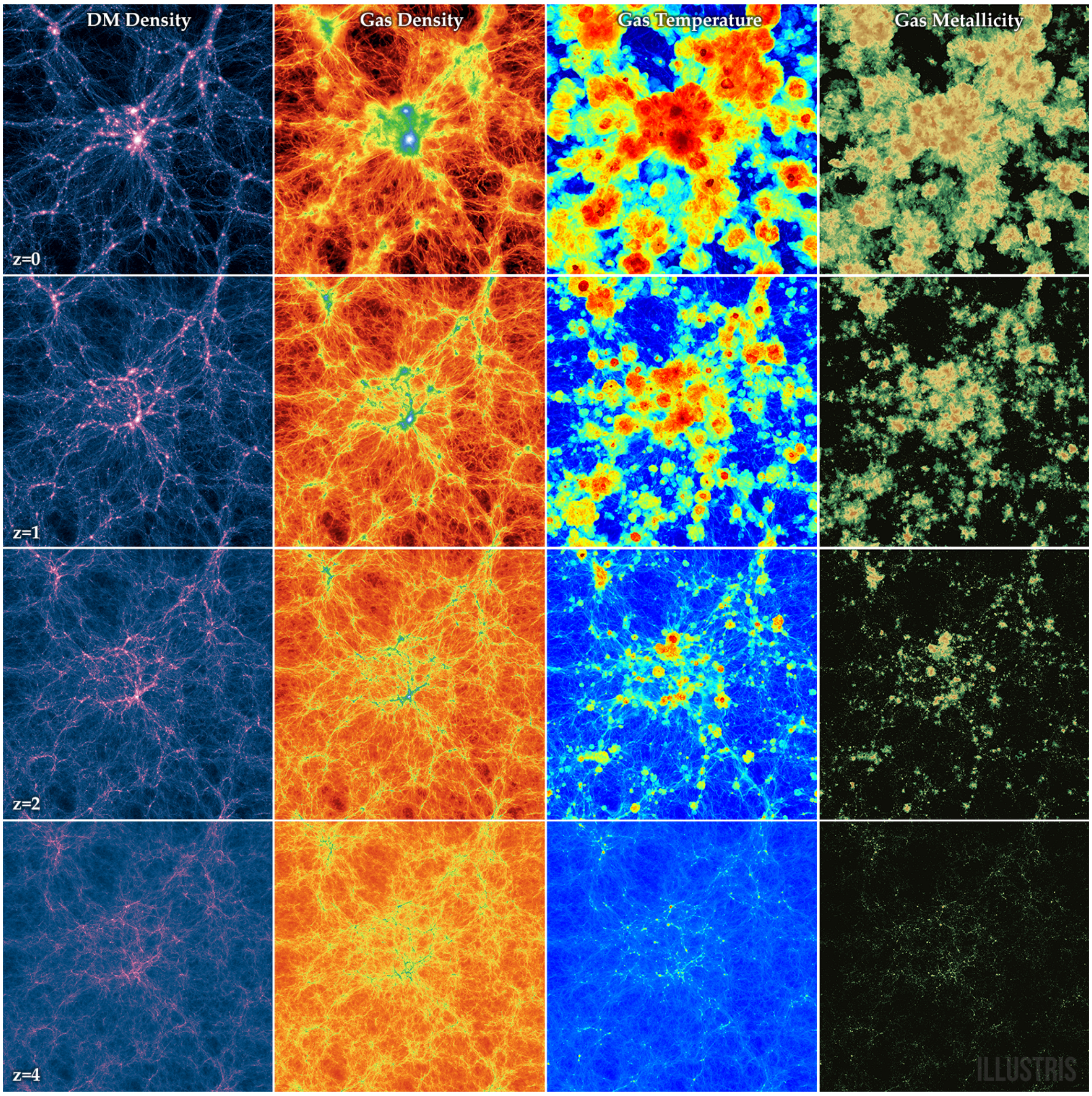

Figure 2.3: Different redshifts of a box slice of the Illustris simulation with lowest redshift ($z = 0$) at top. Columns from left to right: the dark matter density, gas density, gas temperature, and gas metallicity. It can be clearly seen that all properties increase or become more clumped together with decreasing redshift, and the importance of the dark matter structure is clear. Figure from llustris Collaboration/Illustris Simulation.

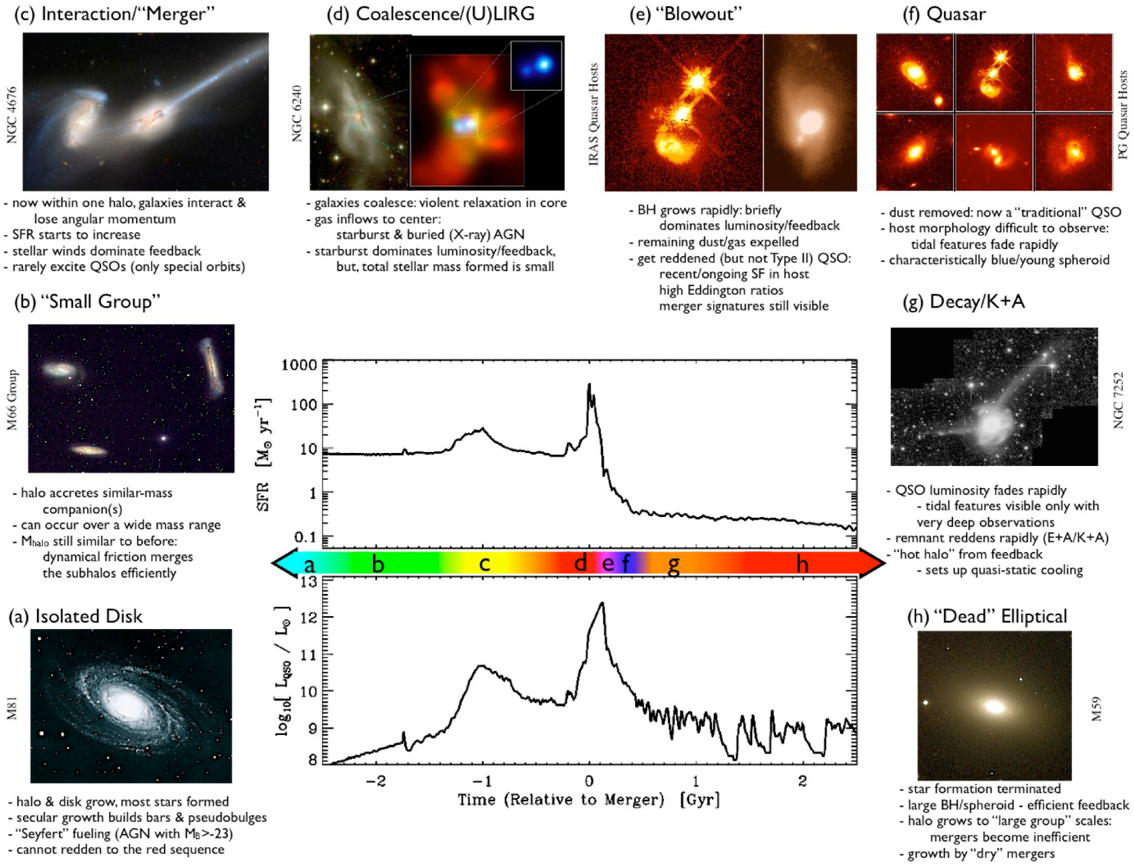

Figure 2.4: An example of the evolutionary steps of massive galaxy evolution. Note the increase in star-formation rate in top the central plot through steps (d) and (e). Figure from Hopkins et al. (2008).

galaxy develops in an over-dense environment. This over-density easily lends itself to the galaxy undergoing merger activity, be it major or minor interactions. Following a major interaction (or an accumulation of minor ones) the galaxies coalesce together and subsequently undergo a blowout phase, during which gas and dust are ejected from the galaxy. The coalescence phase is thought to be a period in which the central SMBH grows dramatically through excess matter infall provided by the merger(s). As the gas and dust have now been blown away from the galaxy, the galaxy presents as an unobscured quasar. Eventually, the lack of matter infall onto the AGN leads to quiescence of the SMBH and similarly a lack of star-formation. The already-formed stars within the galaxy gradually age and the galaxy transforms into a massive 'red and dead' elliptical galaxy (e.g., Sanders et al. 1988; Sanders & Mirabel 1996; Springel et al. 2005; Hopkins et al. 2006; Dasyra et al. 2007; Hopkins et al. 2008). This process is shown in detail in Figure 2.4.

This scenario presupposes galaxies grow in over-dense environments and that merger activity, specifically in the early universe, be high. Thus, predicting the presence of over-densities of galaxies at high-redshift is essential to verifying if this scenario is viable. Simulations of the high-redshift universe, such as Illustris (Sijacki et al. 2015) and Horizon-AGN (Dubois et al. 2014), have shown that interactions are predicted to be commonplace in the high-redshift universe. Studies have shown

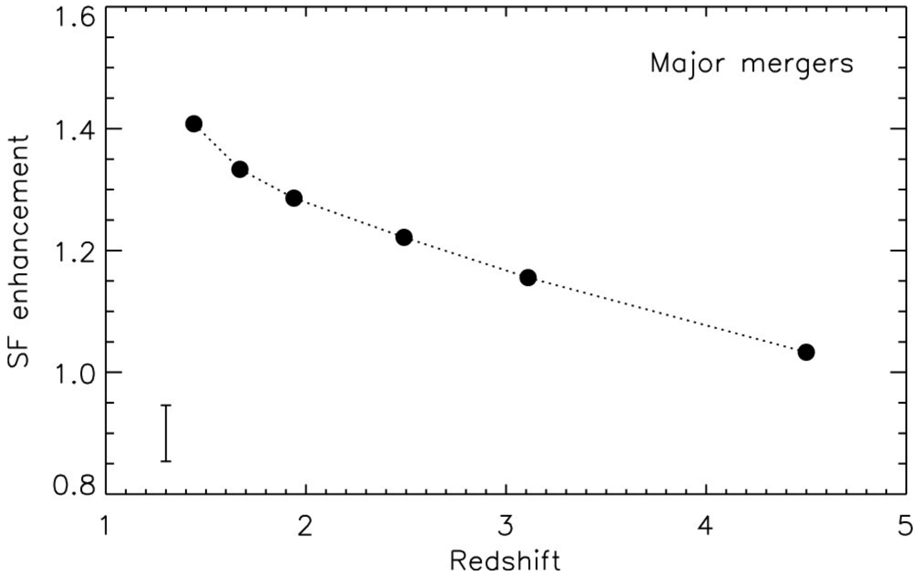

Figure 2.5: The star-formation enhancement following a major merger as a function of redshift in the Horizon-AGN simulation. The rate of enhancement drops significantly with increasing redshift. Figure from Kaviraj et al. (2015).

that minor mergers affect the star-formation rates and evolution of massive galaxies (e.g., Kaviraj et al. 2015; Sparre & Springel 2016; Pearson et al. 2019; Patton et al. 2020). By analyzing the results of the Horizon-AGN simulation, Kaviraj et al. (2015) found that by $z \sim 1$ all massive ($> 10^{10}\mathrm{M}_{\odot}$) galaxies had undergone a major or minor merger, and that minor mergers were around 2.5× more common than major mergers in the redshift range $1 < z < 4$. In addition, the authors found that major mergers were, in fact, not the dominant source of star-formation enhancement in a galaxy, but rather that minor mergers claimed this responsibility (Figure 2.5). As additional corroboration, a study by Fogasy et al. (2017) used semi-analytical model simulations and set a theoretical prediction that 22% of quasars should have at least one companion with stellar mass $> 10^{8}\mathrm{M}_{\odot}$.

Direct observations of companion galaxies, specifically less massive companions, are increasingly challenging with increasing redshift. However, these challenges are being overcome and the number of studies detecting faint companion galaxies to high-redshift massive galaxies have begun increasing. These observations are further discussed in Chapter 3.

2.3 Starburst galaxies

Most star-forming galaxies in the universe follow a trend relating SFR with stellar mass. This trend is generally referred to as the 'main-sequence of star-forming galaxies' (e.g., Brinchmann et al. 2004; Daddi et al. 2007; Elbaz et al. 2007; Noeske et al. 2007). Starburst galaxies lie above this trend. Their increased SFRs are typically attributed to the galaxy undergoing an episode of increased SFR triggered by, for example, galaxy interactions and/or mergers.

Starburst galaxies can have star-formation rates up to 1000 times the rate of typical main-sequence galaxies. A simple but relevant comparison is that of the Milky Way to local and high-redshift starburst galaxies. The Milky Way has a star-formation rate of $\sim 1-2\,\mathrm{M}_\odot\,yr^{-1}$ and lies on the local main-sequence (e.g., Licquia & Newman 2015). M82, a local starburst galaxy, has a star-formation rate of $\sim 10\,\mathrm{M}_\odot\,\mathrm{yr}^{-1}$ (e.g., Gao & Solomon 2004; Förster Schreiber et al. 2003a). HFLS3, a dust-obscured starburst at $z = 6.34$, has a star-formation rate of $\sim 3000\,\mathrm{M}_\odot\,\mathrm{yr}^{-1}$ (Riechers et al. 2013).

2.4 Active galactic nuclei

General reference: Kormendy & Ho (2013)

Galaxies in which the nuclear region of the galaxy emits prodigious amounts of energy are said to host Active Galactic Nuclei (AGN). In AGNs, it is thought to be the SMBH that powers the aforementioned energy and that the luminous nature of the nuclear region is the observational aspect of this phenomenon triggered by matter infall toward the black hole. The AGN population is suggested to play a key role in suppressing star formation (e.g., Cano-Díaz et al. 2012; Page et al. 2012), especially important since the number density of known quasars peaks at $z \sim 2-3$ when galaxies were at their most gas rich (e.g., Fabian 2012).

The observational characteristics of AGN are very diverse. The most widely accepted framework for explaining this diversion is termed the 'unified model of AGN' (e.g., Antonucci 1993; Urry & Padovani 1995; Tadhunter 2008). This model explains the different classes of AGN, such as quasars and radio galaxies, as being dependent on the orientation of the galaxy with respect to the observer; any observational differences between galaxies deemed to be AGN are assumed to stem from the viewing angle, shown in Figure 2.6. In this model, the SMBH is surrounded by an accretion disk of sub-pc size from which matter infalls toward the SMBH, thus driving its growth. Surrounding this is a larger, obscuring, dusty torus structure located at a distance of $0.1-10\,\mathrm{pc}$ (e.g., Ramos Almeida & Ricci 2017). Jets from the SMBH are powered by the extreme amount of matter infall, pushing matter perpendicularly out of the disk.

The infall of matter onto the central SMBH is thought to be one of the primary channels through which SMBH growth occurs. A tight correlation has been found between the mass of the SMBH and the velocity dispersion (σ) of the central bulge of a galaxy (e.g., Magorrian et al. 1998; Ferrarese & Merritt 2000; Gebhardt et al. 2000; Häring & Rix 2004; Gültekin et al. 2009; Beifiori et al. 2012; Kormendy & Ho 2013; Bennert et al. 2015; Reines & Volonteri 2015). This suggests a co-eval evolution of the SMBH and the host galaxy.

In recent decades it has been shown that cosmic noon was not only a peak of cosmic star-formation, but also a peak for AGN activity (e.g., Warren et al. 1994; Schmidt et al. 1995; Kennefick et al. 1995). During this time the most massive and most luminous AGN prevailed in the universe. This also implies that AGN growth 'shut-off' after following cosmic noon. In other words, if there was no mechanism of 'turning off' an AGN, they would continue growing alongside their host galaxies with no apparent limitations to their mass, which does not harmonize with observational

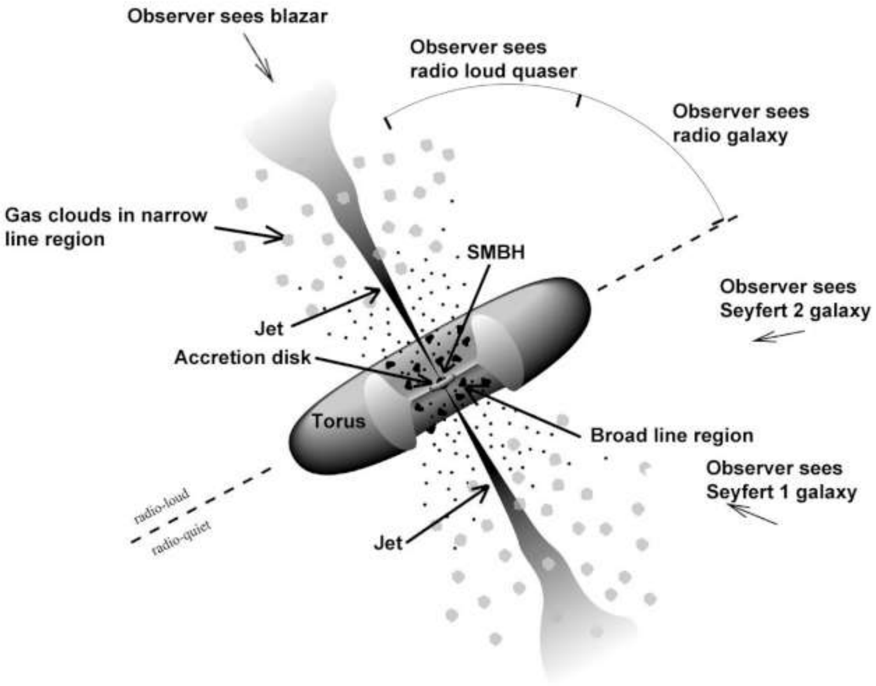

Figure 2.6: A mock-up of the unified model of AGN demonstrating their different classifications depending on viewing angle. Figure from Fermi and NASA.

results. However, a mechanism of quenching this growth must occur during cosmic noon for observations of the high-redshift universe to match what is observed in the local universe. AGN feedback has been named the likely culprit. Indeed, a central pillar of galaxy evolution simulations necessitate that in order to produce the structures seen in the local universe from their high-redshift predecessors, AGN-feedback must occur (e.g., Kauffmann & Haehnelt 2000; Granato et al. 2004; Di Matteo et al. 2005; Springel et al. 2005; Bower et al. 2006; Croton et al. 2006; Ciotti et al. 2010; Scannapieco et al. 2011). The full effect of AGN feedback is yet unknown, along with the scope of its influence on galaxy evolution as a whole; however, it is clear that feedback cannot be overlooked. AGN feedback is further discussed in Chapter 4.

2.5 Additional classifications

There exist a large diversity of galaxy classifications, far too numerous for an extensive summary in this thesis. However, a few deserve recognition due to relevance.

Submillimeter galaxies (SMGs) are a classification of high-redshift ($z \geq 2$) galaxies with properties similar to ultra luminous infrared galaxies (ULIRGs; Sanders & Mirabel 1996) in the local universe. SMGs are rare and generally faint in UV and visible light but extremely bright in sub-mm wavelengths ($> 1.0\,\mathrm{mJy}$ at $870\,\mu\mathrm{m}$, Blain et al. 2002). SMGs are heavily dust obscured and have high infrared luminosities, typically $L_{\mathrm{IR}} \geq 10^{12} L_{\odot}$, and thus high star formation rates of $> 1000 \mathrm{M}_{\odot} \mathrm{yr}^{-1}$. In addition, these galaxies have been found to have high gas masses and gas fractions as well as high dynamical masses (e.g., Tacconi et al. 2008; Engel et al. 2010; Riechers et al. 2011; Bothwell et al. 2013). Observations of SMGs benefit from a negative K-correction[1] which results in high-redshift galaxies exhibiting similar flux at sub-mm wavelengths between $z = 1 - 8$ (e.g., Casey et al. 2013). It has been shown that the SMG population peaks at $z \sim 2.5$ (e.g., Chapman et al. 2005; Wardlow et al. 2011; Simpson et al. 2014). Although SMGs were originally discovered using ground-based submillimeter telescopes, the *Herschel* Space Observatory expanded the selection to a wider range of wavelengths. Following this, a more generalized term, 'dusty star-forming galaxy' (DSFG), is often used to describe the population (see review from Casey et al. 2014).

Hot dust-obscured galaxies (Hot DOGs) are a rare class of strongly obscured and dusty galaxies with very red $[3.6-4.5]\,\mu$m vs. $[4.6-12]\,\mu$m colors in the Wide Infrared-Survey Explorer (WISE) color-color plot. Only around 1000 of these galaxies have been found (e.g., Eisenhardt et al. 2012), and they are constrained to the redshift range $1 < z < 4$ (e.g., Wu et al. 2012; Tsai et al. 2015). The bolometric luminosities of these galaxies are extremely high, $L_{\rm bol} > 10^{13}\,{\rm L}_\odot$ (e.g., Jones et al. 2014; Wu et al. 2014), and strong evidence suggests that these sources harbor strongly dust-obscured AGN (e.g., Stern et al. 2014; Piconcelli et al. 2015; Assef et al. 2015; Fan et al. 2016). Further, a fraction of these sources have also been shown to harbor intense starbursts similar to those of SMGs (e.g., Fan et al. 2016).

Lyman break galaxies (LBGs) are a class of star-forming high-redshift galaxies that are selected based on the presence of a characteristic break in the UV-portion of their spectrum (e.g., Steidel et al. 1996; Giavalisco 2002). These galaxies are massive, with stellar masses of $M_\star \sim 10^{9-11}\,{\rm M}_\odot$ (e.g., Reddy et al. 2006). While LBGs are also intensely star forming, they differ from SMGs by having lower dust content (e.g., Coppin et al. 2015; Schouws et al. 2022). However, some IR-bright LBGs have been found to also host significant dust-obscured star formation (e.g., Koprowski et al. 2020). The IGM along the line-of-sight to these galaxies absorbs the UV light at wavelengths shorter than 912 Å, thereby creating a sharp break in the galaxy's light. As redshift increases, the break also becomes redshifted, and allows for relatively easy detection with observations over a wide range of wavelengths. Although the original LBG definition was specific to the galaxy detection in the range $3 < z < 5$, this method has now been used to detect galaxies up to $z > 10$ (e.g., Oesch et al. 2016).

---

[1] The negative K-correction is the term assigned to the observational phenomena by which the flux density observed at wavelengths longer than $250\,\mu$m stops declining as the inverse square of distance. Instead it remains approximately constant from $1 < z < 10$.

CHAPTER 3

THE ROLE OF ENVIRONMENT: COMPANION GALAXIES

As highlighted in previous chapters, the role of a massive galaxy's environment is thought to play a major role in its evolution. Interactions between massive galaxies and their companions represent an evolutionary juncture in the evolution of these galaxies and their fate. It has been shown that up to a quarter of the population of $z < 1.5$ massive galaxies do not live alone (e.g., Alberts & Noble 2022, and references therein). The term environment is often defined ambiguously in the literature and refers to either larger scale areas such as galaxy clusters, or more localized regions around single galaxies; see Alberts & Noble (2022) for a more detailed discussion of this point. This thesis focuses on the local environment around massive galaxies, and primarily on companions found at close spatial distances.

Theoretical predictions have prompted the search for companion galaxies, small and large, in the high-redshift universe. Direct observations of companion galaxies is a challenging task. Companions need not be as massive as their massive counterparts and might be located relatively near their massive neighbors, and thus difficult to resolve and/or distinguish at the typical resolution of observations (often > 1 arcsecond). Detections of merger activity are generally associated with observations of tidal structures, direct imaging of the merger (such as the case of NGC 2623, Cortijo-Ferrero et al. 2017), or the use of kinematic signatures such as evidence of outflowing gas that can be directly associated with the companion. Combined, this has posed a great challenge in detecting companions at high redshift, and thus complicated studies on the role of mergers as a significant factor in the evolution of distant, massive galaxies.

3.1 Observational challenges

The angular resolution of observations depend, among other things, on the distance to the observed source. The spatial size, as seen per arcsecond, increases up to a redshift of ~ 2 at which point the curve turns over and begins decreasing due to the expansion of the universe and the finite speed of light, see Figure 3.1. For observations of $z \sim 4-5$ objects, the spatial size of said observations is $\sim 6-7$ kpc per arcsecond. As a reference point for galaxy structure size, the diameter of the Milky Way is ~ 30 kpc. The consequence of this is that much of the finer structure is lost in high-redshift observations. Hence, resolving massive companions from massive galaxies is a challenge, and even more so for the faint and small companions to massive galaxies.

Furthermore, the amount of time spent observing on-source greatly impacts the ability to detect fainter companion galaxies. The following simple example helps demonstrate this point. Consider a scenario in which observations target the [C II] 158 μm ($^2P_{3/2} \rightarrow ^2 P_{1/2}$) emission line in a massive galaxy at $z = 4.5$ and detect a peak flux density of 10 mJy and full-width-half-max (FWHM) of 300 $\mathrm{km\,s^{-1}}$ corresponding to a line luminosity of $L_{[\mathrm{CII}]} = 2.0 \times 10^9\,\mathrm{L_\odot}$ or a SFR of $\sim 180\,\mathrm{M_\odot\,yr^{-1}}$ (using the starburst relation from De Looze et al. 2014). Companions exhibiting 10% the flux density of the massive galaxy (1.0 mJy) would have line luminosities of $L_{[\mathrm{CII}]} = 2.0 \times 10^8\,\mathrm{L_\odot}$ or a SFR of $\sim 20\,\mathrm{M_\odot\,yr^{-1}}$. In order for ALMA to detect such companions with 5σ certainty in a 50 $\mathrm{km\,s^{-1}}$ channel, images would need to have sensitivities of 0.2 $\mathrm{mJy\,beam^{-1}}$ per channel. This corresponds to 2 hours of on-source observing time. Changing the peak flux density of the companions to 2.0 mJy results in 30 minutes of observing time required for a 4σ detection. These hypothetical scenarios demonstrate the importance of deeper observations than what has historically been commonly performed with the Atacama Large submillimeter/Millimeter Array (ALMA) where observations have often been on the order of ~ 30 minutes. One additional complicating factor is that the detectability of companion sources has been shown to depend greatly on the tracer utilized to observe them. Studies using continuum observations have often reported no overdensities around massive high-redshift galaxies (or even underdensities, e.g., Willott et al. 2005; Yue et al. 2019) while others using line emission (typically [C II] or Lyman-α) report detections of companions (e.g., Neeleman et al. 2019; Venemans et al. 2020).

Indeed, the difficulties in observing high-redshift companion galaxies has led to conflicting results, specifically when using optical, near-infrared, or Lyman-α emission. A number of studies found little evidence of companion galaxies around high-redshift starbursts and quasar host galaxies (e.g., Willott et al. 2005; Bañados et al. 2013; Mazzucchelli et al. 2017; Yue et al. 2019). For example, Bañados et al. (2013) used Lyman-α emission to search for LAEs around the $z \sim 6$ galaxy ULAS J0203+0012 and concluded that there was no difference in LAE number density surrounding that galaxy in comparison to blank field surveys. However, other studies detected over-dense regions surrounding the galaxy of interest (e.g., Husband et al. 2015; Fan et al. 2016). For example, Husband et al. (2015) used Multi-Object Spectroscopic Explorer (MUSE) observations to investigate the environment of the quasar PKS1614+015 at $z = 3.2$. PKS1614+015 is a well-known quasar that had previously been identified as a system consisting of the radio-loud quasar and a companion galaxy with a bridge of ionized gas extending between the two sources. The MUSE observations detected this bridge in Lyman-α emission along with three other Lyman-α emitting galaxies within the virial radius of the quasar; this suggests that this system is either in the process of merging or will one day do so. These

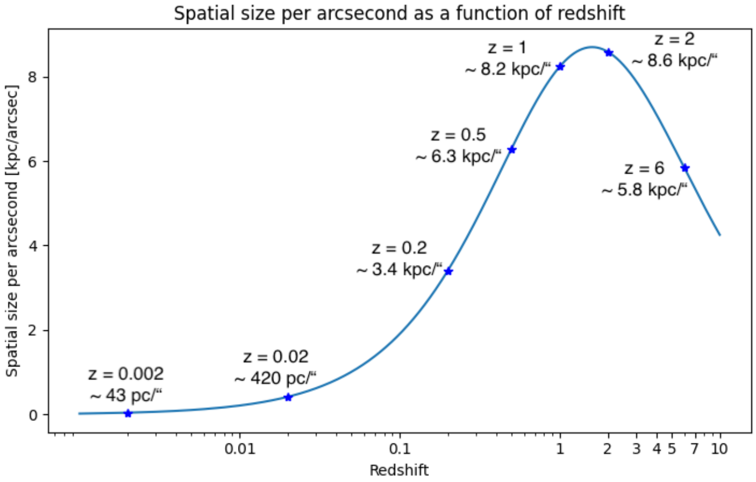

Figure 3.1: The spatial size per arcsecond as a function of redshift using Planck 2015 Cosmology (Planck Collaboration et al. 2016). Illustration by Madeleine Yttergren.

conflicting results illustrate the difficulty of drawing firm conclusions about the presence of overdensities in the environment of high-redshift massive galaxies.

3.2 Recent results

In recent years, with the assistance of ALMA and other radio interferometers, the hunt for companion galaxies to massive high-redshift galaxies has become more fruitful. Observations targeting the bright and ubiquitous [C II] and ^{12}CO (hereafter CO) emission lines have led to a striking increase in companion detections and indications of interaction activity (e.g., Oteo et al. 2016; Trakhtenbrot et al. 2017; Decarli et al. 2017; Díaz-Santos et al. 2018; Wardlow et al. 2018; Casey et al. 2019; Jones et al. 2019; Litke et al. 2019; Neeleman et al. 2019; Fogasy et al. 2020; Venemans et al. 2020; Bischetti et al. 2021). These studies have not only detected massive companions to massive galaxies, but have begun the onerous task of finding smaller companions and indications of galaxy-galaxy interactions. These discoveries have mainly resulted from the unprecedented imaging capabilities of ALMA at millimeter and sub-millimeter wavelengths and observations of the high-redshift universe (up to $z \sim 6$) can now probe down to spatial scales sufficiently small to detect and resolve faint companions.

Indeed, Bischetti et al. (2021) studied eight $2.4 < z < 4.7$ quasar host galaxies and found that 80% had at least one companion galaxy within $\sim 6 - 120$ kpc (projected distance). The companions detected in this study exhibited CO or [C II] emission line flux similar to their quasar companion. However, one companion Comp2$_{\rm J1549}$ to the quasar J1549+1245 was found to have continuum and CO(4-3) line emission at $\sim 17\%$ the strength of the quasar.

Díaz-Santos et al. (2018) used ALMA to observe 212 μm continuum emission in the Hot-DOG W2246-0526 at $z = 4.6$. Through these observations, the

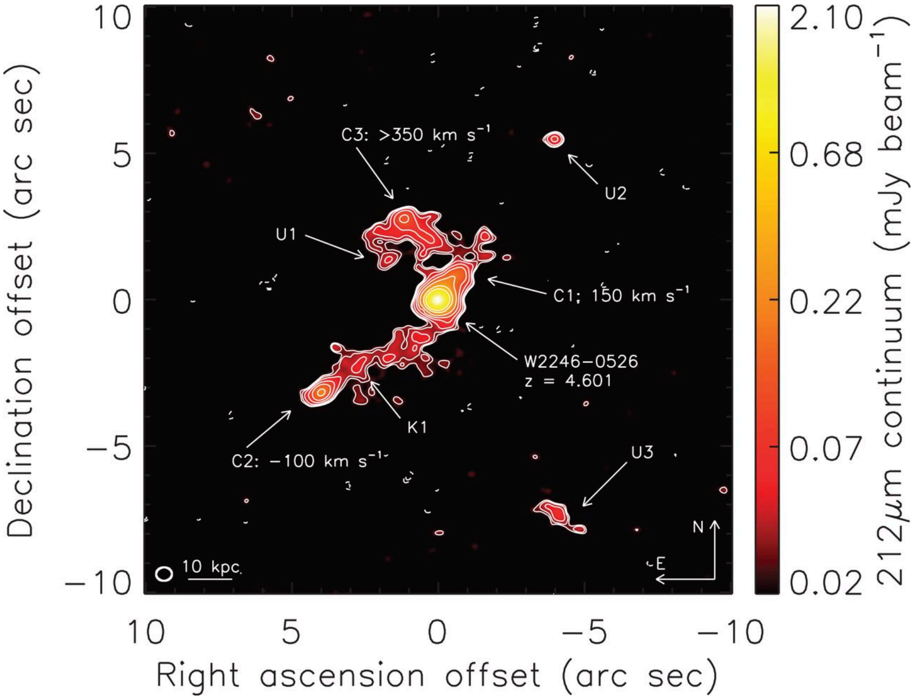

Figure 3.2: ALMA dust continuum image of the Hot DOG W2246-0526 system. The gas bridge-like structures can be seen between C1 and C2 with the central galaxy. A tidal structure is seen between C3 and W2246-0526. Figure from Díaz-Santos et al. (2018)

authors found three faint companions around the quasar with clear indications that these companions are interacting with the quasar. Continuum observations showed a dusty tidal structure between one companion and the quasar, and bridge-like structures of gas and dust between the two other companions and the quasar, shown in Figure 3.2. The dust mass in the gas bridge alone was found be to comparable to the dust mass of the three companions combined. A calculation of the velocity of the gas suggested that the sources are gravitationally bound and, similar to the quasar PKS1614+015, will be or are in the process of merging.

Another well-known example is the environment of the $z = 4.7$ quasar host galaxy BRI1202-0725. The quasar was previously known to be a system with a quasar and an SMG at a projected distance of 26 kpc (e.g., Omont et al. 1996). The ALMA observations used in the study detected two additional LAEs within a projected distance of 35 kpc (Carilli et al. 2013). Additionally, the authors found evidence of a possible gas bridge between the SMG and AGN, although they note that this could be an artifact caused by one of the LAEs.

Finally, the SMG AzTEC-3 holds significance for this thesis as it is the focus of Paper I. AzTEC-3 was discovered by Capak et al. (2011) and has been extensively studied since. The system has been deemed a 'protocluster', or a massive over-dense region in the high-redshift universe. In the case of AzTEC-3, this region extends out to > 2 Mpc encompassing three LBGs, one of which is thought to be composed of three smaller LBGs (Riechers et al. 2014). AzTEC-3 itself has an extreme star-formation rate ($> 1000\,\mathrm{M}_\odot\,\mathrm{yr}^{-1}$) the implications of such a rate clearly point to possible interactions as a source of gas-enrichment (Riechers et al. 2014). In addition, observations of CO(2–1), CO(5–4), and CO(6–5) have suggested that AzTEC-3 has an unusually high-excitation gas component for an SMG, possibly caused by gravitational interactions from companions (Riechers et al. 2010).

The preceding studies have substantiated the hypothesis of companions at $z < 6$; however, the number of $z \sim 6$ quasars with robust interferometric studies of their characteristics and environment have also been increasing rapidly in recent years (e.g., Decarli et al. 2017, 2019; Venemans et al. 2020; Mazzucchelli et al. 2019; Meyer et al. 2022a). Venemans et al. (2020) studied 27 quasars at $z \sim 6$ and found that 13 out of 27 had companion galaxies within 90 kpc. Neeleman et al. (2019) used ALMA observations to categorize [C II] emission from five quasar-companion systems at $z \sim 6$. The authors calculated dynamical mass estimates from the [C II] emission in both quasars and companions; on average, the dynamical masses were similar for both types of sources. Similar to the studies from Carilli et al. (2013), Husband et al. (2015), and Díaz-Santos et al. (2018), three of these quasar-companion systems exhibited gas between the two galaxies suggestive of tidal interactions. Meyer et al. (2022a) used ALMA observations of three $z > 6$ quasars to investigate the prevalence of companions (or lack-thereof).

The exact impact of the environment of high-redshift galaxies is yet to be determined, but it undoubtedly plays a major role in their evolution and star-formation. Deep, high-resolution studies with the focus of detecting the more difficult to observe faint companion galaxies will provide better constraints on the role of interactions and mergers. Observations of high-redshift massive galaxies with powerful interferometers such as ALMA and other next-generation telescopes will foster the conditions under which the true extent of the effect of companion galaxies on high-redshift galaxies can be quantified.

CHAPTER 4

OUTFLOWS & FEEDBACK

General references: Fabian (2012); Heckman & Best (2014); King & Pounds (2015)

The term feedback broadly encompasses astronomical phenomena relating to the re-distribution of momentum and energy. The main drivers for these processes are thought to be stellar winds, supernovae, and the central SMBH of the galaxy. The result of these effects on the contents of a galaxy have been further designated as either negative or positive feedback. Negative feedback refers to that which can suppress star formation in a galaxy, namely through driving out material or through heating the gas, and has been shown to have a profound effect on the properties of galaxies (e.g., Schaye et al. 2015; Hopkins et al. 2018; Pillepich et al. 2018). Positive feedback refers to phenomena such as jets causing star formation through their axis of propagation, as seen in Gaibler et al. (2011). It has even been proposed that star-formation occurs *within* the outflow itself, although this theory is controversial and requires additional investigation to determine its veracity (e.g., Maiolino et al. 2017; Gallagher et al. 2019). The exact role and ratio that these processes play in galaxy evolution is as of yet unknown, but their contribution is anticipated to be large (e.g., Hopkins et al. 2012; Agertz et al. 2013).

4.1 Stellar-driven outflows

Stellar lives are energetic processes and can dramatically affect the gas and dust in the interstellar medium (ISM) of their host galaxy. Stars tend to form and live in clusters (e.g., Lada & Lada 2003; Duchêne & Kraus 2013) and the following processes are mostly restricted to stars in that environment. Stars can drive turbulence and outflows in the following ways: protostellar outflows, stellar winds from young massive stars, core collapse supernovae, cosmic rays, radiation, type Ia supernovae, and stellar winds from old stars (e.g., Veilleux et al. 2020).

Perhaps one of the most iconic examples of this is the nearby galaxy M82. This galaxy has been called an 'archetypal example of a starburst galaxy' (Veilleux et al. 2020). M82 has a complex star formation history and a SFR of $13-33\,\mathrm{M}_\odot\,\mathrm{yr}^{-1}$

(Förster Schreiber et al. 2003b). A large starburst-driven outflow perpendicular to the disk of the galaxy is strongly seen in many wavelengths including X-ray and Hα optical emission with a mass loss rate of $1.4 - 3.6\,\mathrm{M}_\odot\,\mathrm{yr}^{-1}$ (Strickland & Heckman 2009).

4.2 AGN-driven outflows

Outflows and feedback from AGN are an important aspect of galaxy evolution. As noted in Chapter 2.4, theoretical models require feedback to produce the properties of local galaxies. It has been suggested that AGN feedback influences the sizes of galaxies, is responsible for the steep slope of the bright end of the galaxy luminosity function, the number density of AGNs, and enriches the IGM with metals (elements heavier than hydrogen and helium; e.g., Silk & Rees 1998; Hirschmann et al. 2014; Crain et al. 2015; Beckmann et al. 2017; Choi et al. 2018; Scholtz et al. 2018). Furthermore, the effects caused by the interactions of the central SMBH and the gas within the host galaxy are thought to play a major role in regulating star-formation within said galaxy; however, the true extent of this role is unknown (e.g., Di Matteo et al. 2005; Croton et al. 2006; Harrison 2017; Cresci & Maiolino 2018; Scholtz et al. 2020).

In many simulations of galaxy evolution the gas influx in the galaxy due to an interaction is funneled into the central SMBH. Feedback effects then remove and/or heat this gas - thus regulating star-formation - through two main modes; radiative and kinetic. These two classes are based on the Eddington ratio where the radiative mode occurs preferentially at higher Eddington ratios (see Figure 18 in Heckman & Best 2014). The radiative (quasar) mode of feedback occurs in galaxies with a large reservoir of cold and dense gas in their central region. This cold gas is channeled inwards to the central SMBH, subsequently heated by the SMBH, and cooled through radiative emission. The kinetic (radio) mode of feedback typically takes the form of powerful jets from the nuclear region of the galaxy. Gas funneled from the ISM toward the central SMBH is then ripped away by mechanical drivers, heating the gas to sufficiently high temperatures so as to prevent radiative cooling. Hence, the gas has been effectively removed from the galaxy, thereby contributing to the quenching of star formation.

4.3 Probes of outflows & turbulence

In the local universe, observing feedback effects and outflows from a galaxy is challenging but feasible from direct observations of the galaxy (e.g., M82; Strickland & Heckman 2009). In addition there are a wealth of spectral line observations that are simply unfeasible to observe at high-redshift due to their intrinsic faintness. An additional complicating factor is that the angular scale of observations at high-redshift is very limited compared to that of the local universe.

At high-redshift there are three main probes of outflows and feedback effects: P-Cygni line profiles[1], observations of spectral lines associated with outflows

---

[1] P-Cygni line profiles are characterized by a broad emission line that is accompanied by a

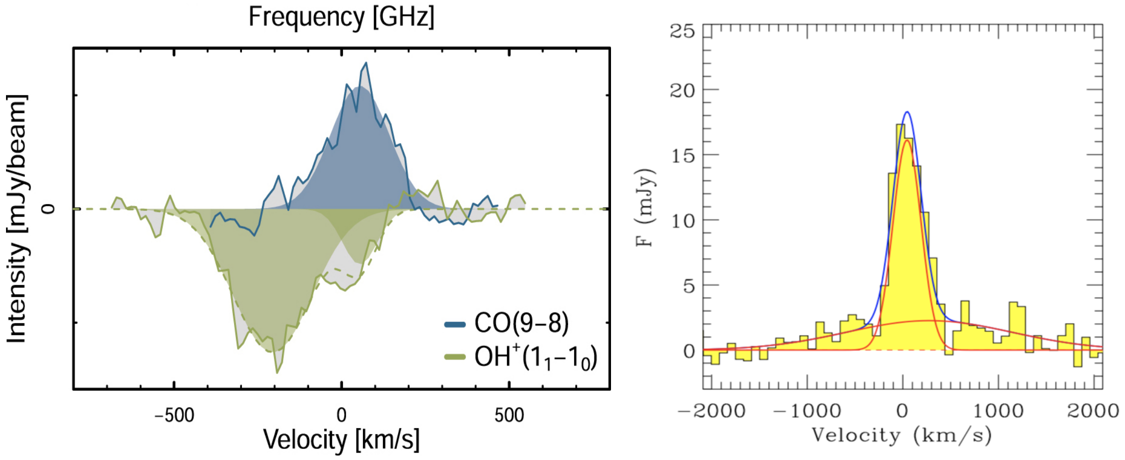

Figure 4.1: Left: Absorption line profile of OH^+ indicative of outflows, figure from Butler et al. (2021). Right: [C II] line profile suggesting a broad velocity component (Maiolino et al. 2012), though see more recent results from Meyer et al. (2022b).

(typically OH), and high-velocity wings on emission spectra (Figure 4.1). These probes have detected both neutral and ionized outflows in galaxies up to $z \sim 6$ (e.g., Maiolino et al. 2012; Cicone et al. 2015; Gallerani et al. 2018; Bischetti et al. 2019; Stanley et al. 2019; Ginolfi et al. 2020; Spilker et al. 2020; Butler et al. 2021; Spilker et al. 2025). However, both have clear drawbacks as well. The use of absorption signatures is contingent on strong continuum emission from the galaxy. The breadth of content traced by the [C II] line (through which high-velocity wings have been detected) including photodissociation regions (PDRs), neutral gas, and ionized gas, results in ambiguous conclusions about the origin of the outflow ([C II] emission is further discussed in Chapter 6.3.1.1).

In the local universe similar methods are utilized in detecting outflow signatures in galaxy spectra, however, the range of molecules available with which to detect these signatures dramatically increases. P-Cygni line profiles observed in a variety of far-infrared OH line transitions are a clear indicator of out-flowing material. The increase of tracers is best illustrated with the high velocity wings of spectra observed in local galaxies. This method has been used with CO, HCN, HCO^+, HNC, and more. Additionally, shock tracers such as SiO can be used to infer the presence of outflows due to the high temperatures and/or shock chemistry necessary to produce them (e.g., Martín-Pintado et al. 1997).

A perfunctory measurement is the mass loading factor, $\eta = \dot{M}_{\rm out}/{\rm SFR}$ where $\dot{M}_{\rm out}$ is the observed mass outflow rate of a galaxy and SFR is the star formation rate. This is a measure of the amount of gas that is blown out of the galaxy in relation to the amount of stars being formed and can therefore be seen as a measurement of whether star-formation quenching is ongoing. For $\eta > 1$ more mass is being removed from the galaxy than stars being formed and vice-versa for $\eta < 1$.

---

blue-shifted absorption component, an example of which is shown in Figure 4.1.

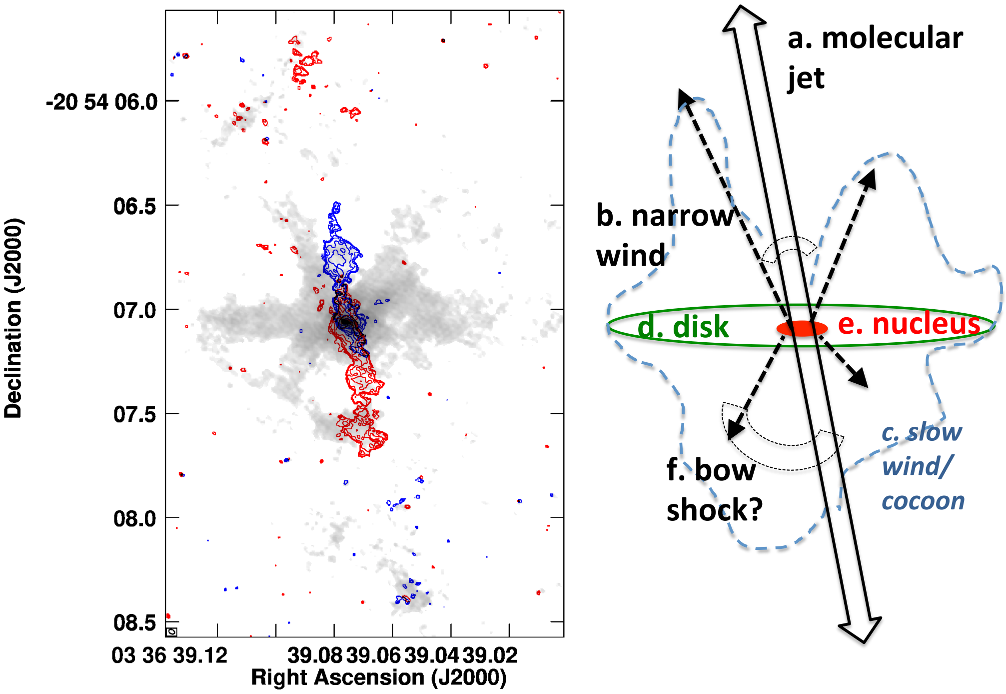

Figure 4.2: The molecular jet of NGC1377. Left: background gray shows CO(3–2) close to the systemic velocity for the source. The red and blue contours show the high velocity CO(3–2) emission in the red and blue wing of the spectra, respectively. Right: a mock-up of the components of the outflow. Figure from Aalto et al. (2020).

4.4 Observations of feedback & molecular gas outflows

4.4.1 Local universe

Observing outflows in the local universe is undoubtedly difficult, but these observations benefit from both images of the outflow and outflow signatures from spectra. Individual observations of specific galaxies can provide a detailed analysis of outflows in the studied objects while sample studies give the opportunity to characterize the properties of a population of galaxies.

Detections of high velocity wings in the spectra of galaxies in the local universe are becoming commonplace with a wide range of detections across molecular species (e.g., Feruglio et al. 2010; Alatalo et al. 2011; Aalto et al. 2012; Cicone et al. 2014). Cicone et al. (2014) used CO(1–0) observations of 19 ULIRG galaxies to conclude that although star-formation driven outflows were present and able to power massive molecular outflows, the effect of outflow enhancement from the AGN was significant.

A rather astounding example of the advantage of observing galaxies in the local universe is that of NGC1377. Aalto et al. (2020) combined observations of CO(3–2), HCO$^+$(4-3), and vibrationally excited HCN(4–3) to resolve the molecular jet extending from this galaxy. This outflow presents as a collimated jet extending 150 pc from the galaxy center, shown in Figure 4.2.

4.4.2 High-redshift universe

Direct observations of outflows in the high-redshift universe are more rare than in the local universe due mainly to observational difficulties. However, the number of known detections is increasing. For example, Maiolino et al. (2012) detected an extreme outflow in the quasar SDSSJ114816.64+525150.3 (hereafter J1148) at $z = 6.4$ with a mass-outflow rate of $\dot{M}_{\mathrm{out}} > 3500\,\mathrm{M}_{\odot}\,\mathrm{yr}^{-1}$ inferred from broad velocity wings found in the [C II] spectrum of the quasar. The extraordinary inferred mass outflow rate of this galaxy prompted additional studies of its properties and Cicone et al. (2015) re-estimated the mass outflow rate to be $\dot{M}_{\mathrm{out}} \sim 1400\,\mathrm{M}_{\odot}\,\mathrm{yr}^{-1}$. However, with recent data of improved quality, Meyer et al. (2022b) found no evidence of broad velocity wings in the [C II] spectra of J1148. This suggests that, for at least [C II] emission, additional factors may be at play and is discussed in Chapter 4.5.

Spilker et al. (2020) searched for outflows using OH observations in 11 lensed dusty star-forming galaxies at $z > 4$, and found evidence of outflows in eight of these galaxies. Riechers et al. (2021a) studied starburst galaxies in the range $2 < z < 6$ and detected OH^{+} emission or absorption in their sample of 18 starburst galaxies and found that the majority showed feedback signatures. The authors concluded that, based on the observed velocity shifts in the line profiles of the detected emission, this emission is evidence of outflows or inflows operating within the galaxies. Riechers et al. (2021b) studied the dusty starbursting major merger ADFS-27 ($z = 5.65$) and, using detections of OH^{+}, concluded that a major molecular outflow was occurring within the galaxy. Butler et al. (2021) studied the star-forming galaxy HATLAS J085358.9+015537 (G09v1.40, $z = 2.09$) and, through detection of OH^{+}, determined that the galaxy hosted a neutral gas outflow with a mass outflow rate of $83 - 25,400\,\mathrm{M}_{\odot}\,\mathrm{yr}^{-1}$. A compilation of molecular and neutral low- and high-redshift outflows from Butler et al. (2021) is shown in Figure 4.3.

Searches for outflows in the high-redshift universe have also utilized stacking methods, primarily through observations of the [C II] line, to amplify the signatures of outflows in less extreme objects. These approaches have led to conflicting conclusions. Gallerani et al. (2018) used ALMA observations of the [C II] line in nine galaxies at $z \sim 5.5$ with SFRs of $\sim 30\,\mathrm{M}_{\odot}\,\mathrm{yr}^{-1}$ and found an average inferred mass outflow rate of $\dot{M}_{\mathrm{out}} = 54 \pm 23\,\mathrm{M}_{\odot}\,\mathrm{yr}^{-1}$. Bischetti et al. (2019) and Stanley et al. (2019) present additional detections of outflows detected through stacking procedures of the [C II] line in galaxies at $z > 4$. However, Decarli et al. (2018) performed a stacking approach of [C II] in 27 quasars at $z > 5.9$ and found no evidence for outflow signatures in their line profiles.

4.5 Interpretation of observations

An additional important consideration in studying high-redshift outflows is the nature and origin of the outflow signature. Due to limited angular resolution at high-redshifts and the methodology of detecting feedback, it remains unclear to what extent observations have actually traced this phenomenon. The commonly used approaches for detecting outflows described above can be used regardless of the angular resolution - i.e., if broad velocity wings are detected in the integrated [C II]

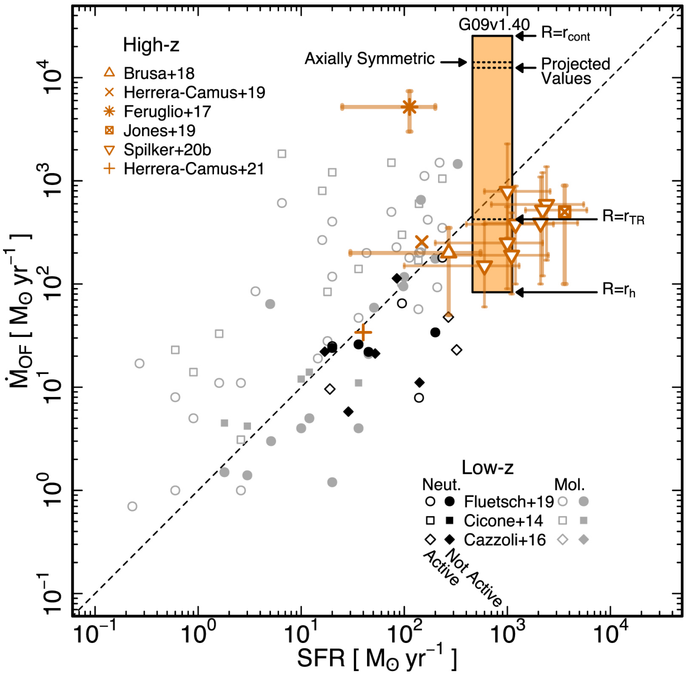

Figure 4.3: Mass outflow rate versus star-formation rate compiled from a variety of low- and high-redshift samples. The legend in the bottom right of the plot shows the known characteristics of the outflow for low-redshift samples and similar for the top right for high-redshift samples. Figure from Butler et al. (2021).

(or other line) spectra for an entire galaxy, this is typically attributed to an outflow signature. This leaves much room for interpretation of the source of this line profile feature. On the other hand, P-Cygni line profiles or lines known to be associated with outflows present a much more robust method of outflow determination in part due to the fact that the blue-shifted segment of the spectrum in P-Cygni profiles can be undeniably attributed to out-flowing gas.

The use of [C II] as a tracer of out-flowing gas has been contentious for quite some time. This was specifically called into question following the results of Spilker et al. (2020), where the authors did not find broad velocity wings in the [C II] spectra of their studied galaxies for which they had robust outflow detections from OH spectra. There are two easily discernible explanations for this discrepancy. The first being that it is possible previous studies which detected broad velocity [C II] emission in truth originated from an insufficient continuum subtraction prior to analysis of the line spectrum. This is unlikely to be the full explanation. However, it is possible that this, combined with the possibility that the [C II] line spectrum for a given galaxy could be contaminated by as of yet unknown faint or unresolved companion galaxies, could provide a more comprehensive explanation. Indeed, Gallerani et al. (2018) note that it is possible a portion of the excess line flux they attribute to outflow signatures could be due to faint satellite galaxies. Additional substantiation to the possibility of outflow signatures being biased by continuum subtraction is the case of J1148. New observations of J1148 from Meyer et al. (2022b), again using the Northern Extended Millimeter Array (NOEMA) but with increased coverage due to a higher number of antennas, of [C II] emission in the quasar did not demonstrate a need for the broad velocity component previously found; thus implying that there was no evidence of outflow signatures in the [C II] emission.

A final consideration is the overall effect of the outflow on the galaxy; that is to say, is there observational evidence of a significant alteration to the state of the galaxy by the outflow? For example, Scholtz et al. (2020) found no evidence of an instantaneous effect from ionized gas outflows in a sample of moderately luminous AGN between $z = 1.4 - 2.6$ (see also Scholtz et al. 2021; Lamperti et al. 2021). The authors suggest two possible explanations for this. Firstly, that the outflow does have an effect, but that effect is limited to spatial scales smaller than those they resolved ($< 5\,\mathrm{kpc}$). Secondly, that the effect of the outflow can only be seen on longer timescales. Regardless of the explanation, their findings demonstrate the need for additional studies on the effect of feedback on the host galaxy, origin of the outflow, and the veracity of previous outflow observations.

CHAPTER 5

GAS KINEMATICS

Similarly important to understanding the environment in which a galaxy grows is the study of it's internal dynamics. A key aspect in this regard are the gas kinematics, which have been studied on a wide redshift range. Studies of gas kinematics probe the rotational versus turbulent motions at work in galaxies. This can provide a measure of understanding for the lifecycle of the galaxy; for example, if a higher degree of turbulence is measured in a galaxy it can provide an indication that the galaxy may have recently undergone an interaction or merger. It should be noted that for this thesis (and broadly speaking for high-redshift studies), studies are limited to the kinematics of the gas and do not include, for example, stellar kinematics.

Galaxy gas kinematics are primarily studied through the rotational velocity of the gas, the turbulence (as measured by σ, the velocity dispersion), and the relative contribution of the ordered rotational movements to the turbulence (as measured by V_{rot}/σ). In addition to serving as a measure of the dynamical state of the galaxy, they provide a reference point for comparison between low- and high-redshift studies and among different high-z studies.

5.1 Gas kinematics at high redshift

The established paradigm through which massive galaxies in the high-redshift universe grow and evolve implies gas accretion from the IGM and through mergers. At high redshifts, the merger rate is known to increase (e.g., Engel et al. 2010; Fakhouri et al. 2010) and this means that the dynamical processes governing galaxies are expected to be different from those in the local universe. In terms of observables, this would correspond to an, on average, higher velocity dispersion (σ) and thereby an, on average, lower V_{rot}/σ value. Several studies using warm, ionized gas did indeed find that turbulence increased in galaxies from $z \sim 0$ to $z \sim 3$ (e.g., Wisnioski et al. 2015; Di Teodoro et al. 2016; Wisnioski et al. 2019; Übler et al. 2019). However, with powerful observatories that can observe resolved cold gas in high-redshift galaxies, such as ALMA and the launch of the *James Webb Space Telescope (JWST)*, these results have been challenged. Smit et al. (2018) used ALMA [C II] observations of two LBGs COS-3018555981 and COS-2987030247 at $z \sim 6$ and showed that there appeared to be ordered rotation already occurring in both of these high-redshift galaxies. Many additional studies have used observations of [C II] and have found increasing evidence that dynamically cold, rotationally supported disk galaxies are not uncommon at high redshifts, even out to $z > 7$ (e.g., Rizzo et al. 2020; Rowland et al. 2024).

Following the work of Smit et al. (2018), Rizzo et al. (2020) studied the kinematics of the gravitationally lensed $z = 4.2$ dusty starburst galaxy SPT–S J041839–4751.9 using non-parametric source plane lens modeling and found a $V_{\rm rot}/\sigma$ value indicative of a dynamically cold disk just 1.4 billion years after the Big Bang. Studies of larger samples have shown a similar trend of consistently higher $V_{\rm rot}/\sigma$ than expected (i.e., with $V_{\rm rot}/\sigma > 2$; e.g., Smit et al. 2018; Sharda et al. 2019; Neeleman et al. 2020; Rizzo et al. 2020; Neeleman et al. 2021; Lelli et al. 2021; Rizzo et al. 2021; Fraternali et al. 2021; Roman-Oliveira et al. 2023; Posses et al. 2023; Pope et al. 2023; Neeleman et al. 2023). The evolution of $V_{\rm rot}/\sigma$ with redshift from Rowland et al. (2024) is shown in Figure 5.1. It is clear that some galaxies out to $z > 7$ seem to be rotationally supported disks, which is supported by some simulation predictions (e.g., Kohandel et al. 2024).

Beyond global kinematic trends, recent targeted, individual studies have also begun to resolve more complex, internal morphological structures that further contextualize their dynamical state. Neeleman et al. (2023) used 400 pc imaging of the $z = 6.5406$ quasar P036+03 and found evidence of a warped disk. The authors argue that this warp could be caused by mergers/interactions but also could be an effect caused by gas deposits from the circumgalactic medium (CGM) onto the ISM of P036+03, where the latter situation is favored by their observations. Amvrosiadis et al. (2025) studied the kinematics of the strongly lensed dusty star-forming galaxy SPT-2147 at $z = 3.762$ and concluded that the residual velocities found in the kinematic modeling were indicative of a bar in the galaxy. Roman-Oliveira et al. (2023) studied a sample of 5 galaxies at $z \sim 4.5$ redshifts and found that the quasar BRI1335-0417 at $z = 4.4071$ showed indications of having a massive bulge at the center of the galaxy. All of these morphological structures have been studied in detail in the local universe, but have not been possible to identify in the high-redshift universe until recently.

These observational advancements have raised important questions about the ability of theoretical models to account for the formation of dynamically cold, rotationally supported systems at such early epochs. Some cosmological simulations have struggled to produce predictions for these galaxies (e.g., Pillepich et al. 2019) while others have found clear evidence for them. Kohandel et al. (2024) used the SERRA simulation suite (Pallottini et al. 2022) to show that, although dynamically cold disks were a reality in the high-redshift universe, the choice of gas tracer used to study the kinematics of the high-redshift galaxy played an important role in the categorization of the galaxy. Overall, while the general consensus is that these dynamically cold galaxies exist at very early ages, it remains unclear how many of these observed disks are real and how many are mergers or other interlopers confused due to observational difficulties.

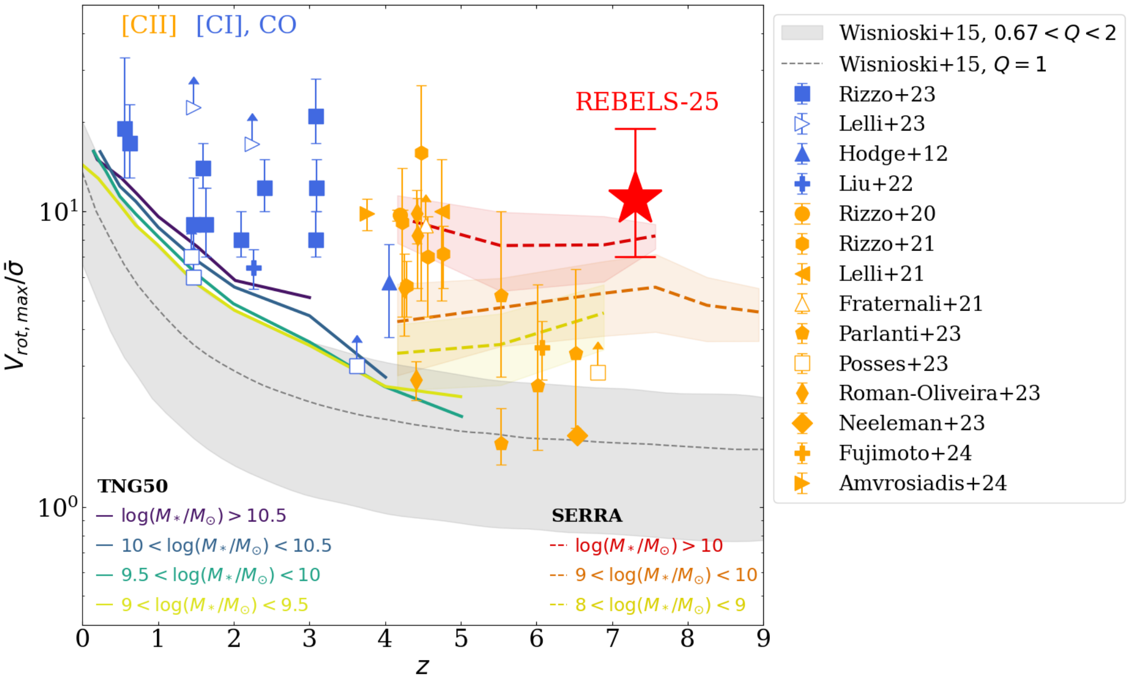

Figure 5.1: Evolution of $V_{\rm rot}/\sigma$ with redshift from Rowland et al. (2024). The empty markers indicate that one or more of the kinematic parameters were upper/lower limits. The gray, red, pink, and yellow shaded regions indicate predictions and associated uncertainties from simulations and models. The large red star shows the values found in Rowland et al. (2024) for the studied galaxy, REBELS-25 ($z = 7.31$).

5.2 Choice of gas tracer

In the local universe, HI and CO(1–0) are the obvious choices for tracing the bulk of the cold molecular gas emission. However, at high redshift, observations of HI become extremely challenging as the 21 cm emission line is redshifted to low radio frequencies, outside the frequency range of ALMA. Similarly, CO(1–0) emission is redshifted out of powerful observatories such as ALMA (note that with the coming online of band 1, it is now possible to observe CO(1–0) in specific redshift windows). Instead, higher-J CO transitions, [C II], or H α emission are commonly used to trace gas kinematics (e.g., Rizzo et al. 2020; Liu et al. 2023, Kade et al. submitted). However, each one of these tracers comes with caveats. Higher-J CO transitions trace warmer, denser gas, meaning that these lines may not trace the turnover radius of the rotation curve depending on the compactness of the gas, leading to the maximum rotational velocity being underestimated. Likewise, the velocity dispersion can be overestimated if the observed CO emission is tracing more turbulent gas, as would be expected with warmer, denser gas. [C II] emission traces multiple phases of the ISM, including both neutral and ionized gas. Finally, H α traces the ionized phase. While all these methods provide reasonable estimates of the gas kinematics, the wide range of measurements of different gas tracers across redshift range and population type make robust comparisons difficult to perform. Indeed, Kohandel et al. (2024) showed that, when using Hα emission, the velocity dispersion was significantly higher than the value found when using [C II] emission to study the same galaxy. This may provide an indication as to why studies using integral field unit (IFU) data of warm, ionized gas found higher amounts of turbulence in high-redshift galaxies compared to studies that used [C II] emission.

5.3 Resolution limitations

Observations of high-redshift galaxies are unable to resolve galaxies to the same spatial scales as in the local universe. For example, observations from the Physics at High Angular resolution in Nearby GalaxieS (PHANGS) survey mapped the kinematics in nearby galaxies down to 150 pc using CO(1–0) emission (Lang et al. 2020). Observations at such high angular resolution in the high-redshift universe are only possible with the aid of strong gravitational lensing; however, this technique introduces its own set of challenges which are discussed in the following subsection. Angular resolution limitations in particular have significant consequences for how well galaxy dynamics are interpreted, particularly when relying on kinematic moment maps.

It has been common at high-redshifts to use kinematic moment maps (i.e., moment-1 and moment-2 maps) to determine the kinematics of high-redshift galaxies. Although this methodology is typically performed by visual inspection, it has commonly been employed to discuss the dynamical state of high-redshift galaxies. For example, Smit et al. (2018) used kinematic maps to make a determination of the dynamical state of the studied LBGs. However, this approach suffers significantly when using lower angular resolution images. In fact, Simons et al. (2019) studied $\sim 24,000$ synthetic images and kinematic maps of high-resolution simulations of galaxies at $z \sim 2$ in a variety of different dynamical states ranging from isolated disk galaxies to mergers and found that up to 100% of these galaxies could be incorrectly classified as disks or mergers depending on the criterion selected and the spatial separation of the mergers. Rizzo et al. (2022) showed a similar rate of misclassifications in their work. The authors considered observations of galaxies from the SERRA simulations at a variety of different angular resolution mock ALMA observations and showed that with the angular resolutions common to high-redshift emission line studies, the rate of misclassifications could be up to 100% when only using kinematic maps. This is highlighted in Figure 5.2 which shows the kinematic maps of a disk galaxy versus a merging system in different angular resolutions. It is clear that even in higher angular resolution observations, it may be difficult to determine if the galaxy is a merger or a disk.

One solution to the need for high angular-resolution observations in order to make accurate kinematic determinations is observing gravitationally lensed galaxies. Since gravitational lensing magnifies the surface brightness of the emission, it can effectively boost the angular resolution of observations to otherwise unreachable scales. Under the assumption of a static magnification factor across an image, this improvement can be described for interferometric observations as $\theta_{\rm maj}/\sqrt{\mu} \times \theta_{\rm min}/\sqrt{\mu}$, where $\theta_{\rm maj}$ and $\theta_{\rm min}$ are the major and minor axes of the synthesized beam in interferometric images and μ is the magnification factor of the galaxy. Performing kinematic analyses of gravitationally lensed galaxies has become increasingly common and has been successfully performed in a number of different studies to identify disks and even provide indications of bars in high-redshift galaxies (e.g., Rizzo et al. 2020; Amvrosiadis et al. 2025). In addition, this method is of primary interest for this thesis as it is the focus of Paper III and is discussed in Paper IV.

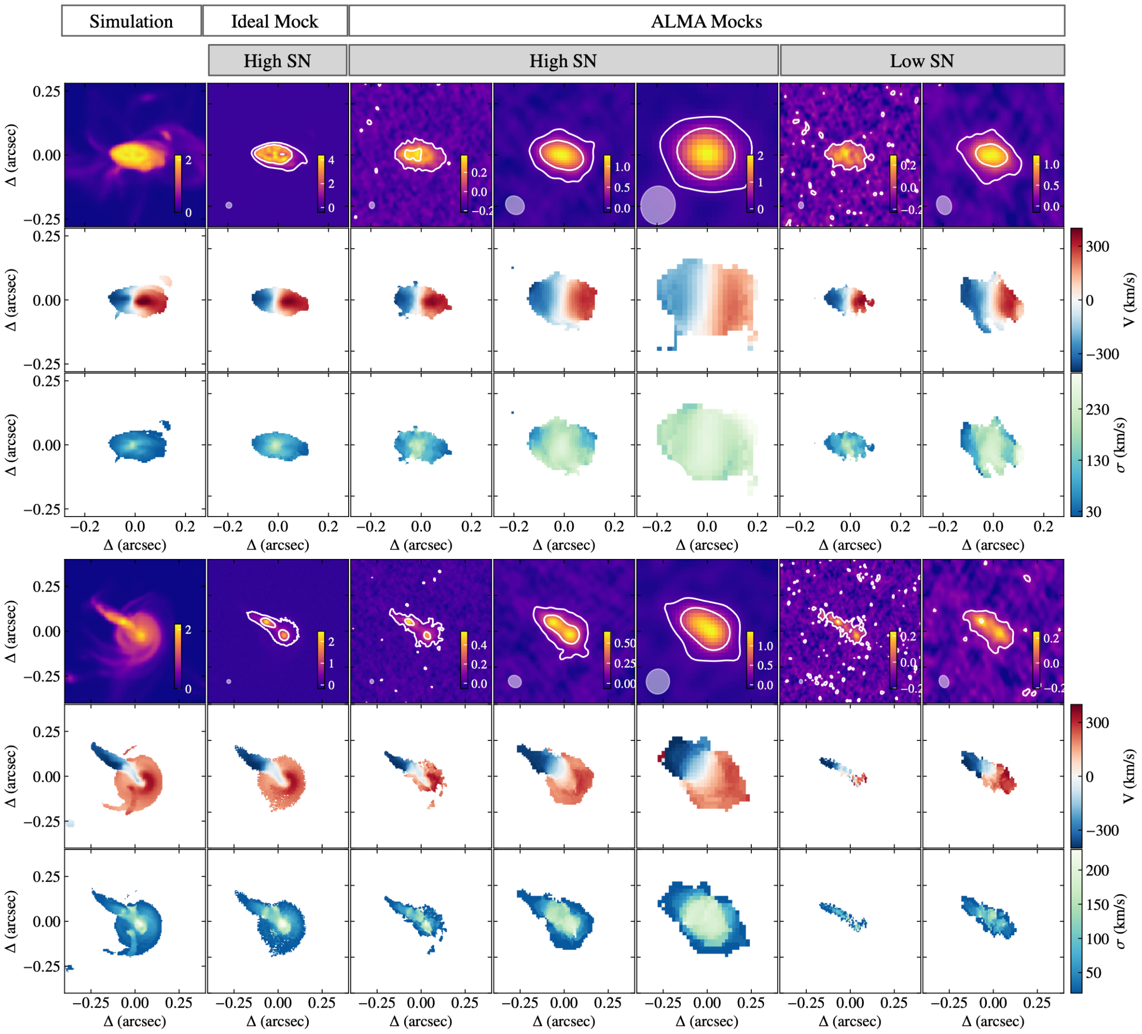

Figure 5.2: Example of the moment-0 (rows 1 and 4), moment-1 (rows 2 and 5), and moment-2 (rows 3 and 6) maps of simulated disk galaxy (rows 1-3) and a merging system (rows 4-6) in different mock ALMA observations at both low and high angular resolutions. Figure adapted from Rizzo et al. (2022).

5.4 Comparison & benchmarking

Observational advancements have progressed rapidly in the last decade, often outpacing our understanding of how robust the results from commonly used analysis tools actually are. Several aspects of how high-redshift data are analyzed further complicate comparisons, both between different high-redshift studies and with local universe galaxy populations. Primarily, this includes the two named above (i.e., gas tracer and observational angular resolution), as well as the tool used to perform the kinematic fitting, and the chosen method for computing the V_{rot}/σ value.

It has already been highlighted that the chosen gas tracer influences the degree of turbulence observed. Another aspect that influences the comparison, both qualitatively and quantitatively, is the choice of tool used to perform the kinematic analysis. There are a number of commonly used publicly available kinematic fitting tools such as GalPak (Bouché et al. 2015), QubeFit (Neeleman 2021), and $^{\mathrm{3D}}$Barolo (Di Teodoro & Fraternali 2015) that use different modeling routines and methodologies. The differences between these tools are not yet well understood and therefore the somewhat random usage of one tool over another is typically based on author preference, or familiarity, rather than a clear scientific basis. Work by Yttergren et al. (submitted) to quantify the differences between these tools should provide a better basis for the usage of one specific tool.

In terms of classification, there are small discrepancies between the exact classification scheme used to differentiate between disk galaxies and those dominated by turbulence. One common classification scheme classifies galaxies with $V_{\mathrm{rot}}/\sigma > 1.5$ as rotationally-supported galaxies whereas those with $V_{\mathrm{rot}}/\sigma < 1.5$ are classified as turbulence dominated. However, the exact V_{rot}/σ value can range between $1 < V_{\mathrm{rot}}/\sigma < 2$ for galaxies to be classified as rotationally-supported.

Together, these factors make it difficult to perform robust comparisons between different studies and samples. For example, Rowland et al. (2024) dedicate an entire discussion section simply to the selection of a representative comparison sample. Rowland et al. (2024) points out that one key difference in different studies is the number of independent sightlines in radio observations. $^{\mathrm{3D}}$Barolo uses a tilted ring model wherein each individual ring is optimized based on a number of input parameters, and is therefore sensitive to over- and under-fitting if too many or too few rings are used. Using a reasonable number of rings is particularly important for interferometric observations where pixels are correlated. Often in such cases, a ring separation of $\theta_{\mathrm{max}}/2.5$, where θ_{max} is the major axes of the synthesized beam from interferometric imaging, is used; but although this value is commonly adopted in the literature, there have been no systematic studies to determine if this or another value would be more accurate.

A final confounding factor is the use of gravitational lensing combined with kinematic modeling. The uncertainties on pixelized source plane reconstructions are often unreported in the literature and therefore it is difficult to evaluate the veracity of claims of studies using this methodology. As of the writing of this thesis, there has been no published benchmarking study that has systematically evaluated the accuracy of kinematic analyses based on source-plane reconstructions using commonly employed gravitational lens modeling codes.

In all, these factors highlight the urgent need to standardize commonly used methodologies and perform systematic benchmarking in order to robustly analyze and compare the kinematics of high-redshift galaxies.

CHAPTER 6

METHODOLOGY

6.1 Radio interferometry

General Reference: Wilson et al. (2013); Thompson et al. (2017)

Typical optical and single-dish radio telescopes are limited in resolution by their light collecting area - generally the diameter of the telescope. Hence, the angular resolution of these observations can be found by the simple relationship between the diameter of the telescope and the wavelength of the observation: $A_{\mathrm{R}} \propto \lambda/D$ where A_{R} is the angular resolution, D is the diameter of the telescope, and λ is the observed wavelength. A direct consequence of this is that achieving comparable angular resolution at longer wavelengths requires a significantly larger telescope diameter, and therefore dish size, than at shorter wavelengths. Radio interferometry is a method designed to overcome this limitation.

Modern interferometry works through a process called aperture synthesis to combine signals from radio dishes in a given array to increase angular resolution according to $A_{\mathrm{R}} \propto \lambda/L$ where L is the longest distance between two radio dishes. Thus, the angular resolution of interferometric radio observations is limited by the largest spacing between antennas in an array rather than any individual antenna diameter. This is a key advantage of radio interferometry from a practical standpoint as it allows for a large number of smaller dishes to achieve the same observing capabilities of a much larger single dish. Moreover, when large numbers of smaller dishes are distributed across large geographic areas, they effectively simulate a telescope much larger than could be physically constructed.

Aperture synthesis synthetically increases the apparent resolution by sampling the radiation field within the desired observation area using different pairs of telescopes or baselines. The sampling from each telescope pair, called visibilities, can be expressed as the following:

$$V_{j,k}(t) \propto \int_{sky} I(\vec{\sigma}) e^{\frac{-2\pi i}{\lambda} \vec{B_{j,k}} \times \vec{\sigma}} \, d\Omega, \tag{6.1}$$

where $V_{j,k}(t)$ is the visibility for telescopes j and k at time t, $I(\vec{\sigma})$ is the source brightness function, $\vec{\sigma}$ is the position vector, and $\vec{B_{j,k}}$ is the distance between the two dishes. The position vector, $\vec{\sigma}$, is typically constructed using a coordinate system designated by (l, m) and visibilities as:

$$\vec{B_{j,k}} \times \vec{\sigma} = \lambda(lu + mv) \tag{6.2}$$

such that the visibilities are then expressed in (u, v) space. This allows us to rewrite equation 6.1 as

$$V_{u,v} \propto \int_{sky} I(l, m) e^{2\pi i(lu+mv)} \, dl \, dm, \tag{6.3}$$

which is the standard 2D Fourier transform form of the visibility equation. Finally, we can invert this equation to write it as the following:

$$I(l, m) \propto \int V(u, v) e^{-2\pi i(ul+vm)} \, du \, dv \tag{6.4}$$

where $I(l, m)$ is the intensity function for a given position (l, m). The (l, m) plane refers to the image-plane and positions in the (u, v) plane refer to the uv-plane. It should be noted that there are two caveats to these equations. First, that the number of dishes in an array is not infinite and thus the sampling of the (u, v) space is limited to the number of samples as N×(N-1) where N is the number of dishes. Second, since each dish pair must have some distance between the two, the center of phase space, $u = v = 0$ remains unsampled, along with distances less than the smallest distance between two dishes. An example of uv-plane sampling is shown in Figure 6.1.

6.1.1 Radio imaging techniques

Since scientific analyses are typically performed in the image-plane, an efficient and user-friendly algorithm must be used to sample $I(l, m)$ for any given position in the observation. The most common method is by using an algorithm called the fast-Fourier transform (FFT). FFTs sample the uv-plane at regular intervals and convolve the sampling with the interval over which the sampling occurred and output a ‘dirty-image’ of $I(l, m)$. This dirty-image must then undergo a deconvolution process, typically CLEAN (Högbom 1974). CLEAN, and others of its kind, are designed to correct for insufficient sampling of the uv-plane.

CASA’s [1] TCLEAN is a commonly used algorithm to clean continuum and spectral line images. TCLEAN is an iterative process in which the emission from the brightest sources in the dirty image are progressively removed from the dirty images and added to a model images until a user-specified threshold is reached. The resulting model image is then convolved with the clean beam (typically an elliptical Gaussian fit to the main lobe of the dirty beam), and added to the residuals to produce the cleaned images generally used for analysis.

An important aspect of imaging is the weighting of the gridded visibilities when performing the FFT. Specific weights can be assigned to different visibilities,

---

[1] Common Astronomy Software Applications (CASA) is a software designed specifically to process interferometric data from telescopes such as ALMA or the VLA (CASA Team et al. 2022).

this is particularly useful when accounting for different noise variations or improving uv-dataset's sensitivity to extended structures or to improve resolution. The default weighting used by algorithms, such as TCLEAN, is natural weighting which assigns more weights to shorter baselines, leading to lower angular resolution but improved sensitivity to large scale emission. Generally, images using this algorithm have the best signal-to-noise ratio but poorer angular resolution. Alternatively, uniform weighting weights all visibilities equally, and therefore weights longer baselines more than shorter ones. An additional weighting scheme (utilized for data analysis in this thesis) is Briggs weighting. Briggs weighting allows for the user to choose a weighting scheme between natural and uniform weighting by using an adjustable parameter called the robust parameter, which varies between $+2$ and -2 and dictates the user's preference of being closer to uniform or natural weighting.

If a given observation is targeting an emission or absorption line, the continuum emission must be subtracted prior to determining the line flux. In radio and millimeter/submillimeter observations targeting spectral lines, any detected emission or absorption lines will appear as sharp peaks or dips, respectively, caused by a specific molecular or atomic transition. These features are effectively superimposed on top of the underlying continuum emission, which presents as a smooth background spectrum from, for example, thermal dust emission. In order to accurately measure the flux of any detected emission or absorption lines, it is first necessary to remove the continuum emission. For ALMA observations this is typically done using CASA's UVCONTSUB task. This task works by determining a fit for the underlying continuum emission using a polynomial of order n where n is specified by the user and fitting to emission line-free channels in the observation. Generally, a polynomial fit of $n = 1$ is sufficient to remove continuum (in cases where $n = 0$ is insufficient).

6.1.2 Radio interferometers

In the past decades a number of impactful radio interferometers have come online. A non-exhaustive list consists of the Very Large Array (VLA) in New Mexico, USA, e-MERLIN in the United Kingdom, the Australian Telescope Compact Array (ATCA) in Australia, the Northern Extended Millimeter Array (NOEMA) in the French Alps, the Atacama Large submillimeter/Millimeter Array (ALMA) in the Atacama Desert in Chile, the Low Frequency Array (LOFAR) with antennas located mainly in the Netherlands but also around Europe, and more. The next-generation of ratio telescopes and upgrades to those already in operation include the Square Kilometer Array (SKA), ngVLA, and the WSU ALMA upgrade. Below, we provide a more detailed description of the ALMA observatory, as it is the primary telescope used for the observations in this thesis.

6.1.2.1 ALMA

The observational power of ALMA is incredibly important for studying high-redshift galaxies. The different antenna configurations can result in arcsecond and sub-arcsecond resolutions, comparable to optical and near-infrared observations. The synthesized large collecting area made possible through interferometry means that, rather than being limited to observing the most luminous high-redshift galaxies,

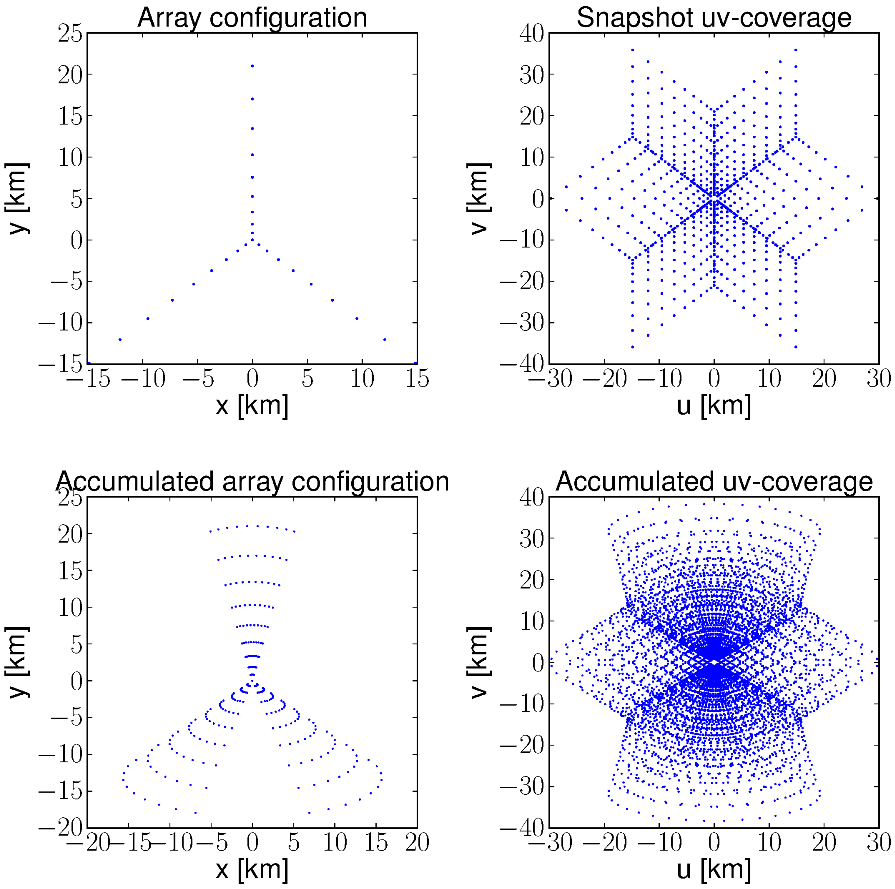

Figure 6.1: An example of a VLA configuration and the *uv*-coverage from that configuration as a snapshot, and accumulated array configuration and *uv*-coverage after 6 hours of integration including the increase in *uv*-plane sampling due to Earth's rotation. Figure courtesy of Lukas Lindroos.

ALMA can also probe down to more normal galaxy populations at and beyond cosmic noon ($z > 3$). The large spectral coverage, covering the majority of the wavelength range from 35 GHz - 950 GHz, means that far-infrared emission lines in high-redshift galaxies are redshifted into the frequency bands of ALMA receivers. In particular, [C II] and mid-J CO emission lines are redshifted to ALMA bands 4 to 7 depending on the redshift ($\sim 3 < z <\sim 5$). These lines are essential for determining the interstellar gas properties. Thus, it has now become possible to image the structure and environment of galaxies at many different evolutionary stages.

ALMA is composed of 66 radio antennas located in the Atacama Desert in Chile at an elevation of $\sim$ 5000 m above sea-level and is shown in Figure 6.2. The Atacama desert is one of the driest places on Earth and is thus ideal for radio interferometers sensitive to water vapor in the atmosphere. The telescope has two constituent arrays; fifty 12-meter dishes constitute the main observational array, used for interferometric observations, and the Atacama Compact Array (ACA) is

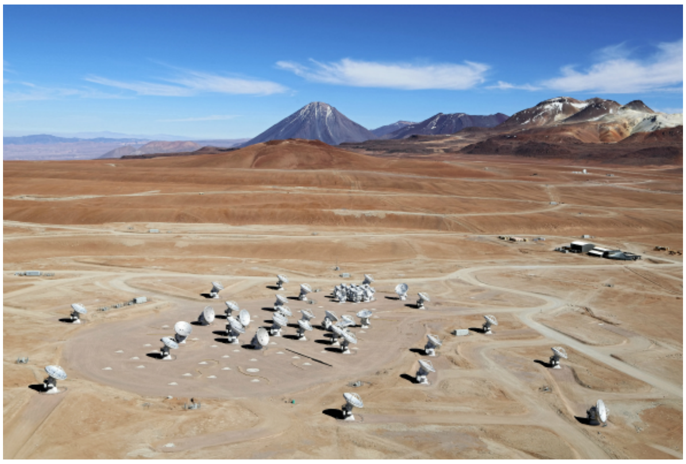

Figure 6.2: Aerial view of the ALMA telescope in the Atacama desert. Most dishes in the image are 12m main-array antennas while the small cluster in the center of the image are the 7m dishes of the ACA. Figure from Clem & Adri Bacri-Normier (wingsforscience.com)/ESO.

made up of twelve 7-meter dishes and four 12-meter dishes, used for Total Power observations. ALMA's dishes can be placed onto specific antenna pads, and antenna transports can move dishes to different pads to create different configurations and thus sample the *uv*-plane in a variety of ways. Observations with ALMA can, at the highest frequencies, reach down to spatial resolutions of 10 milliarcseconds, five times better than *Hubble Space Telescope (HST)* observations. ALMA will be the scientific workhorse of the millimeter/submillimeter astronomical community for years to come.

6.2 Gravitational lensing

General references: Futamase (2015); Schneider et al. (2006); Treu (2010)

Gravitational lensing is a natural phenomenon first predicted by Albert Einstein in 1936 and confirmed in 1979 (Walsh et al. 1979). Since then it has become an essential tool in observations of high-redshift galaxies and effectively acts as a magnifying glass on faint objects. In studies of individual high-redshift galaxies, strong gravitational lensing (lensing that produces double images or an Einstein ring) occurs primarily through galaxy-galaxy lensing or lensing of a galaxy by a massive galaxy cluster. In the galaxy-galaxy lensing scenario, a single massive galaxy is located in the foreground of the distant object. In the most extreme cases, the intervening mass causing the lensing is a galaxy cluster. A short introduction to gravitational lensing formalism is provided below.

A galaxy is said to be gravitationally lensed when it lies along the line-of-sight behind a more massive intervening object, such as a massive galaxy or galaxy cluster. The light from the distant galaxy is redirected around the intervening object and consequently distorted prior to reaching the point of observation. This holds under the thin lens condition: the thickness of the lens must be much smaller than the distance between observer and the deflector (massive galaxy or galaxy cluster) and the distance between observer and the background source. This condition holds in most astrophysical situations as the size of massive galaxies or even galaxy clusters are orders of magnitude smaller than the distances from the observer to those objects or to the background lensed source. Gravitational lensing has the advantage of preserving the surface brightness of the lensed galaxy while the magnification appears to make it look larger and hence brighter. This means that the physical properties of the lensed galaxy can still be studied in depth by simply correcting the brightness for the magnification factor (i.e., how many times brighter the galaxy appears). A schematic of a typical gravitational lensing system is shown in Figure 6.3. The lensing magnification, μ, can be described with the following equation:

$$\mu = \frac{1}{\det A} = \frac{1}{(1-\kappa)^2 - |\gamma|^2} \tag{6.5}$$

where A can be described by the Jacobian matrix,

$$A(\theta) = \frac{\partial \beta}{\partial \theta} = \delta_{ij} - \frac{\partial^2 \psi(\theta)}{\partial \theta_i \partial \theta_j} = \begin{pmatrix} 1-\kappa-\gamma_1 & -\gamma_2 \\ -\gamma_2 & 1-\kappa+\gamma_1 \end{pmatrix}, \tag{6.6}$$

where β and θ are the observed and true angular positions (see Figure 6.3), δ_{ij} is the Kronecker delta, γ_1 and γ_2 are the shear components defined by $\gamma \equiv \gamma_1 + i\gamma_2$ and κ is the dimensionless surface mass density or convergence,

$$\kappa(\theta) = \frac{\Sigma(D_\mathrm{d}\theta)}{\Sigma_\mathrm{cr}}, \tag{6.7}$$

where D_d is the distance between the observer and the lens, Σ_cr is the critical surface mass density defined as the following,

$$\Sigma_\mathrm{cr} = \frac{c^2}{4\pi G} \frac{D_\mathrm{s}}{D_\mathrm{d} D_\mathrm{ds}}, \tag{6.8}$$

where D_s is the distance from the observer to the source, $D_{\mathrm{d}s}$ is the distance between the lens and the source, c is the speed of light, and G is the gravitational constant. Finally, the Poisson equation[2] relates κ to ψ as $\nabla^2\psi = 2\kappa$. Lenses/deflectors where $\kappa \geq 1$, or $\Sigma \geq \Sigma_\mathrm{cr}$, somewhere in the lens plane will produce multiple images, and is the determining factor for whether that deflector produces strong or weak gravitational lensing.

The shear can be redefined as $g \equiv \frac{\gamma}{1-\kappa}$, called the reduced shear, and used so as to more easily understand the image distortions caused by the shear components,

$$A(\theta) = (1-\kappa) \begin{pmatrix} 1-g_1 & -g_2 \\ -g_2 & 1+g_1 \end{pmatrix}. \tag{6.9}$$

The $(1-\kappa)$ component can only isotropically stretch the image, whereas the shear components produce an elliptical stretching. For example, a circular source with a

---

[2] Note that this is very similar to a standard three-dimensional gravitational potential.

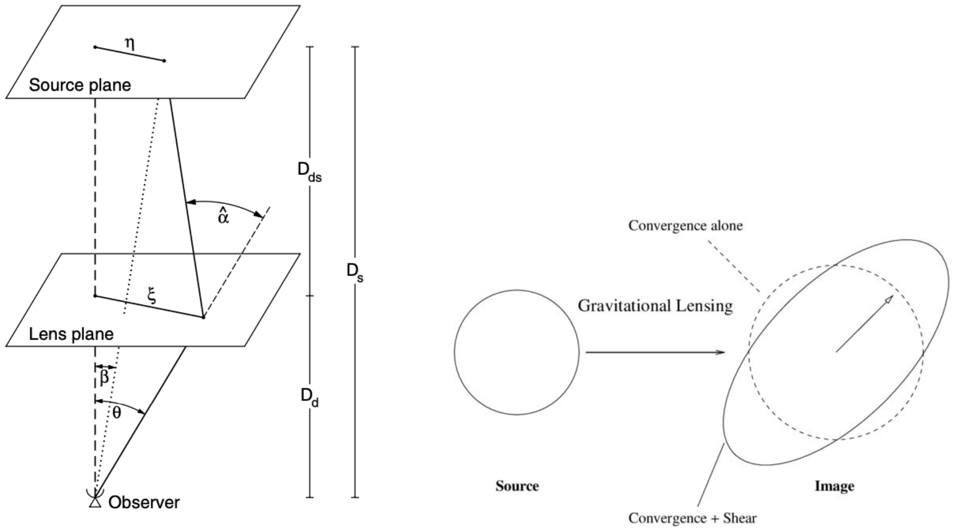

Figure 6.3: (Left) Figure demonstrating gravitational lensing, from Schneider et al. (2006). (Right) Figure demonstrating the effect of the convergence versus the shear, from Umetsu (2010).

radius of 1 produces ellipses in the image plane with axes $|(1-\kappa)(1+|g|)^{-1}$ and $|(1-\kappa)(1-|g|)^{-1}$. A visual description of this distortion is shown in Figure 6.3.

Regions of the image where det $A(\theta) = 0$ are referred to as critical lines, are closed, smooth curves. Using the lens equation, these map to caustic lines in the source plane. Along these curves $\mu = \frac{1}{\det A}$ is formally infinite, but as noted in Schneider et al. (2006), since all astronomical sources have a finite size, they will always have finite magnification, albeit this value can be very large. Note also that the number and location of images produced by a background source is dependent on its location relative to the caustic lines, see Figure 6.4.

6.2.1 Lens modeling

In order to calculate the magnification factor of a lensed object, it is first necessary to establish a mass model for the foreground source(s). This mass model uses information about the foreground mass(es) in tandem with how the background source(s) light is distorted to determine the magnification across a specified region. While large galaxy clusters are often obvious in, for example, optical images, determining the number of lenses can be difficult in cases where there is limited information known about the lenses; for example, if they only have photometric redshift measurements and/or are obscured in the observed wavelengths (e.g., Spilker et al. 2016). Hence, lens modeling often becomes an iterative process. In the occurrence of cluster lensing, the magnification factor can be extreme and the mass model used to describe the gravitational lensing will be extremely complex due to the large number of galaxies involved. Magnification factors of up to $\mu \sim 30$ have been observed resulting from cluster lensing (e.g., Ebeling et al. 2018).

Sophisticated lens modeling software provides a methodology for reconstructing the source and determining lens properties and magnification factors.

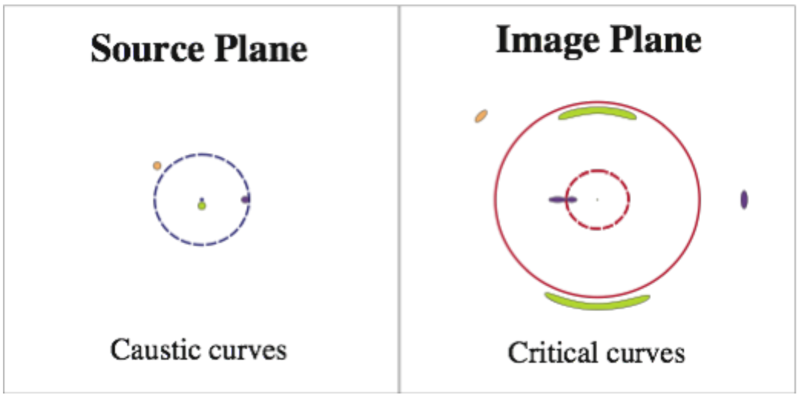

Figure 6.4: The critical and caustic curves from modeling a single circular lens. The left panel shows the source plane in which the blue dashed line is the caustic curves (note that the inner curve is sufficiently small that it appears as a dot) and the different colored blobs represent locations of flux from for example different locations within a larger galaxy or a number of smaller distant galaxies. The right panel shows the image plane in which the red solid and dashed lines represent the critical lines and the blobs and extended arcs show the location of the resultant flux post-lensing in the source plane of the background object(s). Figure from Futamase (2015).

There are a number of publicly available lens modeling software that are commonly used: Lenstool (Kneib et al. 2011) is typically used for optical images of large cluster lenses (e.g., Limousin et al. 2016), Visilens (Hezaveh et al. 2013; Spilker et al. 2016) and PyAutoLens (Nightingale et al. 2021) are adapted for interferometric observations and can perform lens modeling directly on the visibilities rather than images. This is necessary for interferometric images where every pixel is correlated and therefore performing lens modeling on the images themselves introduces bias. Visilens and PyAutoLens are of particular relevance to this thesis. Two methods of performing lens modeling are discussed in the following subsections.

6.2.1.1 Parametric modeling

In the case of parametric modeling, both the lens and source are described parametrically. There are a wide variety of mass models that can be chosen to represent the lens mass. One such commonly used mass profile is that of a single isothermal ellipsoid (SIE), parameterized in PyAutoLens as the following,

$$\mathrm{SIE} = (\frac{1}{1-q})(\frac{\theta_{\mathrm{E}}}{\xi}), \tag{6.10}$$

where q is the axis ratio, θ_{E} is the Einstein radius, and elliptical radius $\xi = \sqrt{x^2 + y^2/q^2}$ for mass center (x, y) (Nightingale et al. 2018). Similarly, Sérsic light profiles are often used to parameterize the source emission (and lens light emission when relevant) as follows,

$$I_{\mathrm{ser}} = I \exp\Big\{ -k \left[(\frac{\xi}{R})^{\frac{1}{n}} - 1 \right] \Big\}, \tag{6.11}$$

where (x, y) are the light center, $\xi = \sqrt{x^2 + y^2/q^2}$ and q is the axis ratio as above, I is the intensity at effective radius R, n is the Sérsic index[3], and k is a function of n (Nightingale et al. 2018).

Parametric modeling is time-efficient and effective, and typically provides reasonably good models of the lens and source magnification factor. Indeed, parametric models can be particularly useful when modeling lenses which have no observational counterpart (e.g., Spilker et al. 2016). However, there are obvious and significant drawbacks when modeling the source plane emission. For example, Kade et al. (2024) used the lens software Visilens to perform lens modeling of the quasar BRI 0952−0115 wherein the source was modeled by a single Sérsic profile. However, Kade et al. (2023) showed that BRI 0952−0115 has two close companions, evidence of an AGN, and evidence of outflow signatures. Hence, it is unlikely that a single Sérsic profile provides an accurate representation of the background galaxy, regardless of the goodness of the lensing fit. Therefore, it is necessary to use alternative modeling methods to create physically motivated reconstructions of the source plane.

6.2.1.2 Non-parametric modeling

Some sophisticated lens modeling software, such as PyAutoLens, allow for the reconstruction of emission in the source-plane using non-parametric modeling. These models have the benefit of not making an apriori assumption about the morphology of the galaxy. Hence, non-parametric models can recover complex or irregular structures such as jets, bars, and tidal features which would not be captured by analytical descriptions of the source. This is especially important when studying the internal structure and dynamics of high-redshift galaxies as these features can provide key information about star formation, feedback processes, and galaxy interactions.

Non-parametric modeling also has the advantage that it is possible to make source plane error maps with PyAutoLens, allowing for the significance of modeled emission in the source plane to be evaluated. Studies have shown that systematic errors are often overlooked and/or underestimated in lens modeling, and model misspecification is not insignificant when using parametric descriptions of lenses/sources in lens modeling and therefore these error maps give an indication of the systematic errors associated with the lensing analysis (e.g., Cao et al. 2022). Additionally, this approach preserves kinematic information throughout the modeling process, making it possible to generate source-plane emission cubes that can be further analyzed.

In non-parametric source-plane models, the source plane is modeled as an adaptive mesh which can adapt to regions of higher magnification, such as those near the caustic lines. The adaptive mesh is commonly chosen to be a Voronoi mesh wherein the pixels or cells of the mesh are polygons and the size of these polygons corresponds to the amount of magnification in that region of the image (i.e., smaller polygons in regions that have a higher magnification). In PyAutoLens, the smoothness of the images is regulated by a regularization coefficient which is used to prevent over-fitting.

---

[3] The Sérsic index ranges between $1 < n < 4$ where $n = 1$ corresponds to an elliptical light profile and $n = 4$ corresponds to a de Vaucouleurs light profile

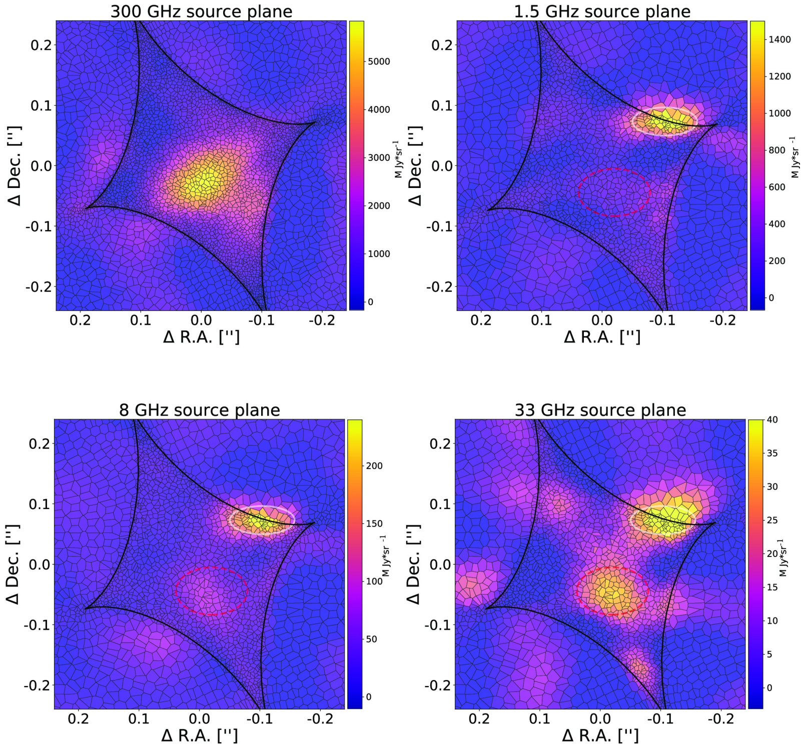

Figure 6.5: Non-parametric source plane modeling of the radio emission toward the Cloverleaf quasar. The radio jet can be seen in the white ellipses to the north-west of the central quasar (red ellipses) lying along the caustic line (shown in black). Figure from Zhang et al. (2023).

Studies using PyAutoLens and employing an adaptive mesh to model the lensed source(s) have shown that this methodology indeed recovers features that would be overlooked in typical parametric source modeling. For example, a radio jet has been discovered in the lensed Cloverleaf quasar at $z = 2.56$ using PyAutoLens's adaptive Voronoi mesh, see Figure 6.5 (Zhang et al. 2023). An additional example is that of the lensed galaxy SPT 2147 at $z = 3.762$. Amvrosiadis et al. (2025) used PyAutoLens to create a de-lensed source plane [C II] emission cube. Following a kinematic analysis using ^{3D}Barolo, the authors found evidence for a bar and a regularly rotating disk. PyAutoLens is extensively used in this thesis, particularly in Papers III and IV.

6.3 Probing the ISM of high-redshift galaxies

General references: Carilli & Walter (2013), Hodge & da Cunha (2020)

The ISM of high-redshift galaxies provides key clues to the ongoing evolutionary processes within them and a guide for characterizing them. The difficulties associated with observing high-redshift objects require unique and innovative methods of study. Attempts to study the faint emission lines and small spatial structures that can be resolved at lower redshifts are simply futile enterprises in the high-redshift universe. Only a few facilities are robust enough to detect, much less produce high quality images of, attributes of the ISM in these galaxies. This subchapter summarizes some of the tools available to study the ISM of high-redshift galaxies.

6.3.1 Atomic tracers

There exist a number of atomic tracers that are commonly used in studies of the ISM. The following two are fine structure carbon lines and are discussed due to their relevance to Paper I and II.

6.3.1.1 [C II] emission

The forbidden fine-structure [C II] 158 μm ($^2P_{3/2} \rightarrow^2 P_{1/2}$) emission line is one of the most commonly used tracers of gas in high-redshift galaxies due to its ubiquitous and bright nature. This line is one of the primary coolants in star-forming regions of the ISM owning to the fact that the ionization energy required to form [C II] is 11.3 eV, lower than that of neutral hydrogen at 13.6 eV (e.g., Stacey et al. 1991, 2010; Carilli & Walter 2013). [C II] emission traces both the cold neutral medium and photodissociation regions (e.g., Stacey et al. 1991). Stacey et al. (2010) suggested that, at high-redshift, [C II] emission originates primarily in PDRs in star-forming galaxies.

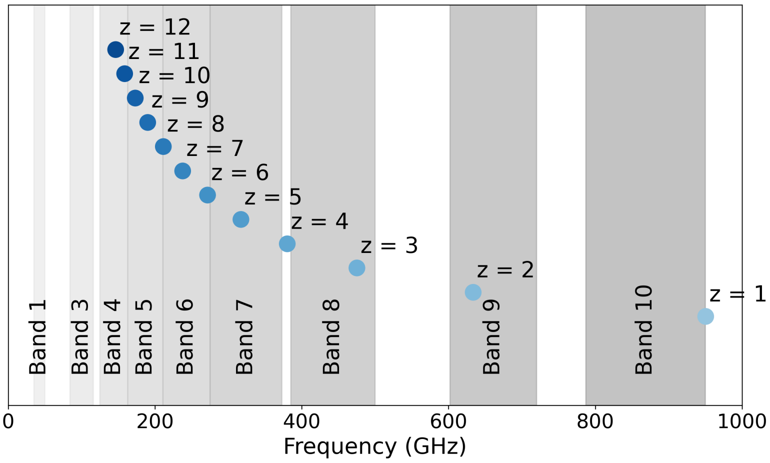

Figure 6.6: ALMA bands and [C II] 158 μm redshifted frequency for sources in the redshift range $1 < z < 12$. Figure produced by K. Kade for the purposes of this thesis.

Observations of [C II] are strategic not only because there is a high chance of detecting the line but also because its frequency is advantageous for high-redshift observations using ground-based radio facilities such as ALMA, VLA, or NOEMA. For these reasons, [C II] observations are typically the primary line emission observation carried out for galaxies at $4 < z < 7$. Figure 6.6 shows the ALMA bands and the redshifted [C II] frequency for galaxies across the redshift range $1 < z < 12$. The wealth of observations of this line have shown that there exists a brightness deficit of this line with respect to a galaxy's far-infrared (FIR) luminosity: [C II] line luminosity decreases with increasing FIR luminosity (e.g., Díaz-Santos et al. 2013). This deficit has been the cause of much debate since its discovery with, as of yet, no conclusion. Possible explanations include the physical scale of star formation, optical depth effects, saturation of the [C II] line, an increase in dust charge in the ISM, and AGN activity (Casey et al. 2014, and references therein). It has also been suggested that this deficit occurs preferentially in AGN host galaxies (e.g., Stacey et al. 2010). This deficit has been detected in a number of other fine structure lines (e.g., [N II], [N III], [O I], [O III]) at high redshift (e.g., Graciá-Carpio et al. 2011; Decarli et al. 2012; Farrah et al. 2013), suggesting that a systematic decrease in fine structure line emission with increasing FIR luminosity is occurring.

[C II] has also been suggested as a star-formation rate tracer with the possibility to be unbiased toward dust extinction as SFRs calculated from infrared luminosities tend to be (Lagache et al. 2018). This method has the caveat of depending strongly on metallicity (e.g., Vallini et al. 2015; Olsen et al. 2017), which can be equally difficult to categorize at high-redshift. Additionally, [C II] has recently been shown to be an inaccurate tracer of star formation in heavily obscured galaxies (e.g., Dwek & Arendt 2020). De Looze et al. (2014) studied the relationship between [C II] line emission and SFR for a variety of galaxy types in the local and high-redshift universe and determined correlations between the two depending on classification. This is rapidly becoming a common method of comparison at high-redshift for SFRs inferred from [C II] emission and inferred SFRs calculated from infrared luminosities from spectral energy distribution (SED) fits.

6.3.1.2 [C I] emission

There are two optically thin fine structure forbidden atomic carbon transitions that, when observed together, allow for the derivation of excitation temperature, neutral carbon column density, and mass independently of other line observations. These lines, [C I] ($^3P_1 \rightarrow ^3P_0$) and [C I] ($^3P_2 \rightarrow ^3P_1$) (hereafter [C I] (1-0) and [C I] (2-1)), have been shown to trace similar regions as CO(1-0) emission given that the critical density for both is similar, $n_{\rm cr} \approx 10^{-3}\,{\rm cm}^{-3}$; thus [C I] lines provide a method for tracing total molecular gas in a galaxy when CO(1-0) is unobservable due to its faintness or thought to be underestimated due to CO-dark gas (see Hodge & da Cunha 2020, and references therein). In cases where CO(1-0) and [C I] (1-0) emission are observed, these lines can be combined to confirm the $\alpha_{\rm CO}$ conversion factor (further discussed below; e.g., Cicone et al. 2018). In addition, the [C I] (2-1) line's emission frequency is very close to that of CO(7-6), which allows many CO surveys to obtain observations or constraints to the line without additional observation time. Studies using [C I], often in combination with other CO lines, have become increasingly commonplace for galaxies in both the local- and high-redshift universe (e.g., Walter et al. 2011; Krips et al. 2016; Cicone et al. 2018; Andreani et al. 2018a; Emonts et al. 2018).

There is sparse evidence showing that the properties of these lines evolve with redshift or with galaxy type (e.g., Gerin & Phillips 2000). When observed at very high-redshifts, this line is less contaminated by the CMB and is less sensitive to cosmic rays (e.g., Zhang et al. 2016; Andreani et al. 2018b). The [C I] gas mass of the galaxy can be calculated using the following equation from Weiß et al. (2003):

$$M_{\rm CI} = 4.566 \times 10^{-4} Q(T_{\rm ex}) \frac{1}{5} e^{T_2/T_{\rm ex}} L'_{\rm CI(2-1)} \tag{6.12}$$

where $Q(T_{\rm ex}) = 1 + 3e^{-{\rm T}_1/T_{\rm ex}} + 5e^{-{\rm T}_2/T_{\rm ex}}$ is the partition function, $T_1 = 23.6\,{\rm K}$ and $T_2 = 62.5\,{\rm K}$ are the respective excitation energy transitions of the [C I] (2-1) and [C I] (1-0) lines, and T_{ex} can be taken as the ratio of the two line transitions (e.g., Jarugula et al. 2021). The total molecular hydrogen mass can then be derived from $\rm M_{CI}$ by assuming a ratio of [C I] to H_2 typically using a template source (e.g., Weiß et al. 2003; Walter et al. 2011; Jarugula et al. 2021). This can then be converted to a total gas mass when taking into account the contribution from helium gas, and subsequent constraints can be placed on the galaxy's star-formation rate efficiency (also known as the depletion time). The star-formation rate efficiency can be described as the length of time for which a galaxy has the capability to form stars, or $t_{\rm dep} = M_{\rm gas}/{\rm SFR}$. This is an important ratio as it allows for a more accurate comparison to be made about the physical meaning of the gas content rather than a simplistic comparison between numbers. Current evidence points to a decrease in $t_{\rm dep}$ with redshift, but the exact rate of this decrease is contentious (e.g., Scoville et al. 2017; Tacconi et al. 2018; Liu et al. 2019).

6.3.2 Molecular tracers

6.3.2.1 CO emission

The ^{12}CO line J-transitions have long been the most commonly used probe of the ISM in both local and high-redshift galaxies. The J-transitions refer to the rotational transitions of the rotational quantum number J from one level to another. Different J-transitions trace different gas conditions and the CO spectral line energy distribution (SLED), or CO excitation ladder, is a powerful tool for analyzing the excitation sources within a galaxy. In addition, different categorizations of galaxies, such as SMGs, seem to have characteristic CO SLEDs that can be used to infer qualities about the galaxy class as a whole.

Low-J ($J < 4$) transitions are typically produced by excited gas in colder, more diffuse molecular clouds. Specifically, the CO(1-0) line allows for a determination of the bulk density of the molecular gas content in a galaxy through a conversion factor termed $\alpha_{\rm CO}$ as $\rm M_{mol} = \alpha_{CO} \times L_{CO}$ where $L_{\rm CO}$ is the CO line luminosity in units of $\rm K\,km\,s^{-1}\,pc^2$; thus $\alpha_{\rm CO}$ can be considered a mass-to-light ratio (e.g., Bolatto et al. 2013). This conversion factor is especially important due to the fact that H_2 has no permanent dipole moment, making it essentially impossible to observe in the millimeter/submillimeter and radio regimes, and thus determine its mass. This method has become somewhat contentious in past years for high-redshift galaxies due to its dependence on observations of the ground state CO(1-0) line which is onerous to observe at high-redshifts. Mid-J ($4 \leq J \leq 8$) transitions occur in warm molecular gas typically through excitation by UV photons in PDRs by OB type stars. High-J ($J \geq 9$) transitions typically require more extreme forms of excitation such as AGN activity.

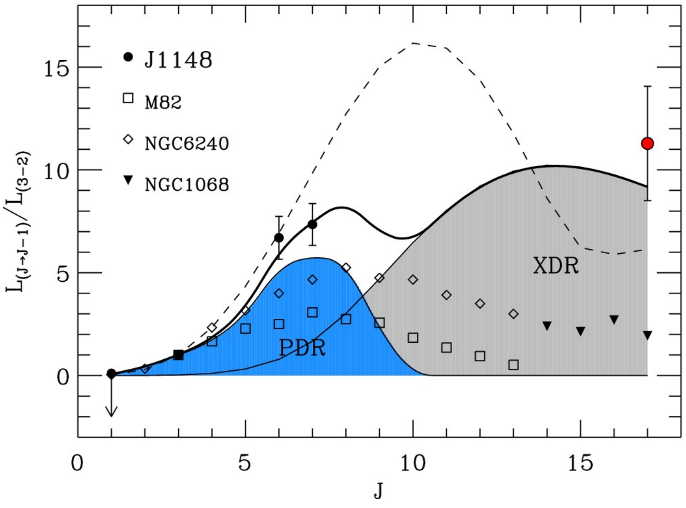

Figure 6.7: The CO SLED of the quasar J1148 and other local galaxies. The blue region under the black curve represents the flux which can be accounted for using PDR modeling and the shaded gray region represents that which required XDRs to produce. Figure from Gallerani et al. (2014).

CO SLEDs can be categorized by their peak, or which *J*-transition is brightest. Rosenberg et al. (2015) studied 29 LIRGs and ULIRGs in the local universe and found three typical CO-SLED classes. Class 1 peaks at CO(5-4), class 2 at CO(7-6), and class 3 exhibits a flat CO-SLED. These classes correlate to the heating mechanisms required to produce the CO SLEDs; class 1 required no additional heating than stellar UV-heating while class 3 required some form of AGN heating in combination with UV-heating. For class 2 objects, it was not possible to determine the heating mechanisms from the observations. At higher redshifts galaxies can peak at even more extreme CO transitions (e.g., Weiss et al. 2007).

Detections of high-*J* CO (J>10) lines have become increasingly common at high-redshift, and continue to increase (e.g., Gallerani et al. 2014; Li et al. 2020; Jarugula et al. 2021). Perhaps the most extreme of these is Gallerani et al. (2014) who detected CO(17-16) in the quasar J1148 at $z = 6.4$. Through radiative transfer modeling the authors determined that a PDR + X-ray dominated (XDR) model of the ISM was needed to generate such intense radiation fields (see Figure 6.7), thus providing evidence of the AGN's (the likely origin of the XDR) direct influence on the ISM.

However, CO SLED analysis alone has been shown to not always provide accurate constraints on the precise mechanisms heating the gas. Indeed, Mashian et al. (2015) showed in a diverse study of local galaxies that even with observations out to $J = 30$, it was not possible to constrain if the CO emission was due to star-formation related heating, AGN, or other heating mechanisms such as cosmic rays. This was further confirmed by a theoretical study from Vallini et al. (2019) where the authors showed that a number of different phenomena could impact the interpretation of the CO SLED. For example, the CO SLEDs of more compact star-forming galaxies could effectively mimic the CO SLED produced by AGN-host galaxies. This is clearly illustrated in Figure 6.8 which shows CO SLEDs out to

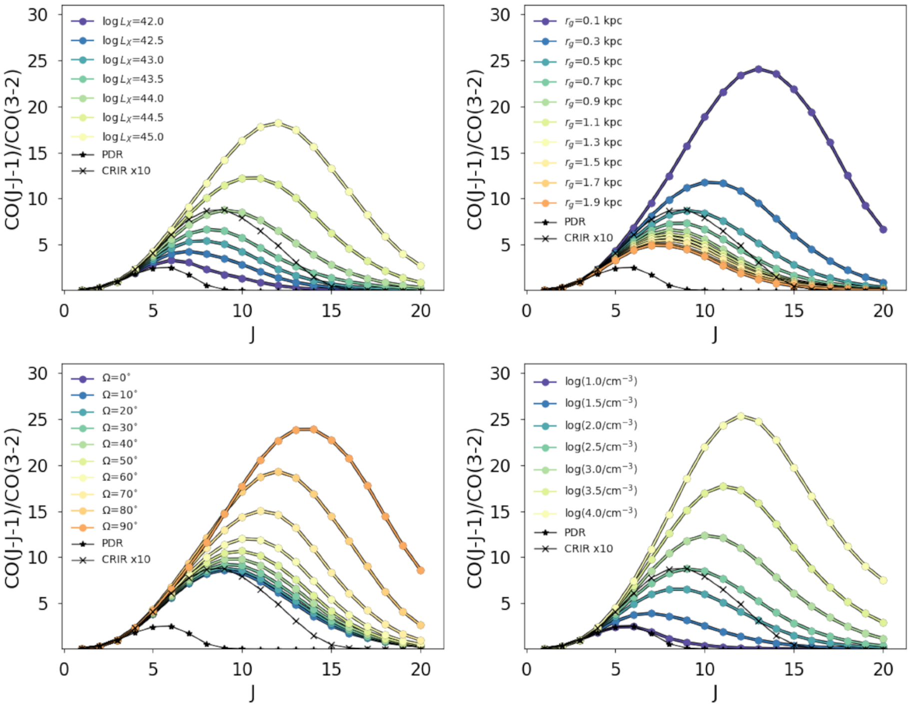

Figure 6.8: Effect of varying different properties of the simulated CO host galaxy: top left: AGN X-ray luminosity, top right: molecular gas disk size, bottom left: inclination angle of the obscuring torus, bottom right: mean density of the giant molecular clouds. Figure taken from Vallini et al. (2019).

$J = 20$ varying a variety of properties of the host galaxy such as the AGN X-ray luminosity and the mean density of the giant molecular clouds.

6.3.2.2 Water emission

Studies targeting water lines in galaxies at both low- and high-redshift have shown that, in the warm, dense, star-forming and shock-heated regions of the ISM, water is the third most abundant molecule (e.g., Bergin et al. 2003; Cernicharo et al. 2006; González-Alfonso et al. 2013) and a prime candidate for gas excitation studies. Water is divided into ortho- and para-transitions depending on the spin of the hydrogen atoms, and an important consequence of the nature of this division is that different water molecules are constrained to transitions only within the division the molecule belongs to (i.e., either ortho or para).

Liu et al. (2017) performed a detailed study of higher frequency water lines in galaxies at $z < 1$ and combined these observations with radiative transfer modeling to link different water transitions to different regions of the ISM based on temperature. Through these links the authors predicted line excitation intensities throughout the ISM, shown in Figure 6.9. The authors found that lines such as the H_2O ($2_{12} - 1_{01}$) transition are very bright in the cold, dense, extended region of the studied galaxies due to strong collisional excitation. Lines such as H_2O ($2_{02} - 1_{11}$) were found to be bright in both the warm and hot components of the ISM, but least affected by radiative pumping within the galaxy. In the warm, dense, and star-forming regions of the ISM young O- and B-type stars contribute heavily to UV radiation production, producing H_2O ($3_{12} - 3_{03}$). The authors found that the H_2O ($3_{21} - 3_{12}$) line was bright in both the warm and hot components of the ISM due to its ability to be excited through either collisional and radiative means. Finally, higher energy transitions (such as the H_2O ($4_{22} - 4_{13}$) line) required more intense excitation sources (i.e., were not found to be collisionally excited) such as XDRs, cosmic rays, or intense turbulence or feedback.

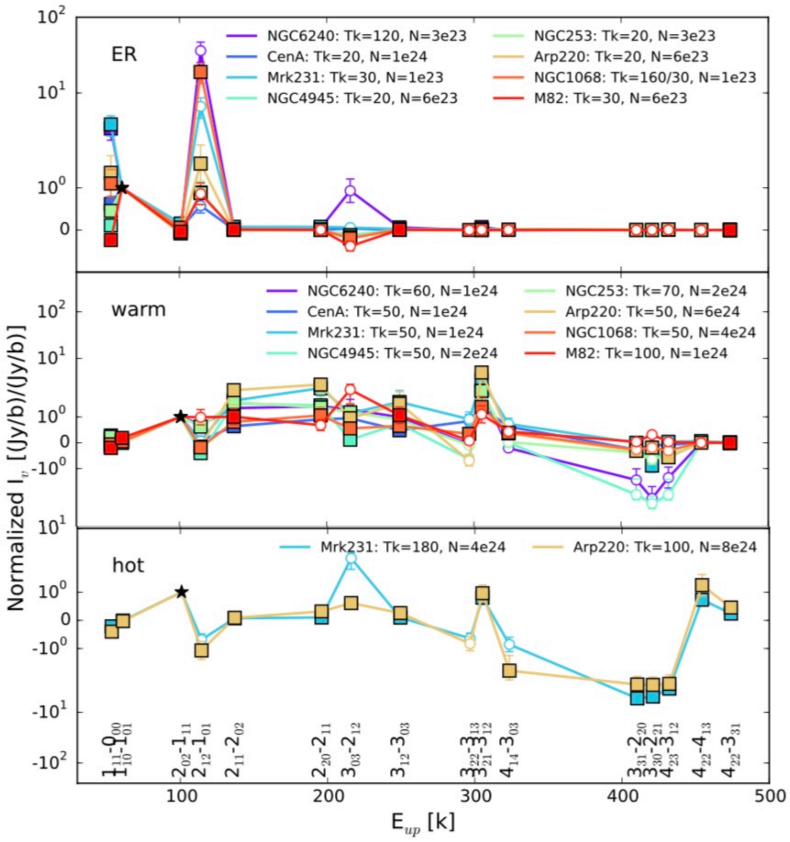

Figure 6.9: Water SLEDs for different ISM regions. From top to bottom: the cold extended region, the warm region, and the hot region. Observed transitions have been normalized to the H_2O ($2_{02} - 1_{11}$) line, designated by the black stars in each panel. Adapted from Liu et al. (2017).

Observations of these lines, in combination with radiative transfer modeling codes, can provide indications of the excitation sources within a galaxy required to produce such line intensities. One such example of this is the local ULIRG Mrk231 which has been detected in a wide variety of H_2O transitions. A thorough analysis of the water SLED using higher frequency water lines and subsequent SED decomposition by González-Alfonso et al. (2010) suggested that PDRs are insufficient to account for the observed H_2O flux. Alternative explanations are extreme outflows/turbulence and cosmic rays, or XDRs.

Yang et al. (2016) studied 11 hyperluminous infrared galaxies (Hy-ULIRGS) and ULIRGS at $z \sim 2 - 4$ and found that water emission was strongly correlated with $L_{\rm IR}$ in their sample with the relation $L_{\rm H_2O} \sim L_{\rm IR}^{1.1-1.2}$. This correlation is thought to originate due to the effect of infrared pumping of the water lines. Infrared pumping is a process by which water transitions at lower infrared frequencies 'pump' higher infrared frequency water lines, in effect synthetically boosting the intensities of certain transitions.

Water lines also provide an additional means of determining the SFR of a given galaxy using the the relations from Yang et al. (2016) and Kennicutt & Evans (2012) (e.g., Jarugula et al. 2021):

$$\mathrm{SFR}[\mathrm{M}_{\odot}/\mathrm{yr}] \sim 1.47 \times 10^{-10} \times \mathrm{L}_{\mathrm{IR}}^{1.1-1.2}[\mathrm{L}_{\odot}]. \tag{6.13}$$

This is particularly interesting as star-formation is thought to heavily affect the specific water lines which can pump other transitions. Water lines, especially in combination with other ISM tracers, may present the new frontier of ISM-diagnostic tools in the high-redshift universe. These lines provide the unique possibility of finally beginning to disentangle the affect of star-formation versus that of the SMBH on the ISM of high-redshift galaxies.

6.3.3 Dust

General reference: Galliano (2022)

Cosmic dust is a key ingredient in the ISM in spite of the fact that it makes up only about $\sim 1\%$ of a given galaxy's mass. Dust is made up of very small grains of matter with very complex morphologies on the order of $0.3\,\mathrm{nm} - 0.3\,\mu\mathrm{m}$ comprised typically of C, O, Mg, Si, S, F, or combinations thereof (e.g., Draine 2011). Dust grains are thought to play a number of significant roles in galaxy evolution.

The surface of dust grains can act as catalysts for chemical reactions. Namely, reactions that create H_2 molecules which are the most abundant molecules in the universe (e.g., Gould & Salpeter 1963; Bron et al. 2014) and hence the main component of the ISM (e.g., Hirashita & Ferrara 2002). Dust grains are a crucial component of star formation (e.g., Li & Greenberg 2002) and are primarily responsible for gas heating within PDRs (e.g., Draine 1978; Kimura 2016).

Although dust grains are immensely important in galaxy evolution, their presence contributes significantly to difficulties in directly observing star-formation in galaxies. Grains absorb the UV light rays from stars and re-emit their energy at longer wavelengths, reprocessing up to $\sim 25\%$ of a galaxy's stellar light into the infrared regime (e.g., Calzetti 2001; Bianchi et al. 2018). The obvious implication of this fact is that studies of a galaxy's dust properties yield information not only about the dust (such as dust mass, temperature) but also about the stellar population of the galaxy.

The effect of dust obscuration of a galaxy is constrained through analysis of its SED. The SED can be divided depending on the source of the emission, as shown in Figure 6.10. At shorter wavelengths unobscured stellar emission dominates the flux while at longer wavelengths dust re-emission of UV light is clearly the prevailing source of radiation. The dust-dominated region of the SED can be further partitioned into the Rayleigh-Jeans tail right of the peak of the dust emission and the Wien side to the left. The Rayleigh-Jeans tail is generally associated with colder dust whereas the Wien side is associated with warm dust. Dust has been observed

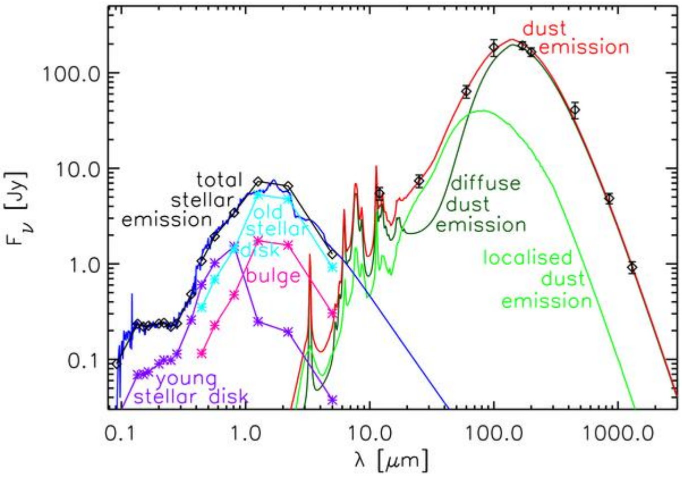

Figure 6.10: Best fit SED models for NGC 891 showing the different components including different dust components. Figure from Popescu et al. (2011).

in galaxies at large distances beyond $z \sim 7$ (e.g., Watson et al. 2015; Knudsen et al. 2017; Hashimoto et al. 2019; Tamura et al. 2019; Bakx et al. 2020; Harshan et al. 2024).

The star-formation rate of a galaxy can be inferred from a galaxy's SED using the above principles. Namely this is done by estimating the contribution of the stellar population to the dust-dominated regions of the SED as SFR $[\mathrm{M_\odot yr^{-1}}] \sim 1.47 \times 10^{-10}\,[\mathrm{L_\odot}]$ (Kennicutt & Evans 2012). However, it should be noted that different initial mass functions and conversion factors can be employed and influence the precise SFR obtained for a specific galaxy.

There are a number of open questions about the evolution of dust with redshift, including the dust production mechanism responsible for the higher than expected dust yields that have been found in distant galaxies. Another includes the evolution of the dust temperature, as probed by the peak of the dust-dominated region of the SED, and the dust emissivity power-law index (β). Dust SEDs, i.e., SED fitting covering the dust-dominated regime of a galaxy's SED, can be fit as a modified blackbody with the dust temperature (T_dust) and β as free parameters (note that other parameters can be assigned to be free parameters as well, such as the dust opacity).

At high-redshifts, the peak of the dust continuum emission is redshifted close to or into the ALMA bands and there have been a number of studies of the evolution of T_dust and β. At present, the exact evolution of these parameters is unknown. It is often assumed that both parameters should increase with increasing redshift and indeed some studies have found a clear increase in the dust temperature of high-redshift galaxies compared to studies of the local universe (e.g., Laporte et al. 2017; Bakx et al. 2020; Viero et al. 2022) while others find little evidence for a clear evolution (e.g., Drew & Casey 2022; Algera et al. 2024). Similar results have been found for β. Witstok et al. (2023) performed a comprehensive study of both parameters and found that there was no clear evolution of either parameter with redshift.

It should be noted that one possibility for the discrepancies found between different studies of an increase (or not) of dust temperature is the difficulty in observing the peak of the dust emission. Often studies rely on a limited number of datapoints covering the dust-dominated regime for SED fitting and therefore the SED fitting may be unreliable. However, with both ALMA and *JWST* now operational and dust formation processes an open research question, this uncertainty will be improved with future studies.

CHAPTER 7

RESULTS OF APPENDED PAPER

7.1 Introduction to paper I

Paper I aimed to place the SMG AzTEC-3 ($z = 5.3$, introduced in Chapter 3) and quasar BRI 0952−0115 (hereafter BRI 0952; $z = 4.432$) into the over-arching context of massive galaxy evolution in the high-redshift universe. Previous studies using ALMA observations of similar sources have begun to yield detections of smaller, fainter companion galaxies to massive high-redshift galaxies (e.g., Carilli et al. 2013; Riechers et al. 2014; Decarli et al. 2017; Díaz-Santos et al. 2018; Neeleman et al. 2019; Venemans et al. 2020). Bearing this in mind, an analysis of the environment of both AzTEC-3 and BRI 0952 was performed using [C II] line emission from high-resolution band 7 ALMA observations. These observations were originally intended to search for magnetic field signatures in either of these sources, seeking what would have been the first detection of magnetic fields at high-redshift. Thus, the integration time for the sources was quite high, a necessary condition for attempts to detect the desired companion galaxies.

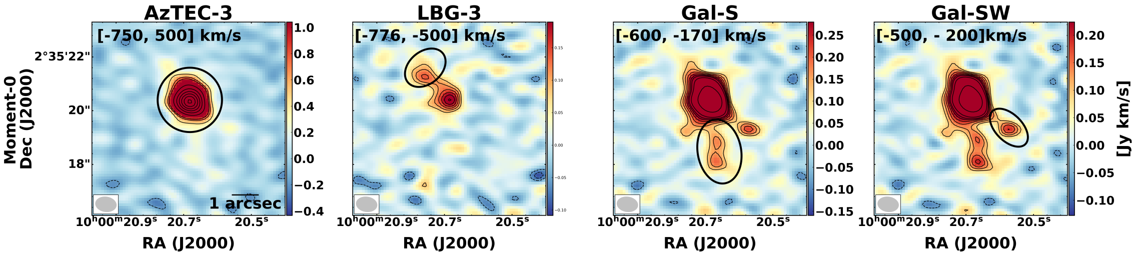

Figure 7.1: [C II] moment-0 map of the AzTEC-3 system for AzTEC-3, LBG-3, Gal-S, and Gal-SW. The top left corner of each image shows the velocity range from which the spectra was extracted for each source. The black circle for AzTEC-3 and ellipses for the remaining sources represent the regions from which the spectra of each was extracted. The contours are shown at $-3, -2, 10, 20, 30, 40, 50, 60\sigma$ levels for AzTEC-3 and $-3, -2, 3, 4, 5, 6, 7\sigma$ levels for the companions. Figure adapted from Kade et al. (2023).

7.2 Results of paper I

Paper I focused on three different aspects of BRI 0952 and AzTEC-3, each provided by the [C II] observations. These aspects were the environment in which these galaxies exist, outflow signatures in both of their [C II] line profiles, and a search for indications of magnetic fields in both galaxies. The main results are summarized below.

Three companion galaxies were detected in close proximity to AzTEC-3: Gal-S, Gal-SW, and LBG-3. Each of these companions are visible in *HST* imaging of the protocluster. LBG-3 was previously noted as a non-detection in [C II] with a 3σ upper limit (Riechers et al. 2014), and further investigated using Lyman-α emission by Guaita et al. (2022). An additional gas feature, possibly tidal in nature, between LBG-3 and AzTEC-3 was tentatively detected. This feature was also tentatively noted in Riechers et al. (2014) and was the subject of intense investigation in Guaita et al. (2022). A bridge of [C II] emission seems to connect Gal-S and AzTEC-3, in a similar manner to the gas-bridge structure detected in the Hot DOG W2246-0526 (Díaz-Santos et al. 2018).The companion galaxies to AzTEC-3 exhibit [C II] emission at $\sim 3\%$ that of the SMG. The moment-0 maps for the AzTEC-3 system are shown in Figure 7.1 and in Figure 7.2 for BRI 0952.

In the case of BRI 0952, the detection of a companion galaxy to the southwest of the quasar (Comp-SW) confirmed its tentative first detection by Gallerani et al. (2012). In addition, another source of emission is tentatively detected to the north of the quasar and is assumed to be a companion galaxy. These galaxies are not detected in *HST* imaging and are located at 0.7 arcseconds and 2.3 arcseconds, respectively, from the northern image of the doubly-imaged the quasar. They exhibit [C II] emission at about 4% that of BRI 0952.

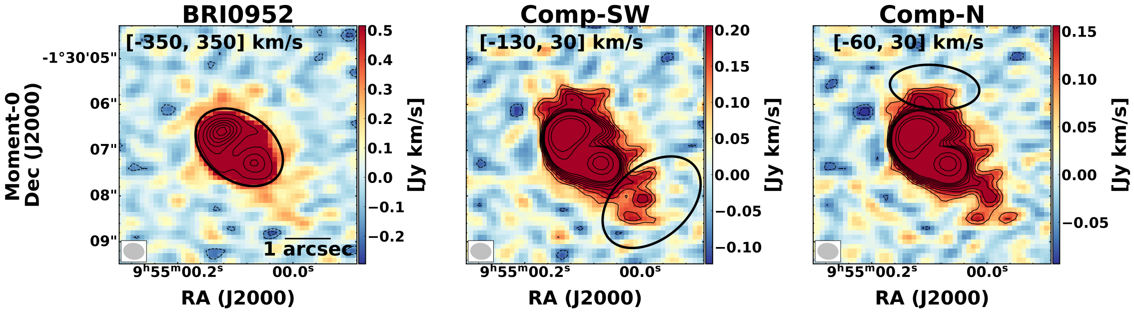

Figure 7.2: [C II] moment-0 map of the BRI 0952 system for BRI 0952, Comp-SW, and Comp-N. The top left corner of each image shows the velocity range from which the spectra was extracted for each source. The black ellipses represent the regions from which the spectra of each was extracted. The contours are shown at $-3, -2, 10, 20, 30, 40, 50, 60\sigma$ levels for BRI 0952 and $-3, -2, 3, 4, 5, 6, 7\sigma$ levels for the companions. Figure adapted from Kade et al. (2023).

The [C II] spectra of both galaxies exhibit high-velocity wings, regardless of the region of spectral extraction (i.e., the wings remain when the spectra is extracted from just the central region and when it is extracted from a larger region). This feature is generally interpreted as gas flows with high velocity and typically associated with outflows. For the purposes of Paper I, these wings were assumed to be a signature of outflows. However, we note the possibility that the wings are caused by a contamination of the [C II] line profile by the companion galaxies.

Under the assumption that these wings are indeed outflow signatures, we calculate the mass outflow rate using a spherical geometry following the procedure described in Maiolino et al. (2012), Cicone et al. (2015), and Stanley et al. (2019). This results in a mass outflow rate of $\dot{M}_{\rm out} = 258 \pm 29\,{\rm M}_\odot\,{\rm yr}^{-1}$ for AzTEC-3 and $\dot{M}_{\rm out} = 97{\pm}18\,{\rm M}_\odot\,{\rm yr}^{-1}$ for BRI 0952. In the case of BRI 0952, this value is lower than those found for quasar-driven outflows (e.g., Feruglio et al. 2010; Sturm et al. 2011; Cano-Díaz et al. 2012; Maiolino et al. 2012; Cicone et al. 2015; Feruglio et al. 2015, etc.), but in good agreement with results from stacking approaches (e.g., Gallerani et al. 2018; Stanley et al. 2019; Ginolfi et al. 2020).

An SED fit was performed for both galaxies, and thus a SFR calculated. Both galaxies have high SFRs (BRI0952: $\sim 770\,{\rm M}_\odot\,{\rm yr}^{-1}$ and AzTEC-3: $7340\,{\rm M}_\odot\,{\rm yr}^{-1}$). We fit simple modified black body approximations to find an approximate $L_{\rm IR}$ for the companion sources for both. Additionally, we investigate the [C II] deficit and find that in AzTEC-3 and BRI 0952 this deficit is similar to other high-redshift galaxies but that the companions compare better to local galaxies (i.e., exhibit a smaller deficit).

We calculated the virial mass from the FWHM of the [C II] line following the procedure described in Riechers et al. (2014) to estimate the mass of the respective companion galaxies of both AzTEC-3 and BRI 0952. We find that they have masses of $\leq 4\times$ for that of AzTEC-3 and $\sim 1.5 - 2\times$ for that of BRI 0952. We note the caveat that the masses of the companions of BRI 0952 are likely overestimated as we do not correct for lensing when calculating their mass; however, given that FWHM measurements are largely unaffected by lensing effects, this overestimation is not likely to be large. In the case of AzTEC-3, the observation of features linked to interactions suggest that these companions may be in the process of merging with the SMG, and their masses classify them as minor mergers.

Based on theoretical predictions that [C II] may trace magnetic fields (e.g., Yan & Lazarian 2012; Zhang et al. 2015; Zhang & Yan 2018), the observations were designed to constrain the magnetic fields of both AzTEC-3 and BRI 0952. However, the full polarization data yielded a non-detection. Limits on the B-field are given in Table 2 in Paper I.

The results of this study demonstrate the striking ability of ALMA to detect and (at least partially) resolve very faint companion galaxies in the high-redshift universe. The extreme star-formation rates of BRI 0952 and AzTEC-3 indicate their need for gas obtainment and thus raise the question of the role of their faint companions in their evolution. Future deep high-resolution ALMA observations of similar galaxies in the high-redshift universe will uncover the role and ubiquity of faint companions in the years to come.

My contribution to Paper I included performing the full analysis of the data including imaging, continuum subtraction, source detection, spectral and continuum analysis, lens modeling, SED fitting (only for AzTEC-3), star-formation rate calculations, mass-outflow rate calculations, and dynamical mass calculations. The observations were reduced and calibrated by ALMA and the regional center ARC

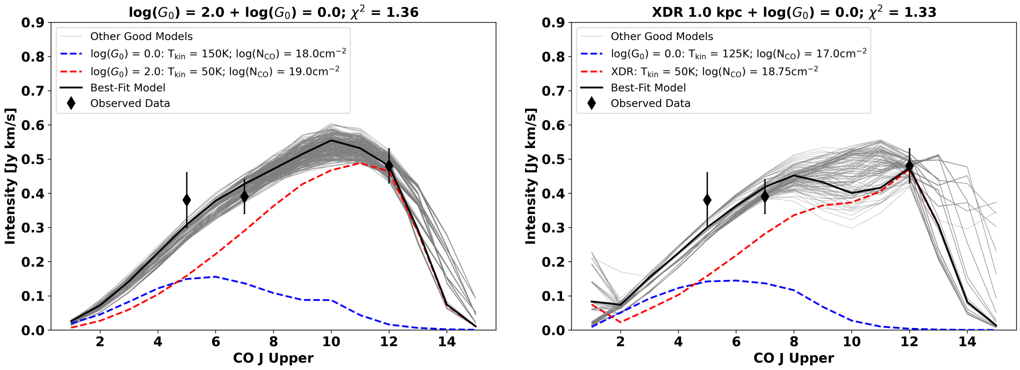

Figure 7.3: CO SLEDs using a two-component description of the ISM using a combination of PDR+PDR heating (left) or PDR+XDR heating (right). The solid black line shows the best-fit composite model while lighter gray lines show other models within 1σ. Figure adapted from Kade et al. (2024).

node. I was not involved in the polarization results and the magnetic field analysis, this was performed by a co-author. Additionally, SED fitting of BRI 0952 was performed by a co-author. I wrote the manuscript text with the exception of subjects relating to magnetic fields.

7.3 Introduction to paper II

Paper II focused on the bright, lensed quasar BRI 0952 at $z = 4.432$ with a previously estimated gas mass of $M_{\mathrm{H_2}} \sim (2-3) \times 10^9\,\mathrm{M_\odot}$ (Guilloteau et al. 1999) and a star-formation rate previously estimated at $\sim 270\,\mathrm{M_\odot\,yr^{-1}}$. BRI 0952 is lensed by a line of sight galaxy at $z = 0.632$ (Eigenbrod et al. 2007) with previous estimates placing the magnification factor $\mu \sim 6.7$ (Gallerani et al. 2012). The lensing has produced a double-image system referred to as the top and bottom images of the quasar. This galaxy was strongly detected in [C II] emission by Maiolino et al. (2009) and Gallerani et al. (2012). Paper II aimed to combine the high-resolution [C II] observations of the quasar BRI 0952 used in Paper I with bands 3, 4, and 6 ALMA archival observations to determine the ISM properties of the quasar. In particular, to determine the individual roles of the AGN, ongoing star formation, and the environment (i.e., nearby companions from Kade et al. (2023)).

7.4 Results of paper II

The ALMA archival observations yielded serendipitous detections of CO(5–4), CO(7–6), CO(12–11), [C I] (2-1), an quadruplet of hyperfine $\mathrm{OH^+}$ $(1_2 - 1_1)$ transitions, an OH doublet, $\mathrm{H_2O}$ $2_{11} - 2_{02}$, and the previously detected [C II] emission reported in Kade et al. (2023). We used these line detections to investigate the differing heating mechanisms at play within the quasar and to estimate physical properties of the quasar such as the gas mass and depletion time.

We used the [C I] (2-1) emission to calculate the gas mass in the quasar and found a total H_2 gas mass of $(6.2 \pm 4.9) \times 10^{11}\,M_\odot$. Using the SFR from the infrared luminosity and the SFR calculated from the [C II] emission, both calculated in Kade et al. (2023), we found a depletion time of $t_{\rm dep,\mathit{L}_{IR}} \sim 8$ Myr and $t_{\rm dep,[CII]} \sim 25$ Myr. Both values are significantly lower than what has commonly been found for galaxies at similar redshifts. We found that the H_2O emission is likely correlated with ongoing star formation in the quasar given that the quasar followed the previously found H_2O -$L_{\rm IR}$ correlation (e.g., Yang et al. 2013, 2016) when using the infrared luminosity from star formation from SED fitting (i.e., the infrared luminosity decoupled from the assumed contribution from the AGN). Further, we found clear signatures of the AGN in the SED fitting performed, as also noted in Kade et al. (2023).

We used the radiative transfer modeling code MOLPOP-CEP (Asensio Ramos & Elitzur 2018) to constrain the properties of the CO emission. We investigated a variety of PDR models of varying strengths and XDRs with varying distances from the assumed CO emitting region. We found that a two-component model of the ISM was necessary to model the CO emission, but that the nature of these two components remain unclear with the current data. In particular, the difference between a PDR-PDR model and a PDR-XDR model is marginal, see Figure 7.3. We performed a Bayesian likelihood analysis for the different models and show that there is indeed little statistical difference between the PDR+PDR versus PDR+XDR two-component models. This highlighted the need for additional atomic and molecular line emission to distinguish between the different heating mechanisms at work in the quasar, beyond the emission lines already detected in BRI 0952.

We hypothesized that BRI 0952 is in a state of transition from a starburst-dominated phase to an AGN-dominated one. This is motivated by the high star-formation rate, the close companion galaxies, clear AGN signatures, and CO SLED which demonstrated that the gas heating mechanisms could be either AGN or star-formation driven. We suggest that more in-depth studies of individual galaxies, now possible with ALMA and *JWST*, are key to better understanding the ISM of high-redshift galaxies.

My contribution to paper II included performing the full analysis of the data including imaging, continuum subtraction, source detection, lensing, spectral, and continuum analysis. A. Bewketu Belete generated the MOLPOP-CEP models and I performed the analysis of the models to determine the best-fit combination for BRI 0952. I also performed the Bayesian likelihood analysis and all other calculations performed in the paper. I wrote the manuscript, with the exception of Section 4, for which A. Bewketu Belete provided some initial text.

7.5 Introduction to paper III

Paper III focused on the strongly lensed SMG H-ATLAS J083051.0+013224 (hereafter, G09v1.97) at $z = 3.63$. G09v1.97 is a hyper-luminous infrared galaxy (HyLIRG) with an intrinsic infrared luminosity of $\sim 10^{13}\,L_\odot$ and a very high SFR of $> 1000\,M_\odot\,{\rm yr}^{-1}$ with a lens magnification factor of $\mu \sim 6-10$ (e.g., Bussmann et al. 2013; Yang et al. 2019; Maresca et al. 2022). An in-depth study of the CO(6–5) emission was performed by Yang et al. (2019) and found that G09v1.97 appeared to

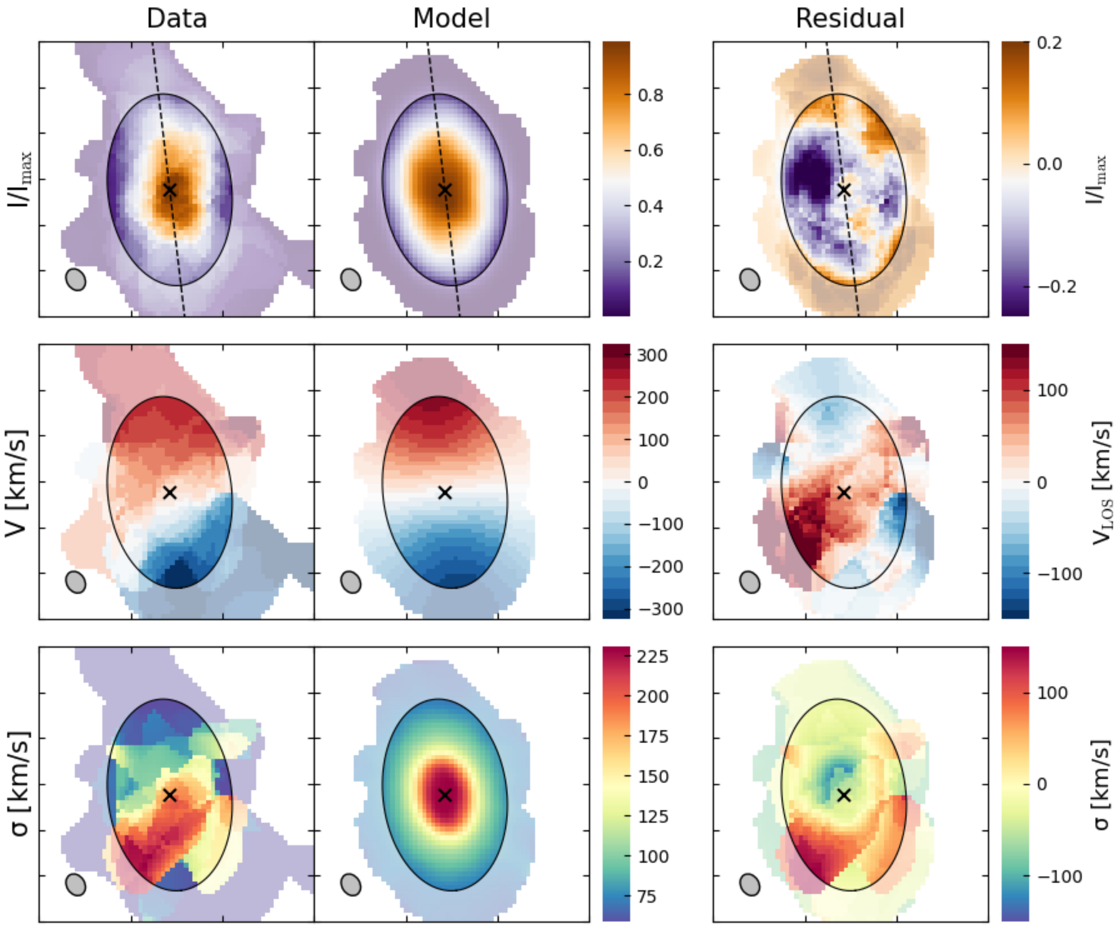

Figure 7.4: Fitting results from ^{3D}Barolo for G09v1.97 showing the moment-0 (top), moment-1 (middle), and moment-2 (bottom) data (first column), model (second column), and residual (third column). The final ring used for ^{3D}Barolo fitting is shown with the black ellipse and values outside this ring as made semi-transparent to emphasize this. Figure from Kade et al. (submitted).

be composed of two galaxies that were interacting and/or merging. Paper III used very high angular resolution ALMA observations of the CO(6–5) emission line to study the kinematics of G09v1.97 in the source plane.

7.6 Results of paper III

We used the sophisticated publicly available lens modeling tool PyAutoLens (Nightingale et al. 2021) to update the parametric lens model for G09v1.97. PyAutoLens has the additional capability of performing non-parametric modeling of the source emission, wherein no parametric model is assumed for the source. We used this capability to create a source-plane de-lensed CO(6–5) emission cube and found that the emission appeared to be from one, relatively compact, source with no evidence of an additional source as found in Yang et al. (2019). We also performed non-parametric modeling of the H_2O emission and dust continuum emission detected toward G09v1.97, although we note that the signal-to-noise of the H_2O emission was not sufficiently strong to make a source-plane de-lensed emission cube. Additionally, we used PyAutoLens to create source plane error maps and signal-to-noise ratio maps for all emission types.

We compared the spatial extents of the CO(6–5), H_2O, and dust continuum emission in the non-parametric source plane models. We found that the dust continuum emission was the most compact of the three emission types and that the extent of the CO(6–5) and H_2O emission were very similar.

We performed kinematic modeling of the CO(6–5) emission using the non-parametric modeling tool ^{3D}Barolo. ^{3D}Barolo fits a user-specified number of tilted rings. We found that the CO(6–5) was mostly well-modeled by a single rotating disk; however, we found tentative evidence of non-circular motions in the moment-0 and moment-1 residual maps shown in Figure 7.4. These residuals could be indicative of a bi-concial outflow, tidal tail from a galaxy interaction, or an additional galaxy. We used the results of our kinematic modeling to calculate $V_{\rm max}/\bar{\sigma}$ for G09v1.97 and found $V_{\rm max}/\bar{\sigma} = 2.8 \pm 0.4$. This value is within the expected region for semi-analytic models (e.g., Wisnioski et al. 2015) but lower than what has been found for disk galaxies at similar redshifts.

We used the kinematic modeling to calculate the dynamical mass of G09v1.97 and found $M_{\rm dyn} = (3.7 \pm 0.1) \times 10^{10}\,{\rm M}_{\odot}$ within 1 kpc (the extent of the CO(6–5) emission. We further calculated the total molecular gas mass assuming a conversion to CO(1–0) from Yang et al. (2017), finding $M_{\rm gas} = (2.0 \pm 0.8) \times 10^{9}\,{\rm M}_{\odot}$. This implied a depletion time of $t_{\rm dep} \sim 14 \pm 9\,{\rm Myr}$, significantly shorter than other galaxies at similar redshifts.

Combined with the residuals from the kinematic modeling, we suggested that G09v1.97 is either under-going or has recently undergone a merger or interaction, which presents as the non-circular motions detected in the moment-0 and moment-1 residuals. Should this be the case, it could explain the extremely high SFR found in G09v1.97.

My contribution paper III was as the primary leader of the project. C. Yang wrote the ALMA proposal and performed the data reduction and imaging process with help from the Nordic ALMA ARC Node. I performed the remainder of the data analysis, with the exception of the kinematic modeling from ^{3D}Barolo. I wrote the manuscript with the exception of some text provided for the following sections: Section 2.1 by S. König, Section 3.3.2 by J. Nightingale, and Sections 3.4 and 4.2 by M. Yttergren.

7.7 Introduction to paper IV

Paper IV focused on two strongly lensed SMG galaxies, SPT 0125−47 and SPT 2134−50, at $z \sim 2.5 - 2.8$. These sources were originally detected by the South-Pole Telescope (SPT) and reported in Weiß et al. (2013) with spectroscopic confirmations through CO(3–2) emission. Although some SPT sources have been studied in detail, these two sources remain relatively under-studied. One previous study from Spilker et al. (2016) used parametric lens models of SPT 0125−47 to suggest that the system seemed to be composed of three sources in the source plane. Paper IV

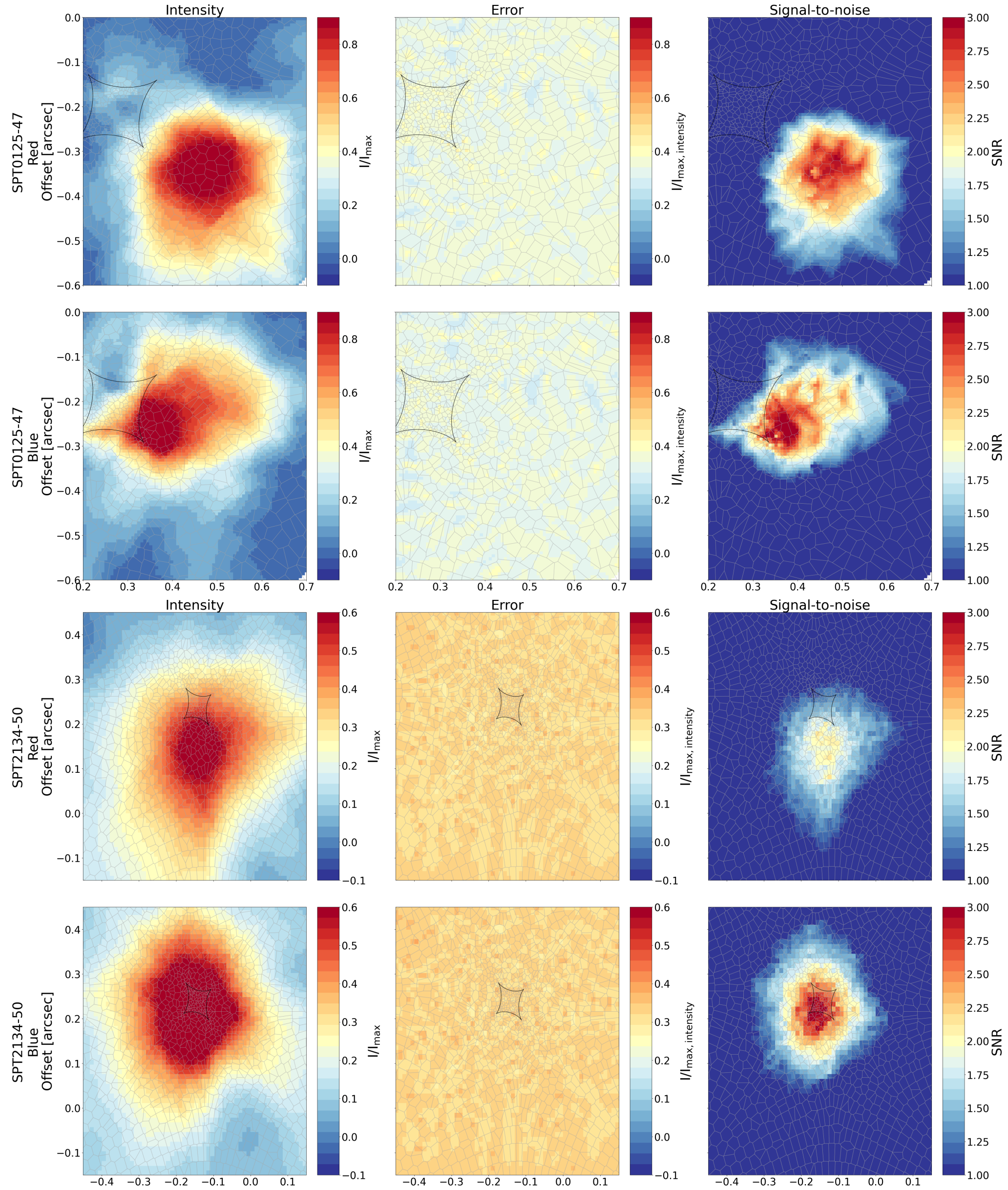

Figure 7.5: Source plane pixelized models for the red/blue spectral bins for SPT 0125−47 (top two rows) and SPT 2134−50 (bottom two rows). The left column shows the source plane intensity, the middle column shows the intensity error, and the right shows the signal to noise map for the bin (i.e., the intensity divided by the intensity error). Both the intensity and error maps are normalized, where the error map is normalized to the maximum of the intensity map, meaning that they can be interpreted as a per-pixel percentage error. The black lines show the caustic in each image and the background gray polygons show the Voronoi mesh.

used high-resolution ALMA observations of CO(3–2) emission to study the morphology of SPT 0125−47 and SPT 2134−50 in the source plane using non-parametric lens modeling.

7.8 Results of paper IV

Similar to Paper III, we used PyAutoLens to perform both parametric and non-parametric source plane modeling of the two galaxies. We found that in the parametric models, a single Sérisc source profile was sufficient to obtain a high-quality lens model without clear residual emission for both SPT 0125−47 and SPT 2134−50. Similar for the non-parametric source plane models, we found no evidence for source multiplicity for either SPT 0125−47 or SPT 2134−50. As with paper III, we created source plane error maps for the non-parametric models.

We performed a rudimentary investigation into the kinematics and morphology of the two galaxies. First, we investigated whether we should expect for our observations to be able to resolve star-forming clumps in our non-parametric source plane models. These clumps have been hypothesized as a cause for the very high SFRs often observed in SMGs and are suggested to exist on scales of $\sim 200 - 500\,\mathrm{pc}$ (e.g., Dekel et al. 2009; Bournaud et al. 2014). A number of previous studies have searched for clumps with mixed results (e.g., Hodge et al. 2016; Spilker et al. 2022). We found that our observations, while high-angular resolution, still only resolve down to scales of $\sim 800 - 1200\,\mathrm{pc}$ in the source plane and therefore would be unable to resolve these clumps should they exist.

We divided the CO(3–2) emission line into two bins corresponding to the red and blue portions of the spectra. We then parametrically and non-parametrically modeled this emission. From the parametric modeling we found clear evidence for differential lensing across the line spectrum for both galaxies, with significantly different magnification factors in each bin. The non-parametric source models suggested a velocity gradient in both sources, and did not provide any indications of clumpy structures, companions, or interactions. The nonparametric red/blue models, as well as signal-to-noise (SNR) maps of the source plane, are shown in Figure 7.5 for both SPT 0125−47 and SPT 2134−50. Given the very high SFRs of both sources, as well as their low depletion times (calculated using values from Aravena et al. (2016)), we suggested that an interaction and/or merger may have triggered the observed high SFR. In such a scenario, we would be observing these galaxies in a recently post-interaction/merger state wherein both galaxies are settling into disks. This is an attractive explanation because it is supported by studies that find that SMGs are mostly major mergers (e.g., Engel et al. 2010) and by theoretical predictions of galaxy evolution (e.g., Hopkins et al. 2008). Higher sensitivity data, with comparable or higher angular resolution, would be necessary to further investigate this.

In 2022 I co-supervised MSc student Markus Bredberg (2nd author) and he, with help from the Nordic ARC node, performed the imaging, continuum subtraction, and initial lens modeling (at the time using Visilens for both sources. My contribution to the project included performing the lens modeling using PyAutoLens and further analysis as well as the writing of the manuscript.

CHAPTER 8

SUMMARY & OUTLOOK

The way in which massive galaxies evolve at high-redshifts is still an open question with significant progress left to be made. Evidence from simulations of the early universe suggest that both feedback effects and the environment in which massive galaxies grow play a key role in their development. These processes are thought to govern their star-formation, morphology, and even regulate the growth of the central SMBH. Studies of high-redshift galaxies therefore must focus on both the external factors (e.g., environment) and internal processes (e.g., ISM, kinematics, etc.) at work in these sources. Only by studying these key factors can a clear determination be made about their capacity to influence the evolution of these galaxies.

Understanding the effect of environment on the evolution of massive galaxies in the early universe is an arduous task to undertake. Detecting even massive companion galaxies to massive galaxies is a challenge, with faint companions only beginning to be discovered in the past decade. Indeed, a number of studies have found evidence for tidal structures, bridges, or streams of gas between the detected smaller and fainter companions to their massive counterparts (e.g., Díaz-Santos et al. 2018; Guaita et al. 2022). Through studying the environment of different classes of high-redshift galaxies (e.g., quasars, SMGs), the observed differences in these classifications can begin to place them into an evolutionary context.

In the local universe, feedback effects can be observed with relative ease, at least compared to the high-redshift universe where distance compounds with technical limitations. Certain studies of high-redshift quasars have claimed detection of massive outflows through high-velocity [C II] spectral wings, only to be disproven with the acquirement of better data (e.g., Maiolino et al. 2012; Cicone et al. 2015; Meyer et al. 2022b). In contrast, other studies using more standard outflow tracers, such as OH, detected clear outflow signatures in $z > 4$ galaxies (e.g., Spilker et al. 2020; Butler et al. 2021). A wide range of mass-outflow rates have been suggested from these studies. A main concern with all studies of feedback in the high-redshift universe is the origin and nature of the outflow and the true effect of the outflow on the evolution of the galaxy (e.g., Spilker et al. 2020; Scholtz et al. 2020).

Many observational techniques and emission lines are lost at high-redshift and it is therefore observationally challenging to precisely determine both the presence of and the immediate impact of an AGN on the dust and gas of its host galaxy. One relatively common approach is to use CO observations to determine the heating mechanisms at work in a galaxy (e.g., Gallerani et al. 2014), however other studies argue that CO emission alone is insufficient to adequately differentiate between heating mechanisms (e.g., Mashian et al. 2015). It is therefore necessary to use a wider variety of emission lines to understand the ISM of high-redshift galaxies.

The gas kinematics of high-redshift galaxies relates directly to the environment and feedback effects occurring with the individual galaxy. Studies of the gas kinematics can reveal if the galaxy is a dynamically cold and settled disk or if the galaxy seems to be more dominated by turbulent motions. However, this is challenging due to the nature of high-redshift observations. In recent years, studies have found more settled disks (e.g., Rizzo et al. 2020; Rowland et al. 2024). However, it has also become clear that the angular resolutions challenges inherent to high-redshift observations, the kinematic fitting tool used for the study, and the gas tracer all pose challenges to accurate comparisons between different samples and studies.

The work of this thesis has focused on each of these different aspects; environment, feedback, gas heating mechanisms, and gas kinematics. Paper I focused on studying the environment of the two massive galaxies BRI 0952−0115 and AzTEC-3 in the early universe. These two galaxies represent prime candidates for ISM and environment studies. The results of Paper I, summarized in the previous chapter, demonstrated both the observational capability of ALMA and the distinct need for additional observations of this kind to determine the true impact of the environment.

Paper II focused on the ISM of the quasar BRI 0952 using multi-band ALMA observations. The results of paper II demonstrated that even with a wide variety of different atomic and molecular emission lines, it remains very challenging to make a precise determination of the gas heating mechanisms at work. This work highlighted that even with high-J CO transitions, it is not possible to robustly distinguish between star-formation driven heating versus AGN driven heating.

Paper III used CO(6–5) observations of the strongly lensed SMG G09v1.97 to study the gas kinematics of the galaxy in the source plane. This paper demonstrated the necessity of performing non-parametric source reconstructions rather than relying on parametric lensing models which cannot accurately describe the complex morphologies of galaxies. This work found that G09v1.97 seemed to be a smooth rotating disk with possible evidence for an outflow or tidal tail from a previous interaction. The results of this work highlighted the combined use of gravitational lensing and kinematic fitting tools to study ISM of high-redshift galaxies in detail.

Paper IV used high-resolution observations of two strongly lensed SMGs to investigate their source plane properties. The non-parametric source plane models for both galaxies shows smooth profiles in our rudimentary kinematics investigation, and both exhibited tentative indications of rotation. We suggested that both sources likely underwent some form of interactions and/or merger, likely the driving mechanism behind their elevated SFRs, and we observe them as settling into warm disks. The results of paper IV showed the necessity of very high angular resolution observations of bright emission lines in order to perform accurate and robust source plane reconstructions of high-redshift galaxies.

The work presented in this thesis has demonstrated the impressive observational capabilities of ALMA while also displaying the clear challenges of studying high-redshift galaxies. Systematic studies of high-redshift galaxies using very high angular resolution observations will continue to uncover the role and frequency of minor mergers. Emission line studies of different types of galaxies will provide additional insights into the gas heating mechanisms, specifically if the driving heating mechanism is the AGN or star formation. Finally, kinematic studies of strongly lensed high-redshift galaxies will continue to uncover the evolution of disk galaxies in the early universe.

Observations in the coming years will continue to provide clues to the processes governing the evolution of massive galaxies in the high-redshift universe. The means by which these galaxies sustain intense star-formation rates will become increasingly clear with additional deep high-resolution observations. The next generation of powerful telescopes (e.g., SKA, Large Synoptic Survey Telescope (LSST), Extremely Large Telescope (ELT), ngVLA, WSU ALMA, etc.) will play a decisive role in these discoveries, along with the already operational ALMA and *JWST* telescopes. The evolution of high-redshift massive galaxies shall not remain enshrouded in mystery for long.

BIBLIOGRAPHY

Aalto, S., Falstad, N., Muller, S., et al. 2020, A&A, 640, A104

Aalto, S., Garcia-Burillo, S., Muller, S., et al. 2012, A&A, 537, A44

Agertz, O., Kravtsov, A. V., Leitner, S. N., & Gnedin, N. Y. 2013, ApJ, 770, 25

Alatalo, K., Blitz, L., Young, L. M., et al. 2011, ApJ, 735, 88

Alberts, S. & Noble, A. 2022, Universe, 8, 554

Algera, H. S. B., Inami, H., De Looze, I., et al. 2024, MNRAS, 533, 3098

Amvrosiadis, A., Lange, S., Nightingale, J. W., et al. 2025, MNRAS, 537, 1163

Andreani, P., Retana-Montenegro, E., Zhang, Z.-Y., et al. 2018a, A&A, 615, A142

Andreani, P., Retana-Montenegro, E., Zhang, Z.-Y., et al. 2018b, A&A, 615, A142

Antonucci, R. 1993, ARA&A, 31, 473

Aravena, M., Spilker, J. S., Bethermin, M., et al. 2016, MNRAS, 457, 4406

Asensio Ramos, A. & Elitzur, M. 2018, A&A, 616, A131

Assef, R. J., Eisenhardt, P. R. M., Stern, D., et al. 2015, ApJ, 804, 27

Bañados, E., Venemans, B., Walter, F., et al. 2013, ApJ, 773, 178

Bakx, T. J. L. C., Tamura, Y., Hashimoto, T., et al. 2020, MNRAS, 493, 4294

Barnes, J. E. & Hernquist, L. 1998, ApJ, 495, 187

Beckmann, R. S., Devriendt, J., Slyz, A., et al. 2017, MNRAS, 472, 949

Beifiori, A., Courteau, S., Corsini, E. M., & Zhu, Y. 2012, MNRAS, 419, 2497

Bennert, V. N., Treu, T., Auger, M. W., et al. 2015, ApJ, 809, 20

Bergin, E. A., Kaufman, M. J., Melnick, G. J., Snell, R. L., & Howe, J. E. 2003, ApJ, 582, 830

Bianchi, S., De Vis, P., Viaene, S., et al. 2018, A&A, 620, A112

Bischetti, M., Feruglio, C., Piconcelli, E., et al. 2021, A&A, 645, A33

Bischetti, M., Maiolino, R., Carniani, S., et al. 2019, A&A, 630, A59

Blain, A. W., Smail, I., Ivison, R. J., Kneib, J. P., & Frayer, D. T. 2002, Phys. Rep., 369, 111

Bolatto, A. D., Wolfire, M., & Leroy, A. K. 2013, ARA&A, 51, 207

Bothwell, M. S., Smail, I., Chapman, S. C., et al. 2013, MNRAS, 429, 3047

Bouché, N., Carfantan, H., Schroetter, I., Michel-Dansac, L., & Contini, T. 2015, AJ, 150, 92

Bournaud, F., Perret, V., Renaud, F., et al. 2014, ApJ, 780, 57

Bower, R. G., Benson, A. J., Malbon, R., et al. 2006, MNRAS, 370, 645

Brinchmann, J., Charlot, S., White, S. D. M., et al. 2004, MNRAS, 351, 1151

Bron, E., Le Bourlot, J., & Le Petit, F. 2014, A&A, 569, A100

Bussmann, R. S., Pérez-Fournon, I., Amber, S., et al. 2013, ApJ, 779, 25

Butler, K. M., van der Werf, P. P., Rybak, M., et al. 2021, ApJ, 919, 5

Calzetti, D. 2001, PASP, 113, 1449

Cano-Díaz, M., Maiolino, R., Marconi, A., et al. 2012, A&A, 537, L8

Cao, X., Li, R., Nightingale, J. W., et al. 2022, Research in Astronomy and Astrophysics, 22, 025014

Capak, P. L., Riechers, D., Scoville, N. Z., et al. 2011, Nature, 470, 233

Carilli, C. L., Riechers, D., Walter, F., et al. 2013, ApJ, 763, 120

Carilli, C. L. & Walter, F. 2013, ARA&A, 51, 105

CASA Team, Bean, B., Bhatnagar, S., et al. 2022, PASP, 134, 114501

Casey, C. M., Chen, C.-C., Cowie, L. L., et al. 2013, MNRAS, 436, 1919

Casey, C. M., Narayanan, D., & Cooray, A. 2014, Phys. Rep., 541, 45

Casey, C. M., Zavala, J. A., Aravena, M., et al. 2019, ApJ, 887, 55

Cernicharo, J., Goicoechea, J. R., Daniel, F., et al. 2006, ApJ, 649, L33

Chapman, S. C., Blain, A. W., Smail, I., & Ivison, R. J. 2005, ApJ, 622, 772

Choi, E., Somerville, R. S., Ostriker, J. P., Naab, T., & Hirschmann, M. 2018, ApJ, 866, 91

Cicone, C., Maiolino, R., Gallerani, S., et al. 2015, A&A, 574, A14

Cicone, C., Maiolino, R., Sturm, E., et al. 2014, A&A, 562, A21

Cicone, C., Severgnini, P., Papadopoulos, P. P., et al. 2018, ApJ, 863, 143

Ciotti, L., Ostriker, J. P., & Proga, D. 2010, ApJ, 717, 708

Conselice, C. J. 2014, ARA&A, 52, 291

Coppin, K. E. K., Geach, J. E., Almaini, O., et al. 2015, MNRAS, 446, 1293

Cortijo-Ferrero, C., González Delgado, R. M., Pérez, E., et al. 2017, A&A, 606, A95

Crain, R. A., Schaye, J., Bower, R. G., et al. 2015, MNRAS, 450, 1937

Cresci, G. & Maiolino, R. 2018, Nature Astronomy, 2, 179

Croton, D. J., Springel, V., White, S. D. M., et al. 2006, MNRAS, 365, 11

Daddi, E., Dickinson, M., Morrison, G., et al. 2007, ApJ, 670, 156

Dasyra, K. M., Tacconi, L. J., Davies, R. I., et al. 2007, ApJ, 657, 102

De Looze, I., Cormier, D., Lebouteiller, V., et al. 2014, A&A, 568, A62

Decarli, R., Mignoli, M., Gilli, R., et al. 2019, A&A, 631, L10

Decarli, R., Walter, F., Neri, R., et al. 2012, ApJ, 752, 2

Decarli, R., Walter, F., Venemans, B. P., et al. 2017, Nature, 545, 457

Decarli, R., Walter, F., Venemans, B. P., et al. 2018, ApJ, 854, 97

Dekel, A., Birnboim, Y., Engel, G., et al. 2009, Nature, 457, 451

Di Matteo, T., Khandai, N., DeGraf, C., et al. 2012, ApJ, 745, L29

Di Matteo, T., Springel, V., & Hernquist, L. 2005, Nature, 433, 604

Di Teodoro, E. M. & Fraternali, F. 2015, MNRAS, 451, 3021

Di Teodoro, E. M., Fraternali, F., & Miller, S. H. 2016, A&A, 594, A77

Díaz-Santos, T., Armus, L., Charmandaris, V., et al. 2013, ApJ, 774, 68

Díaz-Santos, T., Assef, R. J., Blain, A. W., et al. 2018, Science, 362, 1034

Draine, B. T. 1978, ApJS, 36, 595

Draine, B. T. 2011, ApJ, 732, 100

Drew, P. M. & Casey, C. M. 2022, ApJ, 930, 142

Dubois, Y., Pichon, C., Welker, C., et al. 2014, MNRAS, 444, 1453

Duchêne, G. & Kraus, A. 2013, ARA&A, 51, 269

Dwek, E. & Arendt, R. G. 2020, ApJ, 901, 36

Ebeling, H., Stockmann, M., Richard, J., et al. 2018, ApJ, 852, L7

Eigenbrod, A., Courbin, F., & Meylan, G. 2007, A&A, 465, 51

Eisenhardt, P. R. M., Wu, J., Tsai, C.-W., et al. 2012, ApJ, 755, 173

Elbaz, D., Daddi, E., Le Borgne, D., et al. 2007, A&A, 468, 33

Emonts, B. H. C., Lehnert, M. D., Dannerbauer, H., et al. 2018, MNRAS, 477, L60

Engel, H., Tacconi, L. J., Davies, R. I., et al. 2010, ApJ, 724, 233

Fabian, A. C. 2012, ARA&A, 50, 455

Fakhouri, O., Ma, C.-P., & Boylan-Kolchin, M. 2010, MNRAS, 406, 2267

Fan, L., Han, Y., Nikutta, R., Drouart, G., & Knudsen, K. K. 2016, ApJ, 823, 107

Farrah, D., Lebouteiller, V., Spoon, H. W. W., et al. 2013, ApJ, 776, 38

Ferrarese, L. & Merritt, D. 2000, ApJ, 539, L9

Feruglio, C., Fiore, F., Carniani, S., et al. 2015, A&A, 583, A99

Feruglio, C., Maiolino, R., Piconcelli, E., et al. 2010, A&A, 518, L155

Fogasy, J., Knudsen, K. K., Drouart, G., Lagos, C. D. P., & Fan, L. 2020, MNRAS, 493, 3744

Fogasy, J., Knudsen, K. K., Lagos, C. D. P., Drouart, G., & Gonzalez-Perez, V. 2017, A&A, 597, A123

Förster Schreiber, N. M., Genzel, R., Lutz, D., & Sternberg, A. 2003a, ApJ, 599, 193

Förster Schreiber, N. M., Genzel, R., Lutz, D., & Sternberg, A. 2003b, ApJ, 599, 193

Fraternali, F., Karim, A., Magnelli, B., et al. 2021, A&A, 647, A194

Futamase, T. 2015, International Journal of Modern Physics D, 24, 1530011

Gaibler, V., Khochfar, S., & Krause, M. 2011, MNRAS, 411, 155

Gallagher, R., Maiolino, R., Belfiore, F., et al. 2019, MNRAS, 485, 3409

Gallerani, S., Ferrara, A., Neri, R., & Maiolino, R. 2014, MNRAS, 445, 2848

Gallerani, S., Neri, R., Maiolino, R., et al. 2012, A&A, 543, A114

Gallerani, S., Pallottini, A., Feruglio, C., et al. 2018, MNRAS, 473, 1909

Galliano, F. 2022, Habilitation Thesis, 1

Gao, Y. & Solomon, P. M. 2004, ApJ, 606, 271

Gebhardt, K., Bender, R., Bower, G., et al. 2000, ApJ, 539, L13

Gerin, M. & Phillips, T. G. 2000, ApJ, 537, 644

Giavalisco, M. 2002, ARA&A, 40, 579

Ginolfi, M., Jones, G. C., Béthermin, M., et al. 2020, A&A, 633, A90

González-Alfonso, E., Fischer, J., Bruderer, S., et al. 2013, A&A, 550, A25

González-Alfonso, E., Fischer, J., Isaak, K., et al. 2010, A&A, 518, L43

Gould, R. J. & Salpeter, E. E. 1963, ApJ, 138, 393

Graciá-Carpio, J., Sturm, E., Hailey-Dunsheath, S., et al. 2011, ApJ, 728, L7

Granato, G. L., De Zotti, G., Silva, L., Bressan, A., & Danese, L. 2004, ApJ, 600, 580

Guaita, L., Aravena, M., Gurung-Lopez, S., et al. 2022, A&A, 660, A137

Guilloteau, S., Omont, A., Cox, P., McMahon, R. G., & Petitjean, P. 1999, A&A, 349, 363

Gültekin, K., Richstone, D. O., Gebhardt, K., et al. 2009, ApJ, 698, 198

Häring, N. & Rix, H.-W. 2004, ApJ, 604, L89

Harrison, C. M. 2017, Nature Astronomy, 1, 0165

Harshan, A., Tripodi, R., Martis, N. S., et al. 2024, ApJ, 977, L36

Hashimoto, T., Inoue, A. K., Mawatari, K., et al. 2019, PASJ, 71, 71

Heckman, T. M. & Best, P. N. 2014, ARA&A, 52, 589

Hezaveh, Y. D., Marrone, D. P., Fassnacht, C. D., et al. 2013, ApJ, 767, 132

Hirashita, H. & Ferrara, A. 2002, MNRAS, 337, 921

Hirschmann, M., Dolag, K., Saro, A., et al. 2014, MNRAS, 442, 2304

Hodge, J. A. & da Cunha, E. 2020, Royal Society Open Science, 7, 200556

Hodge, J. A., Swinbank, A. M., Simpson, J. M., et al. 2016, ApJ, 833, 103

Högbom, J. A. 1974, A&AS, 15, 417

Hopkins, P. F., Hernquist, L., Cox, T. J., & Kereš, D. 2008, ApJS, 175, 356

Hopkins, P. F., Quataert, E., & Murray, N. 2012, MNRAS, 421, 3522

Hopkins, P. F., Somerville, R. S., Hernquist, L., et al. 2006, ApJ, 652, 864

Hopkins, P. F., Wetzel, A., Kereš, D., et al. 2018, MNRAS, 480, 800

Hubble, E. 1926, Contributions from the Mount Wilson Observatory / Carnegie Institution of Washington, 324, 1

Husband, K., Bremer, M. N., Stanway, E. R., & Lehnert, M. D. 2015, MNRAS, 452, 2388

Jarugula, S., Vieira, J. D., Weiss, A., et al. 2021, ApJ, 921, 97

Jones, G. C., Maiolino, R., Caselli, P., & Carniani, S. 2019, A&A, 632, L7

Jones, S. F., Blain, A. W., Stern, D., et al. 2014, MNRAS, 443, 146

Kade, K., Knudsen, K. K., Bewketu Belete, A., et al. 2024, A&A, 684, A56

Kade, K., Knudsen, K. K., Vlemmings, W., et al. 2023, A&A, 673, A116

Katz, N., Keres, D., Dave, R., & Weinberg, D. H. 2003, in Astrophysics and Space Science Library, Vol. 281, The IGM/Galaxy Connection. The Distribution of Baryons at z=0, ed. J. L. Rosenberg & M. E. Putman, 185

Kauffmann, G. & Haehnelt, M. 2000, MNRAS, 311, 576

Kaviraj, S., Devriendt, J., Dubois, Y., et al. 2015, MNRAS, 452, 2845

Kennefick, J. D., Djorgovski, S. G., & de Carvalho, R. R. 1995, AJ, 110, 2553

Kennicutt, R. C. & Evans, N. J. 2012, ARA&A, 50, 531

Kereš, D., Katz, N., Weinberg, D. H., & Davé, R. 2005, MNRAS, 363, 2

Kimura, H. 2016, MNRAS, 459, 2751

King, A. & Pounds, K. 2015, ARA&A, 53, 115

Kneib, J.-P., Bonnet, H., Golse, G., et al. 2011, LENSTOOL: A Gravitational Lensing Software for Modeling Mass Distribution of Galaxies and Clusters (strong and weak regime), Astrophysics Source Code Library, record ascl:1102.004

Knudsen, K. K., Watson, D., Frayer, D., et al. 2017, MNRAS, 466, 138

Kohandel, M., Pallottini, A., Ferrara, A., et al. 2024, A&A, 685, A72

Koprowski, M. P., Coppin, K. E. K., Geach, J. E., et al. 2020, MNRAS, 492, 4927

Kormendy, J. & Ho, L. C. 2013, ARA&A, 51, 511

Kreckel, K., Platen, E., Aragón-Calvo, M. A., et al. 2011, AJ, 141, 4

Krips, M., Martín, S., Sakamoto, K., et al. 2016, A&A, 592, L3

Lada, C. J. & Lada, E. A. 2003, ARA&A, 41, 57

Lagache, G., Cousin, M., & Chatzikos, M. 2018, A&A, 609, A130

Lamperti, I., Harrison, C. M., Mainieri, V., et al. 2021, A&A, 654, A90

Lang, P., Meidt, S. E., Rosolowsky, E., et al. 2020, ApJ, 897, 122

Laporte, N., Ellis, R. S., Boone, F., et al. 2017, ApJ, 837, L21

Lelli, F., Di Teodoro, E. M., Fraternali, F., et al. 2021, Science, 371, 713

Li, A. & Greenberg, J. M. 2002, ApJ, 577, 789

Li, J., Wang, R., Riechers, D., et al. 2020, ApJ, 889, 162

Licquia, T. C. & Newman, J. A. 2015, ApJ, 806, 96

Limousin, M., Richard, J., Jullo, E., et al. 2016, A&A, 588, A99

Lin, L., Patton, D. R., Koo, D. C., et al. 2008, ApJ, 681, 232

Litke, K. C., Marrone, D. P., Spilker, J. S., et al. 2019, ApJ, 870, 80

Liu, D., Förster Schreiber, N. M., Genzel, R., et al. 2023, ApJ, 942, 98

Liu, D., Schinnerer, E., Groves, B., et al. 2019, ApJ, 887, 235

Liu, L., Weiß, A., Perez-Beaupuits, J. P., et al. 2017, ApJ, 846, 5

Madau, P. & Dickinson, M. 2014, ARA&A, 52, 415

Magorrian, J., Tremaine, S., Richstone, D., et al. 1998, AJ, 115, 2285

Maiolino, R., Caselli, P., Nagao, T., et al. 2009, A&A, 500, L1

Maiolino, R., Gallerani, S., Neri, R., et al. 2012, MNRAS, 425, L66

Maiolino, R., Russell, H. R., Fabian, A. C., et al. 2017, Nature, 544, 202

Maresca, J., Dye, S., Amvrosiadis, A., et al. 2022, MNRAS, 512, 2426

Martín-Pintado, J., de Vicente, P., Fuente, A., & Planesas, P. 1997, ApJ, 482, L45

Mashian, N., Sturm, E., Sternberg, A., et al. 2015, ApJ, 802, 81

Mazzucchelli, C., Bañados, E., Decarli, R., et al. 2017, ApJ, 834, 83

Mazzucchelli, C., Decarli, R., Farina, E. P., et al. 2019, ApJ, 881, 163

Meyer, R. A., Decarli, R., Walter, F., et al. 2022a, ApJ, 927, 141

Meyer, R. A., Walter, F., Cicone, C., et al. 2022b, ApJ, 927, 152

Naab, T., Johansson, P. H., & Ostriker, J. P. 2009, ApJ, 699, L178

Neeleman, M. 2021, Qubefit v1.0.1

Neeleman, M., Bañados, E., Walter, F., et al. 2019, ApJ, 882, 10

Neeleman, M., Novak, M., Venemans, B. P., et al. 2021, ApJ, 911, 141

Neeleman, M., Prochaska, J. X., Kanekar, N., & Rafelski, M. 2020, Nature, 581, 269

Neeleman, M., Walter, F., Decarli, R., et al. 2023, ApJ, 958, 132

Nightingale, J., Hayes, R., Kelly, A., et al. 2021, The Journal of Open Source Software, 6, 2825

Nightingale, J. W., Dye, S., & Massey, R. J. 2018, MNRAS, 478, 4738

Noeske, K. G., Weiner, B. J., Faber, S. M., et al. 2007, ApJ, 660, L43

Oesch, P. A., Brammer, G., van Dokkum, P. G., et al. 2016, ApJ, 819, 129

Olsen, K., Greve, T. R., Narayanan, D., et al. 2017, ApJ, 846, 105

Omont, A., Petitjean, P., Guilloteau, S., et al. 1996, Nature, 382, 428

Oteo, I., Ivison, R. J., Dunne, L., et al. 2016, ApJ, 827, 34

Page, M. J., Symeonidis, M., Vieira, J. D., et al. 2012, Nature, 485, 213

Pallottini, A., Ferrara, A., Gallerani, S., et al. 2022, MNRAS, 513, 5621

Papovich, C., Dickinson, M., Giavalisco, M., Conselice, C. J., & Ferguson, H. C. 2005, ApJ, 631, 101

Patton, D. R., Wilson, K. D., Metrow, C. J., et al. 2020, MNRAS, 494, 4969

Pearson, W. J., Wang, L., Alpaslan, M., et al. 2019, A&A, 631, A51

Piconcelli, E., Vignali, C., Bianchi, S., et al. 2015, A&A, 574, L9

Pillepich, A., Nelson, D., Springel, V., et al. 2019, MNRAS, 490, 3196

Pillepich, A., Springel, V., Nelson, D., et al. 2018, MNRAS, 473, 4077

Planck Collaboration, Ade, P. A. R., Aghanim, N., et al. 2016, A&A, 594, A13

Pope, A., McKinney, J., Kamieneski, P., et al. 2023, ApJ, 951, L46

Popescu, C. C., Tuffs, R. J., Dopita, M. A., et al. 2011, A&A, 527, A109

Posses, A. C., Aravena, M., González-López, J., et al. 2023, A&A, 669, A46

Ramos Almeida, C. & Ricci, C. 2017, Nature Astronomy, 1, 679

Reddy, N. A., Steidel, C. C., Erb, D. K., Shapley, A. E., & Pettini, M. 2006, ApJ, 653, 1004

Reines, A. E. & Volonteri, M. 2015, ApJ, 813, 82

Riechers, D. A., Bradford, C. M., Clements, D. L., et al. 2013, Nature, 496, 329

Riechers, D. A., Capak, P. L., Carilli, C. L., et al. 2010, ApJ, 720, L131

Riechers, D. A., Carilli, C. L., Capak, P. L., et al. 2014, ApJ, 796, 84

Riechers, D. A., Cooray, A., Pérez-Fournon, I., & Neri, R. 2021a, ApJ, 913, 141

Riechers, D. A., Hodge, J., Walter, F., Carilli, C. L., & Bertoldi, F. 2011, ApJ, 739, L31

Riechers, D. A., Nayyeri, H., Burgarella, D., et al. 2021b, ApJ, 907, 62

Rizzo, F., Kohandel, M., Pallottini, A., et al. 2022, A&A, 667, A5

Rizzo, F., Vegetti, S., Fraternali, F., Stacey, H. R., & Powell, D. 2021, MNRAS, 507, 3952

Rizzo, F., Vegetti, S., Powell, D., et al. 2020, Nature, 584, 201

Roman-Oliveira, F., Fraternali, F., & Rizzo, F. 2023, MNRAS, 521, 1045

Rosenberg, M. J. F., van der Werf, P. P., Aalto, S., et al. 2015, ApJ, 801, 72

Rowland, L. E., Hodge, J., Bouwens, R., et al. 2024, MNRAS, 535, 2068

Sanders, D. B. & Mirabel, I. F. 1996, ARA&A, 34, 749

Sanders, D. B., Soifer, B. T., Elias, J. H., et al. 1988, ApJ, 325, 74

Scannapieco, C., White, S. D. M., Springel, V., & Tissera, P. B. 2011, MNRAS, 417, 154

Schawinski, K., Urry, C. M., Simmons, B. D., et al. 2014, MNRAS, 440, 889

Schaye, J., Crain, R. A., Bower, R. G., et al. 2015, MNRAS, 446, 521

Schmidt, M., Schneider, D. P., & Gunn, J. E. 1995, AJ, 110, 68

Schneider, P., Kochanek, C. S., & Wambsganss, J. 2006, Saas-Fee Advanced Course Series, Vol. 33, Gravitational Lensing: Strong, Weak and Micro (Berlin, Heidelberg: Springer-Verlag Berlin Heidelberg)

Scholtz, J., Alexander, D. M., Harrison, C. M., et al. 2018, MNRAS, 475, 1288

Scholtz, J., Harrison, C. M., Rosario, D. J., et al. 2020, MNRAS, 492, 3194

Scholtz, J., Harrison, C. M., Rosario, D. J., et al. 2021, MNRAS, 505, 5469

Schouws, S., Stefanon, M., Bouwens, R., et al. 2022, ApJ, 928, 31

Scoville, N., Lee, N., Vanden Bout, P., et al. 2017, ApJ, 837, 150

Sharda, P., da Cunha, E., Federrath, C., et al. 2019, MNRAS, 487, 4305

Sijacki, D., Vogelsberger, M., Genel, S., et al. 2015, MNRAS, 452, 575

Silk, J. & Rees, M. J. 1998, A&A, 331, L1

Simons, R. C., Kassin, S. A., Snyder, G. F., et al. 2019, ApJ, 874, 59

Simpson, J. M., Swinbank, A. M., Smail, I., et al. 2014, ApJ, 788, 125

Smit, R., Bouwens, R. J., Carniani, S., et al. 2018, Nature, 553, 178

Sparre, M. & Springel, V. 2016, MNRAS, 462, 2418

Spilker, J. S., Champagne, J. B., Fan, X., et al. 2025, ApJ, 982, 72

Spilker, J. S., Hayward, C. C., Marrone, D. P., et al. 2022, ApJ, 929, L3

Spilker, J. S., Marrone, D. P., Aravena, M., et al. 2016, ApJ, 826, 112

Spilker, J. S., Phadke, K. A., Aravena, M., et al. 2020, ApJ, 905, 85

Springel, V., White, S. D. M., Jenkins, A., et al. 2005, Nature, 435, 629

Stacey, G. J., Geis, N., Genzel, R., et al. 1991, ApJ, 373, 423

Stacey, G. J., Hailey-Dunsheath, S., Ferkinhoff, C., et al. 2010, ApJ, 724, 957

Stanley, F., Jolly, J. B., König, S., & Knudsen, K. K. 2019, A&A, 631, A78

Stark, D. P. 2016, ARA&A, 54, 761

Steidel, C. C., Giavalisco, M., Pettini, M., Dickinson, M., & Adelberger, K. L. 1996, ApJ, 462, L17

Stern, D., Lansbury, G. B., Assef, R. J., et al. 2014, ApJ, 794, 102

Strickland, D. K. & Heckman, T. M. 2009, ApJ, 697, 2030

Sturm, E., González-Alfonso, E., Veilleux, S., et al. 2011, ApJ, 733, L16

Tacconi, L. J., Genzel, R., Saintonge, A., et al. 2018, ApJ, 853, 179

Tacconi, L. J., Genzel, R., Smail, I., et al. 2008, ApJ, 680, 246

Tadhunter, C. 2008, New A Rev., 52, 227

Tamura, Y., Mawatari, K., Hashimoto, T., et al. 2019, ApJ, 874, 27

Thompson, A. R., Moran, J. M., & Swenson, George W., J. 2017, Interferometry and Synthesis in Radio Astronomy, 3rd Edition

Trakhtenbrot, B., Lira, P., Netzer, H., et al. 2017, ApJ, 836, 8

Treu, T. 2010, ARA&A, 48, 87

Tsai, C.-W., Eisenhardt, P. R. M., Wu, J., et al. 2015, ApJ, 805, 90

Übler, H., Genzel, R., Wisnioski, E., et al. 2019, ApJ, 880, 48

Umetsu, K. 2010, arXiv e-prints, arXiv:1002.3952

Urry, C. M. & Padovani, P. 1995, PASP, 107, 803

Vallini, L., Gallerani, S., Ferrara, A., Pallottini, A., & Yue, B. 2015, ApJ, 813, 36

Vallini, L., Tielens, A. G. G. M., Pallottini, A., et al. 2019, MNRAS, 490, 4502

Veilleux, S., Maiolino, R., Bolatto, A. D., & Aalto, S. 2020, A&A Rev., 28, 2

Venemans, B. P., Walter, F., Neeleman, M., et al. 2020, ApJ, 904, 130

Viero, M. P., Sun, G., Chung, D. T., Moncelsi, L., & Condon, S. S. 2022, MNRAS, 516, L30

Vogelsberger, M., Genel, S., Springel, V., et al. 2014, Nature, 509, 177

Walsh, D., Carswell, R. F., & Weymann, R. J. 1979, Nature, 279, 381

Walter, F., Weiß, A., Downes, D., Decarli, R., & Henkel, C. 2011, ApJ, 730, 18

Wardlow, J. L., Simpson, J. M., Smail, I., et al. 2018, MNRAS, 479, 3879

Wardlow, J. L., Smail, I., Coppin, K. E. K., et al. 2011, MNRAS, 415, 1479

Warren, S. J., Hewett, P. C., & Osmer, P. S. 1994, ApJ, 421, 412

Watson, D., Christensen, L., Knudsen, K. K., et al. 2015, Nature, 519, 327

Weiß, A., De Breuck, C., Marrone, D. P., et al. 2013, ApJ, 767, 88

Weiss, A., Downes, D., Walter, F., & Henkel, C. 2007, in Astronomical Society of the Pacific Conference Series, Vol. 375, From Z-Machines to ALMA: (Sub)Millimeter Spectroscopy of Galaxies, ed. A. J. Baker, J. Glenn, A. I. Harris, J. G. Mangum, & M. S. Yun, 25

Weiß, A., Henkel, C., Downes, D., & Walter, F. 2003, A&A, 409, L41

Willott, C. J., Percival, W. J., McLure, R. J., et al. 2005, ApJ, 626, 657

Wilson, T. L., Rohlfs, K., & Hüttemeister, S. 2013, Tools of Radio Astronomy

Wisnioski, E., Förster Schreiber, N. M., Fossati, M., et al. 2019, ApJ, 886, 124

Wisnioski, E., Förster Schreiber, N. M., Wuyts, S., et al. 2015, ApJ, 799, 209

Witstok, J., Jones, G. C., Maiolino, R., Smit, R., & Schneider, R. 2023, MNRAS, 523, 3119

Wu, J., Bussmann, R. S., Tsai, C.-W., et al. 2014, ApJ, 793, 8

Wu, J., Tsai, C.-W., Sayers, J., et al. 2012, ApJ, 756, 96

Yan, H. & Lazarian, A. 2012, J. Quant. Spectr. Rad. Transf., 113, 1409

Yang, C., Gao, Y., Omont, A., et al. 2013, ApJ, 771, L24

Yang, C., Gavazzi, R., Beelen, A., et al. 2019, A&A, 624, A138

Yang, C., Omont, A., Beelen, A., et al. 2017, A&A, 608, A144

Yang, C., Omont, A., Beelen, A., et al. 2016, A&A, 595, A80

Yue, M., Fan, X., Schindler, J.-T., McGreer, I. D., & Huang, Y.-H. 2019, ApJ, 883, 141

Zhang, H. & Yan, H. 2018, MNRAS, 475, 2415

Zhang, H., Yan, H., & Dong, L. 2015, ApJ, 804, 142

Zhang, L., Zhang, Z.-Y., Nightingale, J. W., et al. 2023, MNRAS, 524, 3671

Zhang, Z.-Y., Papadopoulos, P. P., Ivison, R. J., et al. 2016, Royal Society Open Science, 3, 160025